Femtosecond Laser Modification of Silicon Photonic Integrated Devices

by

Daniel Bachman

A thesis submitted in partial fulfillment of the requirements for the degree of

Doctor of Philosophy

in

Photonics and Plasmas

Department of Electrical and Computer Engineering
University of Alberta

Abstract

Silicon photonics is an emerging technology with many applications in communications and computing. Light is guided on chip through waveguides with a crystalline silicon core on top of a buffer oxide layer. Silicon is transparent at telecommunications wavelengths with a high index of refraction that enables miniaturization of photonic integrated circuits. However, this high index of refraction also makes resonant and interferometric based silicon photonic devices, like microring resonators and Mach-Zender interferometers, extremely sensitive to waveguide fabrication errors. Current fabrication techniques for silicon photonics are not accurate enough on a wafer scale to allow for proper phase control in these photonic elements and therefore, in most circumstances, post-fabrication tuning of these devices is required. In this thesis, a new, permanent tuning technique is proposed and demonstrated for phase trimming silicon photonic devices. It utilizes single femtosecond laser pulses to change the optical properties of the crystalline silicon waveguide core.

Microring resonators were fabricated and used as the test devices to investigate the femtosecond laser tuning mechanism. Using single pulses with a femtosecond laser wavelength of 400 nm, both positive and negative resonance shifts wavelength shifts were achieved. Positive resonance wavelength shifts were attributed to amorphization of a thin layer of the crystaline silicon at the waveguide surface and a linear relationship between resonance wavelength shift and the applied laser fluences was observed. Negative resonance wavelength shifts at higher fluences were attributed to laser ablation of a thin layer of material from the waveguide surface. The technique was also demonstrated to work through a thick SiO_2 cladding layer and beam shaping allowed for very fine tuning of microring resonance wavelengths. The same experiment was conducted at a femtosecond laser wavelength of 800 nm and it was found that the threshold fluence for permanent change to silicon at this wavelength

occured about 5x lower than previously reported values. Finally the technique was successfully demonstrated on advanced silicon photonic devices including resonance alignment in high-order microring filters and phase correction in polarization diversity circuit.

I dedicate this thesis to my wonderful wife Jocelyn.

Acknowledgements

I would like to thank everyone who has helped me along throughout the past 5 years in my PhD. You all made the journey a little easier and more fun to go through. All of the NanoFab staff who were helpful and trained me on the various tools and proccesses I would need to learn to fabricate my photonic devices. All the members of the Nanophotonics Research Lab (NPRL) including Cameron, Rice, Siamak, Ken, Marcello, and Alan. I appreciate all of the conversations we had in the lab. I also want to single out Ashok from the NPRL for his guidance and help at the very beginning of my PhD. He taught me how to fabricate the photonic devices I used throughout my PhD and how to measure them. I used many of his processes and equipment he initially set up. I would like to thank Jocelyn and Wayne for allowing me to use their experimental setup for a week and helping me operate it. For help wth the femtosecond laser and maintaining it in the latter stages of my PhD, I would like to thank Henry, Ward, and Eltahlway. I would also like to single out my collaborator Zhijiang for all the work he did with me. The initial experiments we did would not have been possible without his expertise and the optics guidance he gave me after he graduated was always very much appreciated. I really enjoyed working with him. I would like to thank Ying and Bob for allowing me to use their labs and for all their advice. I would like to thank my family and my wife for all the support and love they gave me throughout the years. My wife Jocelyn in particular was instrumental in the decision to pursue a PhD and I can not stress enough how important her support has been to me throughout the last few years. Finally I want to thank my supervisor Vien. He always had great ideas and was very supportive throughout my PhD. I will miss our discussions in the lab.

Contents

List of Figures

Chapter 1

Introduction

1.1 Photonics relevance to information processing

Modern electronic devices allow for the computation of vast amounts of information, but they are beginning to reach fundamental bottlenecks in processing speed and core-to-core data transfer [1]. In the past, electronics manufacturers relied on increasing transistor density and decreasing transistor dimensions to enable faster processing speeds, but as transistor dimensions reach sub-10 nm levels this approach will no longer be feasible [2]. This has forced manufacturers to achieve greater processing power by scaling up the number of cores on microprocessors and use techniques like parallel processing [3]. However, as the number of cores in a processor scales to the hundreds, conventional copper wire interconnects are not expected to be able to efficiently transfer the information required by each core throughout the chip [4–6]. It is estimated that copper interconnects use approximately 80% of the power on a microprocessor and signals must be amplified over long distances which decreases the signal propagation speed [7]. The International Technology Roadmap for Semiconductors (ITRS) lists optical interconnects as an emerging, alternative technology that may be able to replace these electronic interconnects and eliminate these barriers to greater processing speeds and more efficient data transfer [8].

Optical interconnects transfer information using light instead of electricity. By using light as the transfer medium, optical interconnects gain many advantages in speed, bandwidth, and propagation loss over traditional electronic interconnects [9, 10]. These advantages are currently being utilized for long range applications in the communications industry, as fiber optic cables have been replacing the older copper coaxial

cables. In an integrated platform, optical interconnects would come in the form of a photonic integrated circuit (PIC). PICs use planar dielectric waveguides patterned onto a chip to replace some of the functions of electronics such as filtering, multiplexing, and demultiplexing. Planar dielectric waveguides use total internal reflection to confine light and transfer it down the waveguide. This mechanism provides a low loss means to transport information across the chip at a speed much faster than electronics with a much wider bandwidth.

PICs also offer the ability to perform wavelength-division-multiplexing (WDM). WDM is a powerful information transfer technique used in optical communications to increase the density of information sent through a fiber optic cable or dielectric waveguide. The technique utilizes the property of light that in a linear material two separate wavelengths of light will not interact, which allows many different signals, encoded on separate wavelengths of light, to be sent down the same dielectric waveguide. In optical interconnects, the signals are then separated, or demultiplexed, at their destination by wavelength selective photonic components for detection and conversion back to electronic signals. WDM is a well-known and necessary approach in optical interconnects to increase the density of information carried by waveguides above that of conventional copper wires [10–12].

In an integrated platform WDM is usually accomplished using phase sensitive components like microring resonators and Mach Zender interferometers. They perform various functions in signal add/drop filters, modulators, and routing. For example, adding and removing specific wavelengths of light to a central bus waveguide can be accomplished by placing microring resonators along it. A microring resonator is an optical waveguide that is fabricated in a circle and placed close enough to the bus waveguide to allow evanescent coupling from the bus waveguide to the microring resonator. If the light that propagates around the circle constructively interferes with itself after each roundtrip, the microring is said to resonate and it will remove that specific wavelength from the bus waveguide. That wavelength can then be "dropped" out of the other side of the microring resonator into a different bus waveguide for detection.

1.2 Silicon as a photonics materials platform

Silicon has emerged as an attractive platform for achieving very large scale integration of PICs [13–16]. Silicon manufacturing is one of the most widely studied and perfected technologies due to its importance to the micro-electronics industry. Being the basis for complementary metal oxide semiconductor (CMOS) technology, there are many foundries already in place that could produce silicon PICs.

Silicon's optical properties are also well suited for PICs. Silicon is transparent at telecommunications wavelengths, and also has a high refractive index (3.45). This enables high confinement of the optical mode inside silicon waveguides which permits their dimensions to be made on the order of a few hundred nanometers. The high mode confinement allows for the miniaturization of silicon photonic components as well as for a much higher density PIC. Silicon also possesses other desirable properties for photonic devices like a relatively high optical damage threshold and thermal conductivity, while also possessing a free carrier dispersion effect that is suitable for optoelectronic applications [13].

1.3 Post-fabrication tuning requirements of silicon devices

Although silicon has been very well studied as a photonics platform and has many attractive optical properties, there are still many outstanding issues with the technology. Among them is a requirement for resonant and interference based silicon photonic components that are phase sensitive, like microring resonators and Mach-Zender interferometers, to undergo post-fabrication tuning in most circumstances [15]. Placing the resonances or interference minima of these devices at very specific wavelengths is critical in PICs especially in those designed for WDM applications so that the appropriate signal is added or removed from the main waveguide. Unfortunately, resonance and phase detuning is caused by some of silicon's most attractive features for optical interconnects, namely its high index of refraction and high optical mode confinement, which requires that the silicon waveguides to be made with extreme precision to avoid detuning in phase sensitive devices. For example, a 1 nm deviation

from the designed waveguide dimensions will cause a change in the effective index of refraction of a typical silicon waveguide of about 0.002, which results in over 100 GHz of detuning, or ∼1 nm, in the resonance of a microring resonator. This large deviation in the resonance wavelength is unacceptable for most applications.

Although silicon photonics manufacturing technology has advanced significantly, very small deviations in waveguide dimensions from the design values are currently unavoidable [4, 17, 18]. The tuning requirements of phase sensitive devices can be reduced by exploiting CMOS manufacturing processes, but process variations and the silicon layer thickness across an entire wafer vary by too much to avoid phase errors at this time.

1.4 State of the art tuning methods in silicon photonics

The most common approach to tuning phase sensitive photonic components is to modify the waveguide's index of refraction actively. This is usually accomplished by locally heating the waveguide. Local heating of silicon waveguides is achieved by placing resistive microheaters near a silicon waveguide, or in the waveguide, that are used to actively increase the temperature of the waveguide when supplied with current [19–22]. Since silicon has a relatively high, positive thermo-optic coefficient, an increase in waveguide temperature will cause an increase in the index of refraction of the silicon waveguide. For a typical silicon microring resonator this enables a red-shift in the resonance (increase in resonance wavelength) of the device. The technique has been shown to be a very effective and accurate way of tuning microring resonators.

Unfortunately, thermal tuning uses a very large amount of power to heat the silicon waveguides and requires extra fabrication steps along with the electronics to control the temperature [19–22]. This extra power consumption is one of the major challenges of current optical interconnect technology. In conjunction with the power needed for light production, modulation, and detection, optical interconnects currently consume more power than their electrical counterparts in short range applications despite having negligible propagation loss in comparison [4]. This limits current optical interconnect technology to relatively long range applications like rack

to rack and chip-to-chip communication ($\gtrsim$1cm) rather than shorter range applications like core-to-core communication ($\lesssim$1cm). Low power electrical tuning methods have also been demonstrated using free carrier dispersion or junction depletion effects in silicon modulators, however, their addition adds significant complexity to the fabrication process and they have a limited tuning range [23,24]. Therefore it is desirable to have a permanent tuning technique to either reduce the amount of power needed to correct the phase error of silicon photonic components or eliminate the need for active tuning altogether.

There have been many demonstrations of permanent tuning in silicon microring resonators. Microrings are used as the demonstration device because they commonly require tuning in practical applications and are very sensitive to any changes caused by the tuning technique. A common approach is to change the index of refraction of a sensitive cladding layer placed over top of the silicon waveguides in the microring resonator. These layers have been shown to be trimmed by UV [25] and visible light [26] as well as an electron beam [27]. The cladding layers have also been patterned over top of the silicon waveguides to modify the waveguide effective index of refraction after fabrication [28]. Another approach is to permanently modify the core silicon waveguide for tuning. There was demonstration of compaction in the SiO_2 insulator layer by an electron beam which induced stress in the silicon layer to change its index of refraction [29]. The silicon waveguide core can also be oxidized to reduce its size and its effective index of refraction. This has been performed using an atomic force microscope tip (AFM) [30] and a visible CW laser [31]. There are also many tuning methods that have been demonstrated in other materials systems that can be applied to silicon microrings [32–35].

Unfortunately the previously demonstrated permanent tuning methods are either too slow to be used in industrial applications and/or require a material or process that is not CMOS compatible. This thesis demonstrates a new permanent tuning method using a single femtosecond laser pulse to modify the surface of the core silicon waveguide that resolves both of these issues.

1.5 Reseach goals of the thesis

As outlined in the previous section, there has been no demonstration of a permanent phase tuning technique for silicon photonic integrated circuits that could be achieved quickly and in a CMOS environment for cost-effective mass production. **This thesis demonstrates a new technique based on irradiation of single femtosecond laser pulses to permanently modify silicon waveguides for phase tuning of silicon photonic integrated circuits.** A technique based on the application of a single laser pulse would only be limited in time by the repetition rate of the laser and the alignment system, which with proper engineering can be very fast. It also has the potential to be CMOS compatible as no special materials or processes are required during the fabrication of the photonic devices. The research goals of the thesis are outlined below:

- Explore the feasibility of using femtosecond laser pulses to modify silicon photonic waveguides and perform a proof of concept experiment.
- Evaluate the capability of single femtosecond laser pulses to tune silicon photonic microring resonators post-fabrication for devices both with and without a cladding.
- Use beamshaping to demonstrate the technique's ability to perform fine tuning of silicon photonic integrated circuits.
- Explore the ability of different wavelengths of femtosecond lasers to tune silicon photonic devices.
- Use the tuning technique to more accurately determine the minimum threshold fluence for femtosecond laser induced damage to a silicon surface at multiple wavelengths.
- Demonstrate application of the technique in tuning advanced silicon photonic integrated circuits.

Chapter 2 of this thesis gives some background information and models of basic silicon microring resonators and describes the basic fabrication procedure for the

silicon photonic integrated circuits used in this thesis. Chapter 3 is focused on background information related to femtosecond laser matter interactions with silicon and describes the femtosecond laser tuning apparatus used throughout this thesis. Chapter 4 is the initial results of the proof of concept experiment (published in ref. [36]). Chapter 5 describes the single shot femtosecond laser tuning experiments on both unclad and clad microring resonators (published in refs. [37,38]). Chapter 6 details how beam shaping allowed for fine tuning of microring resonators at multiple wavelengths and a new, accurate method for determining the threshold fluences for permanent change to a silicon waveguide. Chapter 7 provides demonstrations of the method for tuning of advanced silicon photonic integrated circuits. Chapter 8 describes the first demonstration of negative coupling in the silicon on insulator photonics platform. Finally Chapter 9 summarizes the thesis and offers suggestions for future research work.

Chapter 2

Silicon Microring Resonators

Microring resonators are an important building block for integrated optical circuits with applications in sensing [39–42], filtering [43–46] and modulation [23, 47]. The devices are made from waveguides bent to form a continuous loop, usually making a circle or a racetrack shape. As discussed in the introduction, these devices are very sensitive to fabrication imperfections in waveguide dimensions and for most applications require post-fabrication tuning. Their high sensitivity to index and dimension changes is the reason why they have been chosen in this thesis for the demonstration of our tuning technique based on single femtosecond laser pulses. This chapter outlines the basic theory of microring resonators that will be used to model changes in the device characteristics caused by femtosecond laser pulses.

2.1 All-pass and add-drop microring resonators

In a microring resonator, light is evanescently coupled to and from the microring via a bus waveguide placed close to the microring waveguide as shown in Figure 2.1. The light then travels around the microring and returns to its starting point with an acquired phase shift. If the field of the light constructively interferes with itself after every roundtrip, the resonant condition of the microring cavity will be satisfied. The wavelengths at which this condition is satisfied are represented by equation 2.1.

$$\lambda_m = \frac{2\pi R n_{eff}}{m} \tag{2.1}$$

where m is the integer resonance order, R is the radius of the microring, and n_{eff} is the waveguide effective index.

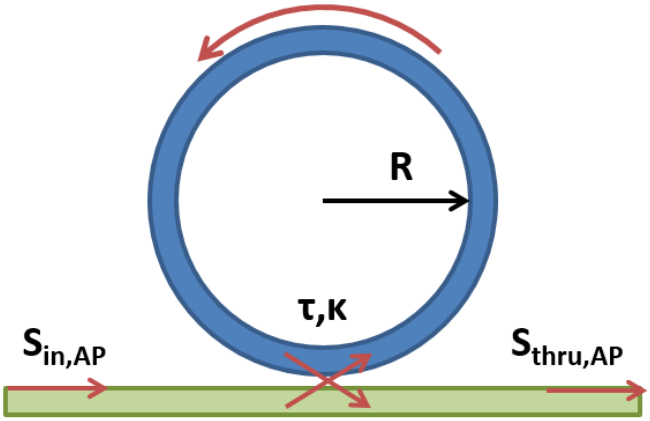

Figure 2.1: Schematic of an all-pass microring resonator with radius R. The blue and green sections are the microring and bus waveguides respectively. Red arrows represent the propagation of the electric field through the structure with S_{in} as in the input electric field and S_{thru} as the output electric field. κ and τ are the field coupling and transmission coefficients between the bus waveguide and microring.

The free spectral range (FSR) of a microring resonator is the spectral distance between the resonance wavelengths. In wavelength it can be detmined by

$$\Delta\lambda_{\mathrm{FSR}} = \frac{\lambda^2}{\mathrm{n}_g 2\pi \mathrm{R}} \tag{2.2}$$

where n_g is the group index of the microring waveguide and R is the radius of the microring. For the 15 μm microrings in Figure 2.2 and 2.4 the FSR is 5 nm.

Another useful measure of a resonator's performance is the quality factor (Q). It is defined by equation 2.3 below

$$\mathrm{Q} = \frac{\lambda}{\Delta\lambda_{\mathrm{3dB}}} \tag{2.3}$$

where λ is the resonance wavelength and $\Delta\lambda_{\mathrm{3dB}}$ is the full width half maximum of the resonance spectrum. If a spectrum has a higher quality factor, it indicates that it has a sharper resonance peak (or dip). Physically this is related to rate of energy lost from the cavity to the amount of energy stored in the cavity. The lower that the rate of loss from the cavity is will result in a higher quality factor.

There are two commonly used configuations for single microring resonator devices. In the all-pass configuration, the microring is evanescently coupled to a single bus waveguide as shown in Figure 2.1. The other common configuration is called add-drop

where a second bus waveguide is coupled to the microring at another location [46]. The frequency response of the all-pass microring can be modelled using a field coupling approach. In this approach, the magnitude and phase of the electric field for the light wave travelling through the microring is determined from which the transmission of the device can be obtained.

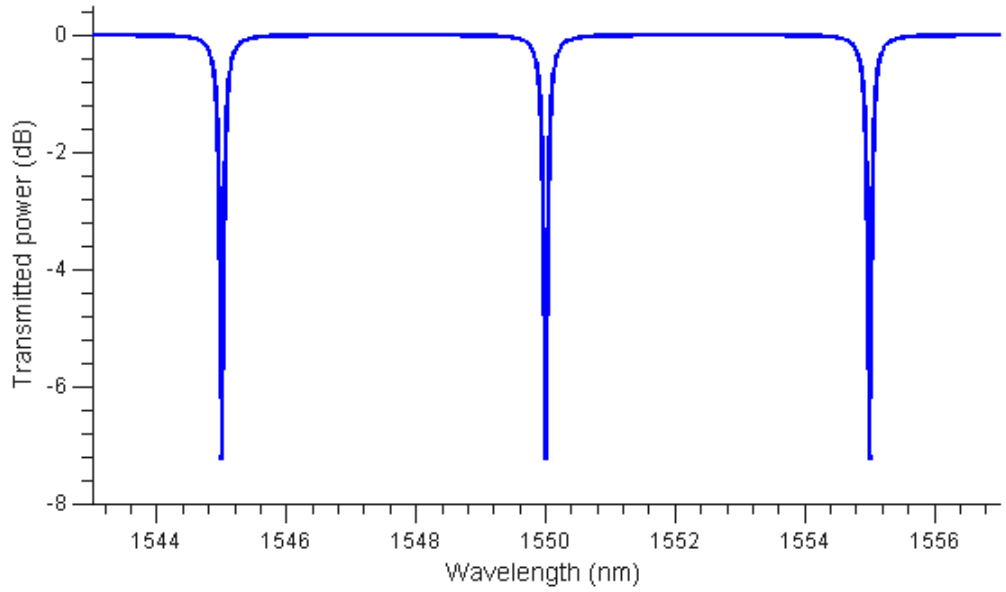

Figure 2.2: The through-port power spectrum of a typical all-pass silicon microring resonator with a radius of 15 μm that has values of $\tau = 0.95$ and $a_{\mathrm{rt}} = 0.98$.

We assume a monochromatic light wave is applied to the input of the all-pass microring, which travels from left to right in the bus waveguide and is represented by $\mathrm{S_{in,AP}}$ in Figure 1. The output light signal also travels from left to right and is represented by $\mathrm{S_{thru,AP}}$. As the light travels past the microring in the bus waveguide, a portion of it is coupled to the microring represented by the field coupling coefficient κ while the remaining portion travels past and is represented by the field transmission coefficient τ, where $|\kappa|^2 + |\tau|^2 = 1$ for power conservation and no coupling loss is assumed [48]. Equation 2.4 for the transmission at the through port can now be derived using the field coupling approach,

$$\frac{\mathrm{S_{thru,AP}}}{\mathrm{S_{in,AP}}} = \frac{\tau - a_{\mathrm{rt}} e^{-j\phi_{\mathrm{rt}}}}{1 - a_{\mathrm{rt}}\tau e^{-j\phi_{\mathrm{rt}}}} \tag{2.4}$$

where $a_{\mathrm{rt}} = e^{-\alpha\pi \mathrm{R}}$ is the roundtrip field attenuation factor and $\phi_{\mathrm{rt}} = \mathrm{n_{eff}}(2\pi/\lambda)2\pi\mathrm{R}$

is the roundtrip phase acquired by the light wave. In this expression, α representing the power attenuation in the waveguide, n_{eff} the effective index of the waveguide, R the radius of the microring, and λ the free space wavelength of the light.

At the output of the device, the transmitted light power is given by $|S_{thru,AP}|^2$. The through-port power spectrum is plotted in Figure 2.2 for a typical silicon microring with a radius of 15 μm.

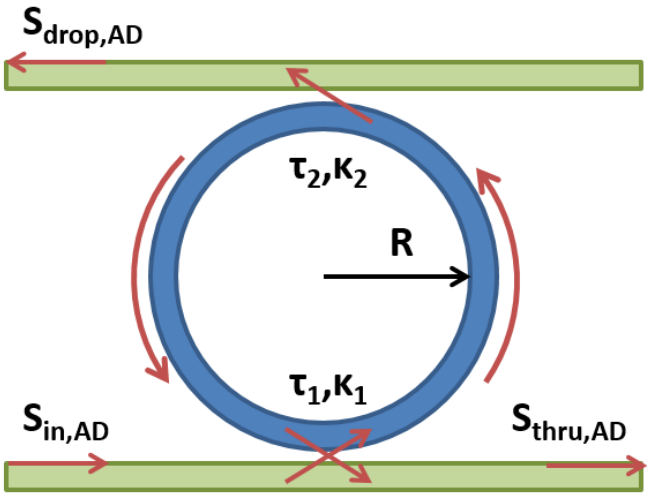

Figure 2.3: Schematic of an add-drop microring resonator with radius R. The blue and green sections are the microring and bus waveguides respectively. Red arrows represent the propagation of the electric field through the structure with S_{in} as in the input electric field and S_{thru} and S_{drop} as the output electric fields. $\kappa_{1,2}$ and $\tau_{1,2}$ are the field coupling and transmission coefficients between the bus waveguides and microring.

The add-drop microring resonator configuration is similar to the all-pass configuration. A schematic of an add-drop microring resonator is in Figure 2.3. The only difference between an add-drop microring resonator and an all-pass microring resonator is the addition of a second bus waveguide coupled to the microring resonator. This second bus wavegide has field coupling and transmission coefficients κ_2 and τ_2 respectively. The microring now has two outputs, one in the main bus waveguide labelled $S_{thru,AD}$, and one at the secondary bus waveguide labelled $S_{drop,AD}$. The through-port transmission is very similar to that of the all-pass microring resonator with $S_{thru,AD}$ given by equation 2.5 while the ouput at the drop port is given by equation 2.6.

$$\frac{\mathrm{S}_{\mathrm{thru,AD}}}{\mathrm{S}_{\mathrm{in,AD}}} = \frac{\tau_1 - \tau_2 a_{\mathrm{rt}} e^{-j\phi_{\mathrm{rt}}}}{1 - a_{\mathrm{rt}}\tau_1\tau_2 e^{-j\phi_{\mathrm{rt}}}} \tag{2.5}$$

$$\frac{\mathrm{S}_{\mathrm{drop,AD}}}{\mathrm{S}_{\mathrm{in,AD}}} = \frac{-\kappa_1\kappa_2 a_{\mathrm{rt}}^{1/2} e^{-j\phi_{\mathrm{rt}}/2}}{1 - a_{\mathrm{rt}}\tau_1\tau_2 e^{-j\phi_{\mathrm{rt}}}} \tag{2.6}$$

At the outputs of the add-drop microring device, the transmitted light powers are given by $|\mathrm{S}_{\mathrm{thru,AD}}|^2$ and $|\mathrm{S}_{\mathrm{drop,AD}}|^2$. The power spectrum for both outputs is plotted in Figure 2.4 for a typical silicon microring with a radius of 15 μm.

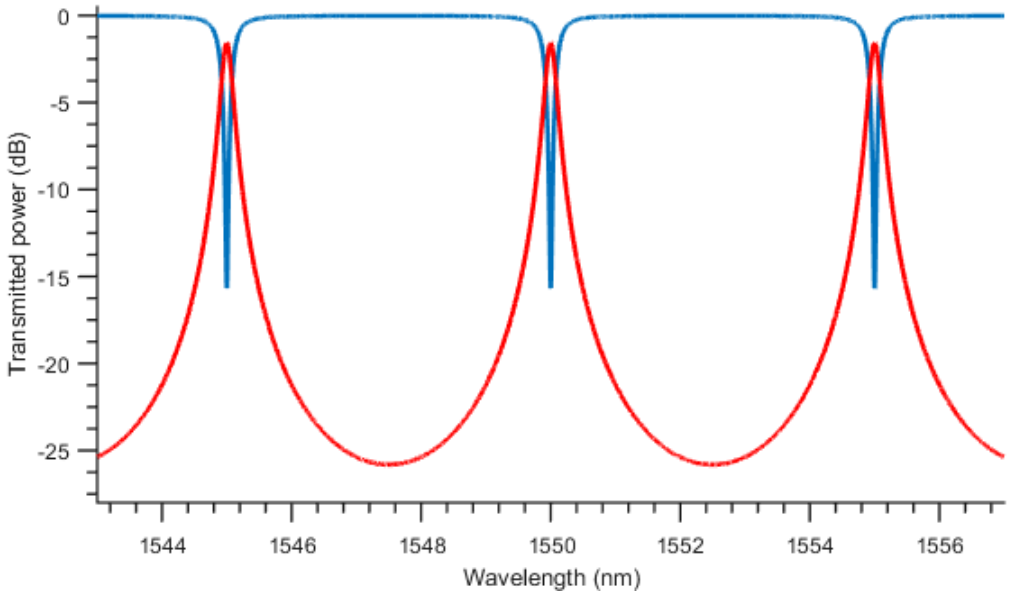

Figure 2.4: The through-port, blue line, and drop-port, red line, power spectrum of a typical add-drop silicon microring resonator with a radius of 15 μm that has values of $\tau_1 = \tau_2 = 0.95$ and $a_{\mathrm{rt}} = 0.98$.

The minimas in the through-port frequency response of an all-pass and add-drop microring and the maximas in the add-drop microing drop-port frequency response occur when the microring's resonant condition is satisfied. It is important for microring resonators that act as filters and modulators that their resonances occur at specifically designed wavelengths. As discussed in the introduction, this is not possible to achieve in silicon photonics using current state-of-the-art fabrication techniques and for this reason a post fabrication tuning method is required.

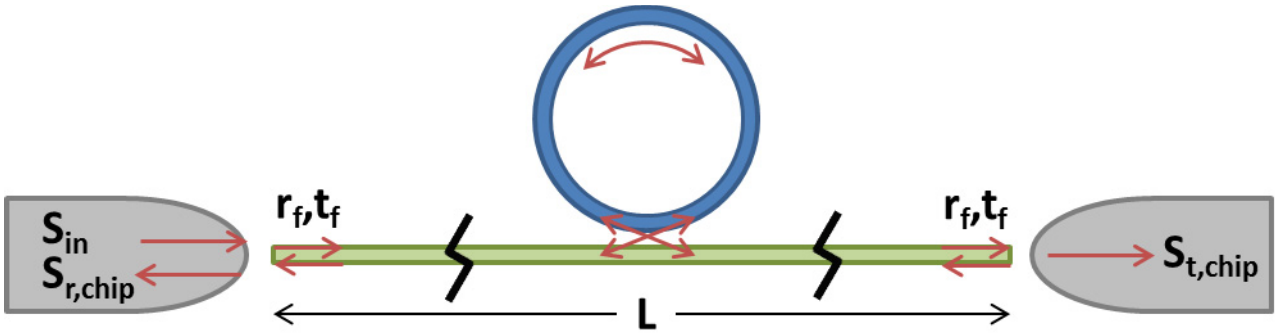

Figure 2.5: Schematic of coupling to the chip for the purpose of measuring a microring. The grey fiber optic cables couple light on/off the chip by butt coupling to the green bus waveguides, which then couple light to the blue microring waveguides. The reflections at the end facet are represented by the field reflection coefficient r_f and the field transmission coefficient t_f. Red arrows follow the propagation of the light's electric field through the chip of length L. S_{in}, $S_{r,chip}$, and $S_{t,chip}$ represent the input, reflected and transmitted propagating electric fields from the chip.

2.2 Modelling the chip level response

Figure 2.2 shows the response of an ideal all-pass microring resonator operating in isolation. In practice, the silicon microrings fabricated in our lab are measured on long input/output waveguides and butt coupling from lensed optical fibers is used to get light on and off the chip for measurement as shown in Figure 2.5. The coupling points on the chip are created by cleaving the chip which exposes the cleaved end waveguide facets. Butt coupling to the waveguide end facets causes reflections due to the index mismatch between the fiber, the air, and the waveguide. The reflections turn the long input/output waveguide into a Fabry-Perot cavity which modifies the measured frequency response from the chip. In order to extract the microring resonator's properties accurately from measured data, this modification to the frequency response of the system must also be modelled.

The modelling of the system is carried out in a very similar manner to the modelling of an individual microring. The field coupling approach is used to track the electric field of the light in the system at every junction and equation 2.7 is derived analytically. For the case where the test device is an all-pass microring resonator we obtain

$$\frac{S_{thru,chip}}{S_{in}} = \frac{(1 - r_f^2)S_{thru,AP}e^{-j\phi_l}}{1 - r_f^2 S_{thru,AP}^2 e^{-2j\phi_l}} \tag{2.7}$$

where r_f is the field reflection coefficient at the end facet, $S_{thru,AP}$ is the microring transmission coefficient represented by equation 2.4, and ϕ_l is the phase change over one length of the chip. r_f can be determined experimentally by fitting the waveguide response far from a microring resonance to that of a Fabry-Pérot resonator response. If r_f is zero then equation 2.7 reduces to equation 2.4 multiplied by a phase factor due to the input/output waveguide.

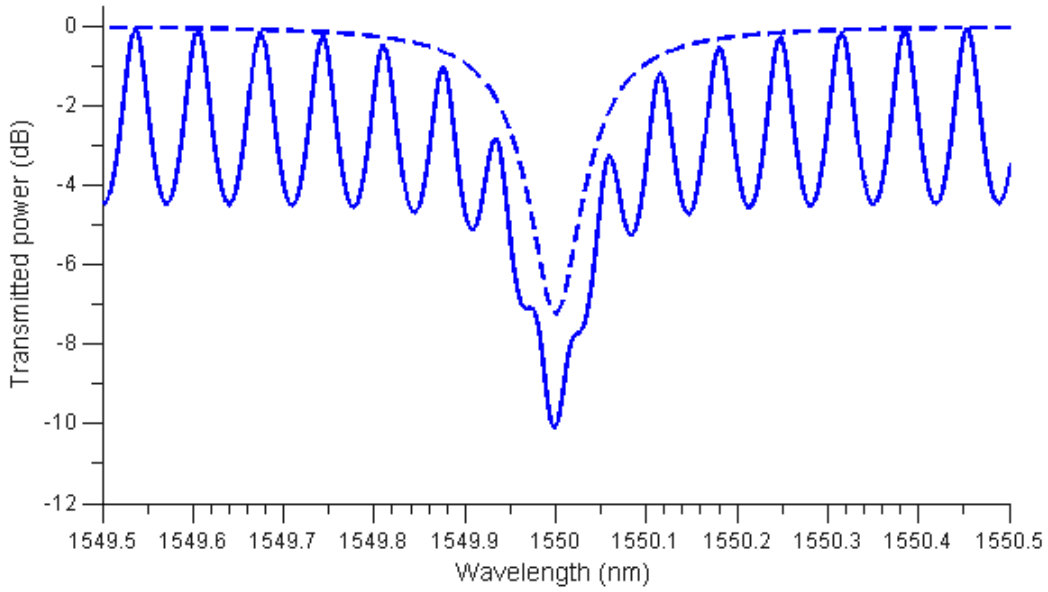

Figure 2.6: The modified transmission spectrum, solid line, of an all-pass microring resonance spectrum, dashed line, due to reflections at the waveguide end facets. The modelled all-pass silicon microring resonator has a radius of 15 μm with $\tau = 0.95$ and $a_{rt} = 0.98$. The model assumes a chip length of 3mm.

Figure 2.6 shows how the resonance spectrum of a microring resonator is modified by the reflections from the chip end facets. Typical experimental parameters for silicon microrings, end facet reflection coefficients, and chip length were used to produce the model. Equation 2.7 has a very similar form to the response of a Fabry-Pérot resonator with the only difference being the addition of the microring response, $S_{Thru,AP}$, next to the phase terms. At wavelengths far from the microring resonance wavelength, the response looks very similar to the response of a Fabry-Pérot resonator. However near the microring resonance, the chip's response does not resemble one of a microring

resonator or a Fabry-Pérot resonator. The difference between the microring response and the total response from the chip is very large and it illustrates the need to model the Fabry-Pérot effect in equation 2.7 for the purpose of extracting the microring parameters, a_{rt} and τ.

Normally a_{rt} and τ are indistinguishable quantities from the measurement of an individual all-pass microring's frequency response i.e. the resonance power spectrum for two microrings with a_{rt} and τ interchanged are identical. In order to determine these microring parameters separately, a different measurement technique that enables measurement of the phase response of the microring must be used. The Fabry-Pérot resonator-like response of the chip that is created by the end facets provides some phase information indirectly in the frequency response near a microring resonance. Since the phase response of the microring is different with a_{rt} and τ interchanged, this modifies the frequency response of the entire chip described by equation 2.7 which allows for the separate extraction of a_{rt} and τ.

2.3 Fabrication of silicon photonic integrated circuits

Commercial 4 inch silicon-on-insulator (SOI) wafers with a 340 nm crystalline Si (c-Si) layer on top of a 1 μm-thick SiO_2 buffer and 500 μm structural silicon layer were used as the starting point for the photonic device fabrication. A complete process flow of the device fabrication is shown in Figure 2.7. All device fabrication was carried out in the University of Alberta Nanofab.

The SOI substrates were first diced into 1x1 cm^2 pieces using a Disco DAD 321 dicing saw. The individual chips were then cleaned in a piranha solution (3:1 mixture of H_2SO_4 (96%) and H_2O_2 (30%)), rinsed with de-ionized (DI) water, and dried with an N_2 gun.

Patterning the chips would then be carried out using electron beam lithography. Positive electron beam lithography resist ZEP 520A was first diluted with anisole and then spun onto the chips and baked using a Brewer Spinner and Hotplate. Two drops of the diluted ZEP 520A were placed in the center of the chip before starting the spin cycle immediately after. The chip was spun using a spread cycle at 500 RPM for 5 s

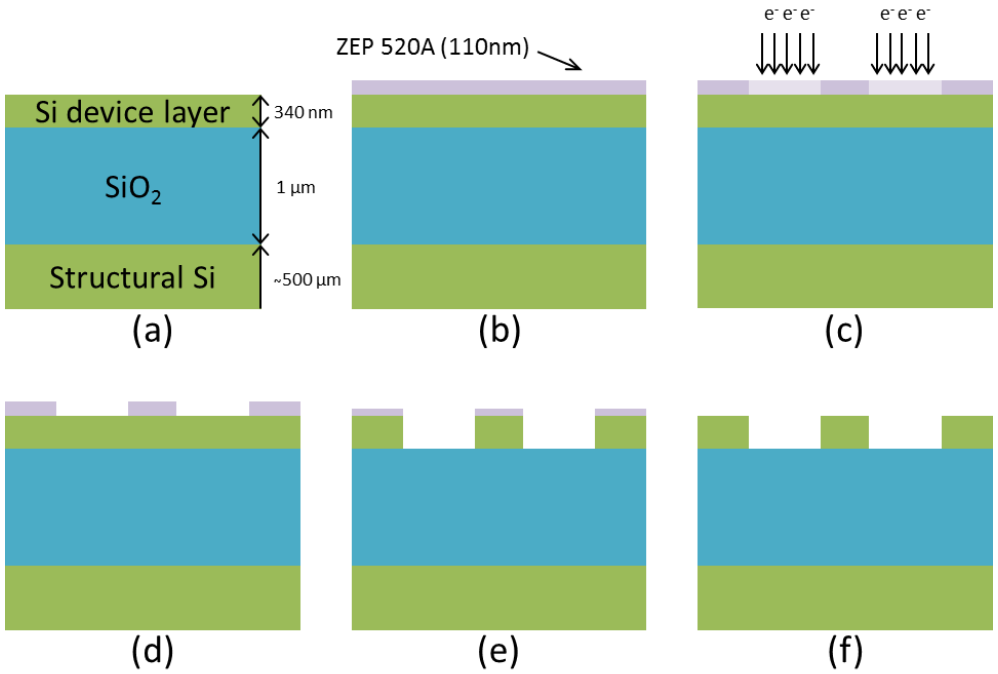

Figure 2.7: Cross-sectional schematic of the silicon chip at all photonic waveguide fabrication steps. A detailed description of all steps is in the body of the report. (a) The chip was first diced and cleaned to start the fabrication. (b) Electron beam resists spinning. (c) Electron beam lithography. (d) Development. (e) Dry etch. (f) The finished chip after cleaning.

and then ramped to 5000 RPM for 40 s. After spinning, the chip was transferred to the hotplate for baking at 170°C for 10 minutes to evaporate any remaining solvent. This left a layer of electron beam resist about 110 nm thick measured using a Filmetrics system and a test bare Si chip.

A Raith 150-TWO system was used to perform the electron beam lithography. The system was operated at an accelerating voltage of 10 kV and using the 10 µm aperture to provide a beam current of about 27 pA . Focusing on the chip was accomplished on 20 nm gold particles that were placed near a corner of the chip in a solution. The long input/ouput waveguides for the devices were patterned using the fixed-beam-moving-stage (FBMS) option at a dose of 35 µC/cm^2 and width of 4 µm. The microring devices were patterned using the area write option at a dose of 35 µC/cm^2 and a step size of 8 nm. It took about 15 minutes for the system to write one microring and input/output waveguide pattern. After the exposure, the chip was developed in ZED N50 for 40 s and immediately transferred to an MIBK/IPA 3:1 mixture for 30 s

before being rinsed in isopropyl alcohol (IPA) for 30 s and DI water after that for a few seconds. The chip was then rinsed with DI water from a gun and dried with the N_2 gun.

After inspection from an optical microscope, dry etching was used to transfer the pattern to the substrate with smooth and vertical sidewalls. Before etching, the chip had to be mounted onto a 4 inch carrier wafer to be loaded into the STS Inductively Coupled Plasma Reactive Ion Etch (ICP-RIE) machine. This was accomplished by spinning a thin layer of HPR-504 photoresist onto the wafer and then using a drop of photoresist in the center like a glue for the chip. The wafer was then baked at a 115°C for 5 minutes to evaporate the solvent. The chip was etched using the PRECNPRL recipe for about 45 s which uses a combination of SF_6 and C_4F_8 to provide vertical sidewalls while etching the silicon waveguides. After the etch, the chip was released from the carrier wafer in a sonicated acetone bath for 10 minutes before being rinsed with IPA and DI water and then dried with an N_2 gun.

2.4 Summary

The beginning of this chapter provides the basic modelling of silicon microring resonators that will be used throughout this thesis. It is concluded by a description of the fabrication procedure used to make the silicon microring resonators used in this thesis.

Chapter 3

Femtosecond laser tuning experiment

The purpose of this chapter is to provide some background information on femtosecond laser-matter interaction with silicon and how this can modify the properties of a crystalline silicon substrate. It is concluded by a description of the experimental apparatus used in the femtosecond laser modification experiments.

3.1 Femtosecond Laser Surface Modification

The ability of high power lasers to melt or ablate the surface of materials has been well known since just after the invention of the laser in the 1960s [49]. At that time, researchers were using lasers that had a minimum pulse duration on the order of nanoseconds. Laser technology has since improved to allow for high power pulse durations on the femtosecond time scale. The shorter pulses lead to different laser-matter interactions with much smaller interaction volumes which is suitable for modifying materials on the nanoscale [50].

3.2 Femtosecond laser-matter interaction with silicon

Lasers that have a photon energy greater than the bandgap of a semiconductor will mostly interact with the electronic system of the semiconductor. The laser photons are absorbed in semiconductors by the electrons through processes like interband transitions or free carrier absorption. A single electron may be involved in the ab-

sorption of multiple photons which can place it very high in the conduction band. For the electron to return to an equilibrium state in the semiconductor's valence band, it must lose the extra energy it has acquired. For an indirect bandgap semiconductor like silicon this is accomplished by electron interactions with the lattice and the energy is lost to heating the lattice (creating phonons). The process of transferring the energy from the electron to the lattice takes place on the order of picoseconds [51].

For nanosecond or longer laser pulse durations, most electrons will have had time to relax to an equilibrium state in the material and the laser-matter interactions can be considered to take place in an equilibrium state. However, the same assumptions are not true for femtosecond pulse durations because the electrons have not had time to relax to their equilibrium state while the pulse is still interacting with the material. This makes the description and modelling of the processes much more complicated under these conditions, but it does lead to interesting properties. Unlike nanosecond pulses, the processes for melting can become non-thermal with femtosecond pulses [52, 53]. As the laser pulse interacts with the material, it creates a very high density plasma that affects the stability of the silicon lattice [54]. The destability is caused by the removal of so many electrons from their bonding states in the valence band of the semiconductor to anti-bonding states in the conduction band of the semiconductor [55]. This destability in the lattice can lead to so-called cold melting of the lattice on time scales much shorter than it would take for thermal processes and melting is observed in under a picosecond [52,53,56]. For femtosecond laser pulses, the pathway to melting can either be thermal or non-thermal depending on the laser fluence [53,57].

After causing melting of the silicon structure, if the femtosecond laser pulse has enough energy then laser ablation may take place. Ablation is the process by which a laser can remove material from the surface it is interacting with. For femtosecond pulses, the material removal occurs long after ($\sim$1 ns) the laser pulse has finished interacting with the material through a hydrodynamic mechanism [58,59]. The irradiated silicon experiences a rapid expansion upon melting which causes a rarefaction wave to travel through the melted silicon and eject the material from the surface [58, 59]. This can lead to very small volumes of material being ejected from the surface [59].

3.3 Silicon structure after femtosecond laser irradiation

The final state of the silicon after femtosecond laser irradiation is the most important factor for using it in micromachining applications like post-fabrication tuning of integrated optical circuits. However, there have been far fewer studies of the final state of the silicon left over after melting or ablation than on the transient processes during the laser matter interaction [60, 61].

If a single femtosecond laser pulse has enough energy to cause the crystalline silicon to melt, but not enough to ablate the silicon then the material properties of the silicon will be modified by the resolidification process. The literature reports conflicting results about the final phase of the laser affected region, whether it is amorphous silicon or crystalline silicon with defects and small polycrystalline grains.

Bonse et al. studied the surface of initially crystalline silicon after irradiation with single 800 nm, Gaussian shaped femtosecond laser pulses [62]. An amorphous silicon layer was found using micro-Raman spectroscopy for pulses with enough energy to melt the surface but not cause laser ablation. A micro-Raman study of silicon spots irradiated by 1030 nm femtosecond pulses by Kiani et al. also showed the existence of an amorphous silicon layer [63]. An amorphous silicon layer was also found by Izawa et al. in cross sectional transmission electron microscopy (TEM) studies of silicon irradiated with 267nm, 400 nm, and 1550 nm femtosecond laser pulses [64, 65]. However, their TEM results for 800 nm pulses did not show the formation of amorphous silicon until after six laser shots which disagrees with the result from Bonse et al. [66]. For less than five shots with 800 nm pulses, the study identified a preamorphization phenomenon wherein a change of the surface reflectivity of the silicon surface was found but there was no observable amorphous layer under TEM analysis. Regardless of the final state of matter in these studies, they all show that the silicon in the femtosecond laser affected region has undergone a change that could be used in micromachining applications.

The literature also disagrees on the thickness of the laser affected regions in silicon for single 800 nm femtosecond laser pulses below the ablation threshold, while only one study was found for other wavelengths. TEM analysis by Izawa et al. found

that for 267, 400, 800, and 1550 nm Gaussian shaped pulses, the laser affected layer thicknesses were independent of the laser fluence below the ablation threshold [64,65]. The thicknesses of amorphous silicon were: 7 nm for 267 nm pulses, 17 nm for 400 nm pulses, 42 nm for 800 nm pulses (6 shots), and 56 nm for 1550 nm pulses. However, scanning laser microscopy performed by Bonse et al. and the TEM study by Hoche et al. on single 800 nm femtosecond laser pulses concluded that the thickness of the amorphous silicon was dependent on the laser fluence with a maximum thickness in both cases of about 60 nm [61, 67].

For laser fluences above the ablation threshold, the amount of silicon removed by a single femtosecond laser pulse is dependent on the laser fluence [65, 68]. As the laser fluence increases, so does the amount of material removed ranging from several nanometers to microns. The phase of the material underneath the laser ablated zone is dependent on the number of shots as well as the fluence of the laser for 800 nm wavelength femtosecond laser pulses. Single shot studies of femtosecond laser ablation at near threshold fluences as well as very high fluences found defective crystalline silicon underneath the ablation zone [62, 69]. However multiple shot studies at laser fluences near the ablation threshold have found the existence of amorphous silicon near the ablation threshold [70–73].

3.4 Silicon melting threshold fluence estimation

The threshold fluence for melting silicon can be estimated from silicon's heat capacity and heat of fusion. The only unknown using this method of determining the fluence is the absorption depth of the femtosecond laser pulse since nonlinear processes are likely to play a large role. To avoid this problem, the depth of the amorphous silicon layers that were produced by femtosecond laser pulses and measured by Izawa et al. in [65] in a cross sectional TEM study will be used. The threshold fluence will be estimated for both 400 nm and 800 nm pulses since they are both used in this thesis.

There will be two processes that will determine how much energy is required to melt silicon. The first is the temperature increase from room temperature to the melting temperature of silicon (1687 K). After this the silicon must transition from a solid to liquid phase. Both of these processes are described in the equation below.

$$Q = mC\Delta T + mH_f \tag{3.1}$$

where Q is the required energy for melting, m is the mass of the silicon area melted, C is the specific heat capacity of silicon (0.7 J/gK), δT is the temperature change to the melting temperature, and H_f is the heat of fusion for silicon (1.79 kJ/g). The mass of silicon can be calculated per unit area by multiplying the density (2.329 g/cm^3) by the depth of the molten silicon layer. This then gives the energy required per unit area which is equivalent to the fluence. For 400 nm pulses, Izawa et al. found the a-Si layer to be 17 nm while for 800 nm pulses it was 42 nm.

Inputing all the values into equation 3.1 yields a threshold fluence of 0.014 J/cm^2 for 400 nm pulses and 0.035 J/cm^2 for 800 nm pulses. Now it is important to note that these values are the abosorbed fluences by the silicon and not the incident fluences. It is also noted that there will be some energy absorbed beneath this layer. To account for absorption of the pulse below the molten layer, I will assume that the depth of the amorphous silicon layer is the skin depth of the pulse meaning that $1 - e^{-1}$ of the pulse energy is absorbed in the molten layer. To account for the reflection at the air-silicon interface, the reflectance for both wavelengths is calculated from the Fresnel formulas with the index of refraction for silicon being 5.58 and 3.68 at 400 nm and 800 nm respectively [74]. This gives a reflectance of 48% for 400 nm and 33% for 800 nm.

Taking all these factors in account yields an estimated melting threshold fluence of 0.043 J/cm^2 for 400 nm and 0.083 J/cm^2 for 800 nm.

3.5 Apparatus

In order to provide accurate and reproducible results when tuning silicon microring resonators with a femtosecond laser, it was decided to use single femtosecond laser pulses instead of multiple pulse irradiation. The single femtosecond laser pulses at a wavelength of 400 nm were produced by frequency doubling ~130 fs FWHM, 800 nm pulses in a BBO (barium borate) nonlinear crystal that were produced by a Ti:sapphire laser. The single pulses are created by triggering the Pockels cells of the femtosecond laser once to release a single pulse. After the crystal, a 2 mm BG39

bandpass filter was then placed in the beam path to remove the remaining 800 nm light. The 400 nm pulses were used initially instead of 800 nm pulses because of silicon's higher absorption at 400 nm [75]. For the 800 nm experiment, the nonlinear crystal and filter were removed from the beam path and pulses were taken directly from the laser to the tuning apparatus.

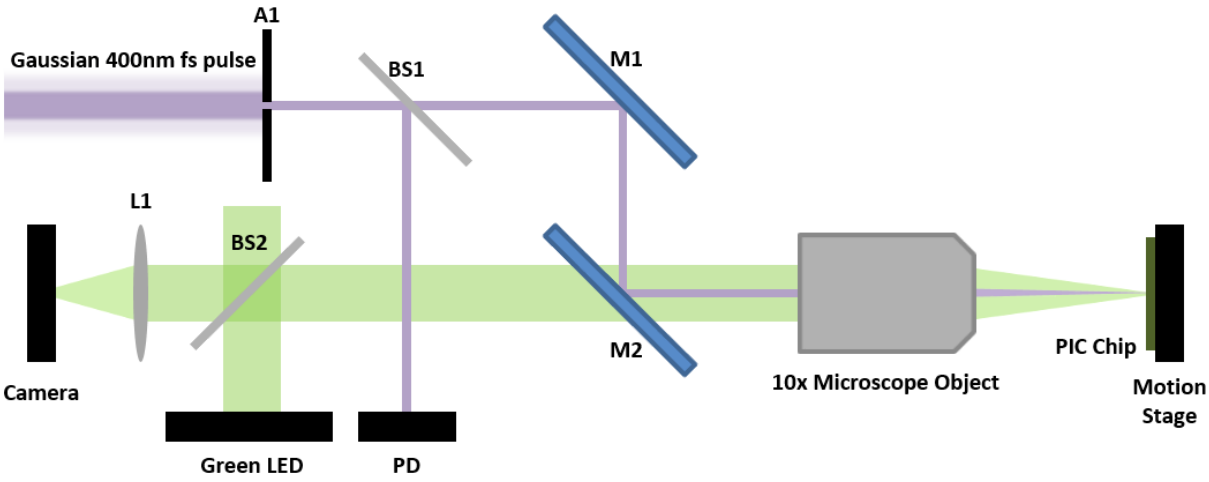

Figure 3.1: Setup for the femtosecond laser tuning aparatus. The center of a Gaussian pulse of 8 mm beam waist diameter is passed through a pin hole (A1), and was imaged onto the device. M1 and M2 are dielectric mirrors, L1 is a plano-convex lenses, BS1 and BS2 are glass slides acting as beam splitters.

The apparatus used for tuning silicon microring resonators is shown in Figure 3.1. The aperture (A1) is used to create either a "top-hat" beam profile or Gaussian-like beam profiles. The "top-hat" beam profile is obtained by demagnified imaging of the center part of the Gaussian beam selected with a hard pinhole aperture, where the intensity distribution is close to uniform. The technique provides a flat fluence profile over the entire beam spot. The pinhole aperture can also be used to create an Airy disc pattern when focused which can then be approxmated as a Gaussian beam profile. This allows for different sizes of a Gaussian beam profile to be created depending on the size of the aperture chosen. The radius of the Airy disk, r_1, is related to the size of the aperture as shown by equation 3.2 [76].

$$r_1 = 1.22\frac{f\lambda}{D} \tag{3.2}$$

where f is the focal length of the lens, λ is the wavelength of light, and D is the

aperture diameter. The formula assumes that the lens is placed directly after the aperture.

After the aperture, there is a glass slide used as a beam splitter to sample the energy of the laser pulse at a photodiode for fluence calculations. It is calibrated by placing a power meter at the chip location and correlating the voltage of the photodiode to pulse energies at the power meter.

The beam is then directed through the microscope objective and to the chip by two dielectric mirrors. M1 is a dielectric mirror for either 400 nm or 800 nm light depending on the wavelength of the experiment whereas M2 is a 400 nm dielectric mirror for the 400 nm experiments and a 90/10 splitter for the 800 nm experiment.

A green LED is used to image the chip for alignment purposes. The 532 nm green LED passes through M2 because it is either a dielectric mirror at 400 nm or a beam spitter designed for 800 nm and both are transparent to the imaging LED at this wavelength. The image is collected by a long focal length lens L1 (60 cm) and focused onto a CCD camera.

Not shown in Figure 3.1 are two irises between aperture A1 and mirror M1 used to ensure the beam was coming through the setup straight for every experiment. The objective could also be removed and replaced with two irises on a tube to ensure the beam passed through the center of the objective. To get the beam from the main beam line to the setup, a flip mirror on the main beam line was used to direct the beam to a periscope made of two metal mirrors to get the beam to the height of the table being used.

Relating to mass post-fabrication trimming of silicon photonic integrated circuits, the apparatus as shown here can be made entirely automated for faster and more reliable operation.

3.6 Summary

This chapter details how a femtosecond laser can be used to change the properties of an initially crystalline silicon substrate. It also shows the apparatus that was used in this thesis to modify silicon photonic integrated circuits. The next chapter demonstrates the proof of concept for the tuning technique in this thesis.

Chapter 4

Femtosecond laser tuning of silicon microring resonators: Proof of concept

4.1 Hypothesis

It has already been discussed that high power femtosecond lasers are able to deliver a large amount of energy to a surface in a very short amount of time. This energy deposition can permanently change the surface of the chosen material. In the case of crystalline silicon substrates, it was observed under a microscope that there was a permanent colour change at the surface of the material in the laser affected region. The question pertaining to silicon photonics is: can this colour change be used as a mechanism to change the index of refraction in crystalline silicon waveguides in a controllable manner? In particular, can this mechanism be used to correct for fabrication induced phase errors in silicon photonic devices such as microring resonators and interferometers? These initial questions are what lead to the research conducted in this thesis and the proof of concept experiment is discussed in this chapter.

To test this hypothesis, a single microring resonator was subjected to irradiation by single femtosecond laser pulses and the shift of the microring resonances and changes to quality factor were recorded. The results of the experiment are described below.

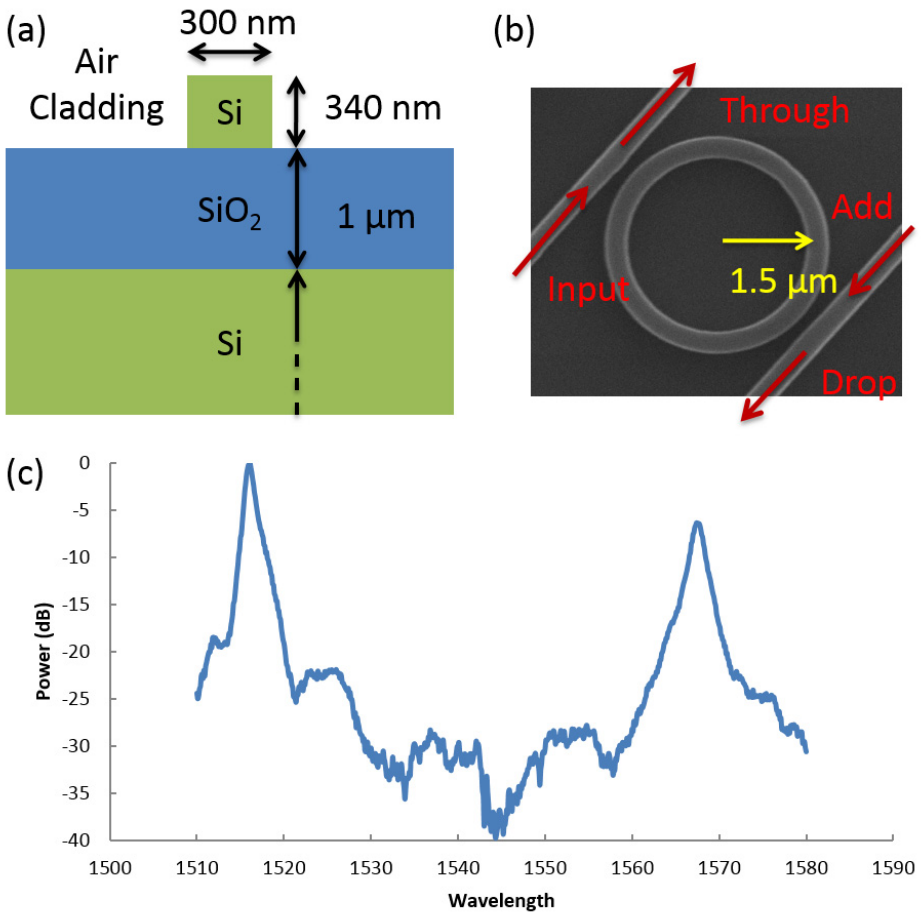

Figure 4.1: (a) Cross sectional diagram of the waveguides. (b) A top-down SEM image of the ultracompact microring resonator. (c) Initial drop port response of the microring resonator.

4.2 Initial Microring Characterization

For the proof of concept experiment, a single add/drop silicon microring resonator was used as the test device. The ultra-compact silicon microring resonator had a radius of 1.5 µm and was made from air clad c-Si waveguides 340 nm tall and 300 nm wide operated in the TM mode. A cross sectional schematic of the waveguides and an SEM picture of the microring resonator are in Figure 4.1 (a) and (b). The device had a free spectral range of 51.4 nm and the initial drop port spectrum is shown in Figure 4.1 (c).

4.3 Laser Beam Characteristics

For the proof of concept experiment, 400 nm femtosecond pulses were generated using the aparatus described in Chapter 3, Figure 3.1. The pulses were then imaged onto the chip after passing through a pinhole aperture to create a top-hat beam profile with a radius of about 10 μm. This made the beam spot much larger than the microring diameter, while the use of the top-hat profile ensured that the entire device would be affected by a constant laser fluence.

4.4 First laser shot

The ultra-compact microring resonator was first characterized and then shot by a single femtosecond laser pulse at a fluence of 0.08 J/cm^2. This fluence was chosen for the first shot because tests on bare silicon showed a change in the surface colour for any laser shot above 0.06 J/cm^2 and targeting this fluence ensured we would affect some change to the silicon surface (0.07 J/cm^2 was the target fluence, but due to about a 10% uncertainty in the energy of the laser pulse it came out a little higher). The laser pulse covered the entire microring device and a colour change was noted at the silicon surface around the microring device. Due to the small size of the waveguides, no change could be observed at the top of the silicon waveguides under observation with an optical microscope. A plot of the microring resonance originally at 1516.1 nm is shown in Figure 4.2 before and after the laser shot.

The single laser pulse caused the microring resonance wavelength to red shift (increase) by 4.4 nm. This result shows that it is possible to change the resonance wavelength of a microring resonator with a single femtosecond laser pulse. It is also possible from this result to find the change in the waveguide effective index of refraction from the change in the microring resonance wavelength by taking the derivative of equation 2.1 with respect to the effective index.

$$\Delta \mathrm{n_{eff}} = \frac{\Delta\lambda}{\lambda_\mathrm{o}} \mathrm{n}_g \tag{4.1}$$

where n_g is the group index and λ_o is the initial resonance wavelength.

The original index of refraction for a silicon waveguide is obtained from mode

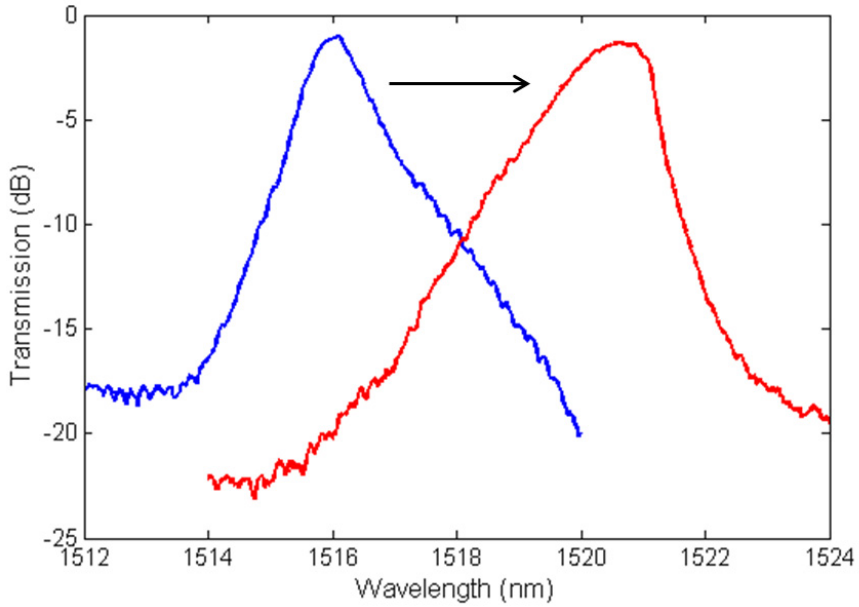

Figure 4.2: Drop port response of the short wavelength resonance before (blue) and after (red) the first laser shot at a fluence of 0.08 J/cm^2. The resonance wavelength has increased by 4.4 nm.

solver simulations and found to be about 2.3 for air clad waveguides with core dimensions 340x300 nm^2. This gives a change in the effective index of refraction for the silicon waveguide of about 0.014 for the short (1516 nm) and long (1567 nm) wavelength resonances measured.

The quality factor of the microring resonances have also changed, decreasing by about 30% from 1330 to 905 for the short wavelength resonance. These low quality factors give the microring a very broadband response as is seen in 4.2. This is due to the high loss in the microring from the very tight bending radius. We will study extra loss induced by femtosecond laser irradiation in subsequent experiments.

4.5 Multiple laser shots

After the first shot on the microring was shown to be able to shift the microring's resonance wavelength, additional tests at varying laser fluences were conducted to see if the femtosecond laser pulses could shift the microring's resonance again. The results of the measured wavelength shifts at two resonances are shown in Figure 4.3.

After the initial laser shot at a fluence of 0.08 J/cm^2, nine more shots at a tar-

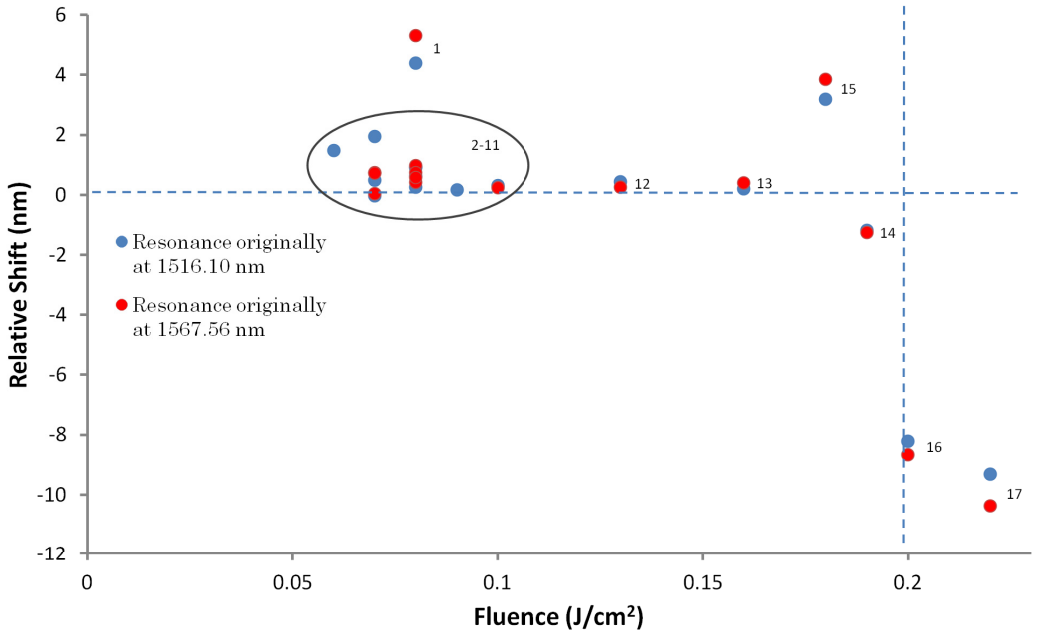

Figure 4.3: The relative shift in the microring's resonance with each successive shot. 17 shots were conducted and they are labelled 1-17 on the plot. Dashed lines are included at a relative shift of zero and a fluence of 0.20 J/cm^2.

get fluence of 0.07 J/cm^2 were conducted. These shots red shifted the microring's resonance by about another 5 nm in total. The laser fluence of the shots were then gradually increased to a fluence of 0.22 J/cm^2, however due to the 10% uncertainty in the laser fluence from shot-to-shot the fluence did not always increase monotonically. Small positive resonance wavelength shifts were recorded until the 14$^{\text{th}}$ laser shot at a fluence of 0.19 J/cm^2 where a negative shift was recorded. The 15$^{\text{th}}$ laser shot was attempted at the same fluence, but came out at 0.18 J/cm^2 where a large positive resonance wavelength shift was observed. For the next two laser shots at fluences of 0.20 and 0.22 J/cm^2, large negative resonance wavelength shifts were observed.

The quality factor of the microring also changed after each laser shot. Figure 4.4 shows the quality factor recorded for the microring resonances originally at 1516 nm and 1567 nm. After the first shot on the microrings which saw a decrease in the microring's quality factor of about 30%, the microring's quality factor remained relatively constant for the rest of the experiment changing only slightly as the laser fluence was increased.

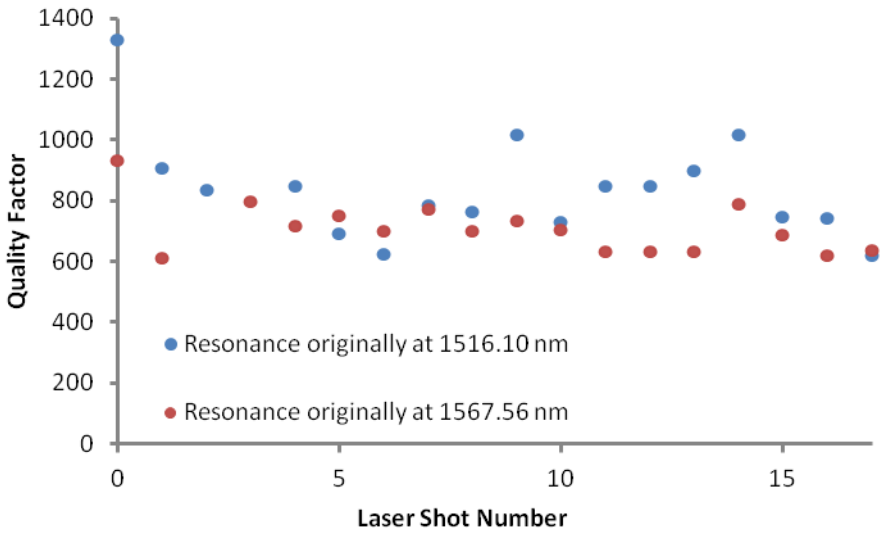

Figure 4.4: The quality factor of both the microring resonances recorded over the duration of the experiment.

4.6 Discussion of Results

In an attempt to explain the trend observed in Figure 4.3 for the shift in the microring resonances a thorough literature search was conducted. Atomic force microscopy (AFM) of the microring was also performed to investigate physical changes to the silicon surface.

The literature search results are discussed in detail in Chapter 3. To summarize, a silicon surface can be modified by a femtosecond laser pulse differently depending on the laser fluence used [60]. Specifically, at high laser fluences nanomilling takes place in which a thin layer of silicon is ablated from the surface. At lower laser fluences, no material is removed but a thin layer of crystalline silicon (c-Si) at the surface is converted into amorphous silicon (a-Si) in a process called amorphization. Here we exploited both of these mechanisms to tune the resonance of a silicon microring resonator in both directions, i.e., towards longer and shorter wavelengths. Ablation from the surface decreases the height of the waveguide, causing a decrease in the microring effective index which induces a blue shift in the resonance. Alternatively, modification to the crystal structure of silicon from c-Si to a-Si will cause an increase in the effective index of the waveguide due to the higher index of a-Si, thereby inducing a red shift in the microring resonance.

Two distinct modes of operation are discernable from Figure 4.3, one for laser fluences below about 0.20 J/cm^2 and one above this threshold. In the mode of operation below 0.20 J/cm^2 only red shifts in the resonances were observed. These shifts correspond to a change on the order of 10^{-3} in the effective index of refraction of the silicon waveguide core. The most likely physical mechanism for this change is a conversion of a thin layer of crystalline silicon at the top waveguide surface to amorphous silicon. From a single laser shot experiment on a blank Si substrate [65], it was reported that this amorphous layer is about 17 nm thick using 400 nm laser pulses. The conversion from c-Si to a-Si results in an increase in the effective index of the waveguide which would cause the red shift in the resonance observed. In the mode of operation above the 0.20 J/cm^2 threshold only blue shifts in the resonances were observed. The most likely physical mechanism responsible for the blue shifts is laser ablation of the surface of the waveguide. The ablation would cause a decrease in the height of the waveguide resulting in a decrease in the effective index of the waveguide, thereby causing a blue shift in the resonance. The blue shifts of approximately 8-10 nm in wavelength are consistent with simulation results for approximately a 2-3 nm decrease in the waveguide height in the microring waveguide.

Figure 4.3 shows that much larger red shifts were obtained for shots 1 and 15 compared to the other shots in the low fluence region, implying that there was a much higher amount of c-Si converted to a-Si for these two particular shots. For each femtosecond laser pulse to cause a change in the waveguide, it would have to melt the silicon at the surface of the waveguide regardless of whether it was crystalline or amorphous. Indeed for the first shot, there would be the highest amount of crystalline silicon available at the waveguide surface for conversion to a-Si, so it is reasonable that the initial shot would cause a larger red shift in the microring resonance than subsequent shots with an even higher fluence. This is because much of the laser pulse energy would be devoted to remelting the a-Si at the surface and thus less c-Si would be converted to a-Si with these laser shots even though the fluence was higher.

For shot 15, we note that it followed shot 14, which had likely removed a layer of material on the microring surface due to ablation since a blue shift was obtained. It was reported in [62] that when the laser fluence is above the ablation threshold, the molten silicon on the surface has enough time to cool and form poly-crystalline

silicon instead of amorphous silicon. Thus following shot 14, the microring surface had recrystallized so that more c-Si was available to be converted to a-Si during shot 15. This could explain the large red shift in the resonance observed for this shot.

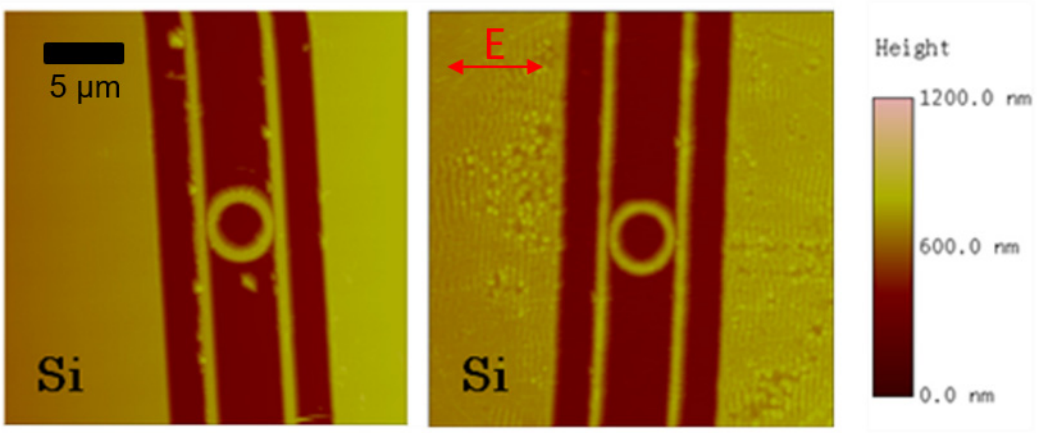

Figure 4.5: AFM images of the microring after multiple shots with (a) incident fluence no more than 0.15 J/cm^2 and (b) after the end of the experiment. The red arrow is the polarization of the electric field of the femtosecond laser pulse.

To confirm the physical origins for the red- and blueshift regimes of operation, atomic force microscopy (AFM) scans of the microring were taken before shot 13 and after shot 17. Figure 4.5 displays the results of two of these scans. Figure 4.5(a) shows the microring after laser shots with a fluence of no more than 0.15 J/cm^2. The image shows no variations or patterns on the silicon surface as a result of the laser shots. This is consistent with the assumption that amorphization of crystalline silicon has occured at these fluences. In this prcocess it is expected that the femtosecond laser pulse would produce a melt layer on the surface of the silicon waveguide which when it solidifies may slightly increase the surface roughness, but is not expected to change the silicon height. In this case, no significant change in roughness or height of the waveguides is detected supporting this conclusion. This also argees with TEM scans of silicon irradiated with similar wavelength and fluences [65].

However, the AFM scan in Figure 4.5(b) obtained at the end of the experiment shows that periodic ripples perpendicular to the laser's polarization direction, with a period that is on the order of the laser wavelength, have materialized on the silicon surface to the left and right of the microring device. These surface ripples appear only in the laser affected region which are indicative that ablation has occurred [60].

Thus, the AFM scans support our hypothesis for the physical origins of the red- and blueshifts observed. Because a fluence of about 0.20 J/cm^2 separates the amorphization regime from the ablation regime, it allows us to define this fluence to be the ablation threshold of our silicon device. This value is comparable with the ablation threshold reported in the literature for single shot ablation experiments on flat silicon wafers using 400 nm pulses [65].

We also monitored the quality factor of the microring resonator after each shot to ensure that the device response was not significantly degraded during the tuning. Figure 4.4 shows a plot of the extrinsic quality factor of the microring measured at both resonances after each shot. The plot shows that there was some drop in the quality factor of the resonator after the first shot, after which very little degradation occurred, even as the microring was ablated after shot 16. The decrease in the quality factor after the initial shot can be attributed to the increased absorption in the a-Si layer compared to c-Si as well as increased roughness caused by the amorphization of an initially smooth c-Si surface. Subsequent shots did not seem to incur additional roughness, as seen from the relatively constant quality factor after shot 1. The quality factor of the microring resonator used in this study was relatively low owing to its small size, so further study would be required to examine how femtosecond laser surface modification would affect the loss of a high-Q resonator.

In terms of stability, the resonance wavelengths of the ablated microring were observed to change by 10–20 pm over a period of several weeks. However, this change is also observed for a typical Si microring resonator without ablation and is normally attributed to the slight temperature variations in the laboratory from day-to-day. Therefore, the technique can be considered a permanent tuning technique.

4.7 Summary

The proof of concept experiment reported in this chapter demonstrated that we were able to shift the resonance of the microring resonator using 400 nm femtosecond laser pulses. The first laser shot at a fluence of 0.08 J/cm^2 induced a 4.4 nm red shift in the microring's resonance which corresponded to an increase in the waveguide effective index of 0.014. Subsequent laser shots at fluences between 0.06 J/cm^2 and

0.20 J/cm^2 saw small increases in the resonance wavelength while shots with fluences above 0.20 J/cm^2 were accompanied by large blue shifts in the microring resonance wavelength. At this point, we could conclude that femtosecond laser surface modification of silicon waveguides could provide coarse tuning of silicon photonic circuits. There were still many questions that this simple experiment was not able to answer. Further experiments are needed to address the repeatability of the technique, fine tuning, achievable tuning resolution, and possible application of the method to tune practical silicon photonic circuits.

The work described in this chapter was published in Optics Letters in 2011 [36] and presented at IPR in 2011 [77].

Chapter 5

Single shot femtosecond laser tuning of silicon microring devices

5.1 Experiment Design and Goals

The proof of concept experiment in the previous chapter showed that it was possible to tune silicon microring resonators with 400 nm wavelength femtosecond laser pulses. However, the experiment was based on irradiation of the microring using several femtosecond laser pulses on the same spot at varying fluences which gave unreliable shifts. The goal of this experiment was to determine if single femtosecond laser pulses of different fluences on previously unmodified sections of waveguide would have a different effect and to find out if the results of the proof of concept experiment were repeatable. Tests were also conducted to see if the technique would also work on devices with an oxide cladding layer.

5.2 Devices with no cladding

5.2.1 Microring resonator characterization

Seven all-pass silicon microrings were fabricated on the same SOI chip with separate input/ouput waveguides for the femtosecond laser tuning experiments. Each silicon microring had a 15 μm radius and was coupled to a single bus waveguides via a coupling gap of 410 nm. Both the bus and microring waveguides were 310 nm wide by 340 nm tall and were operated in the TM mode (cross-sectional diagram in Figure 5.1 (b)). The devices were left air cladded. A scanning electron microscope (SEM)

image of one of the fabricated microrings is in Figure 5.1 along with a cross-sectional diagram of the silicon waveguides.

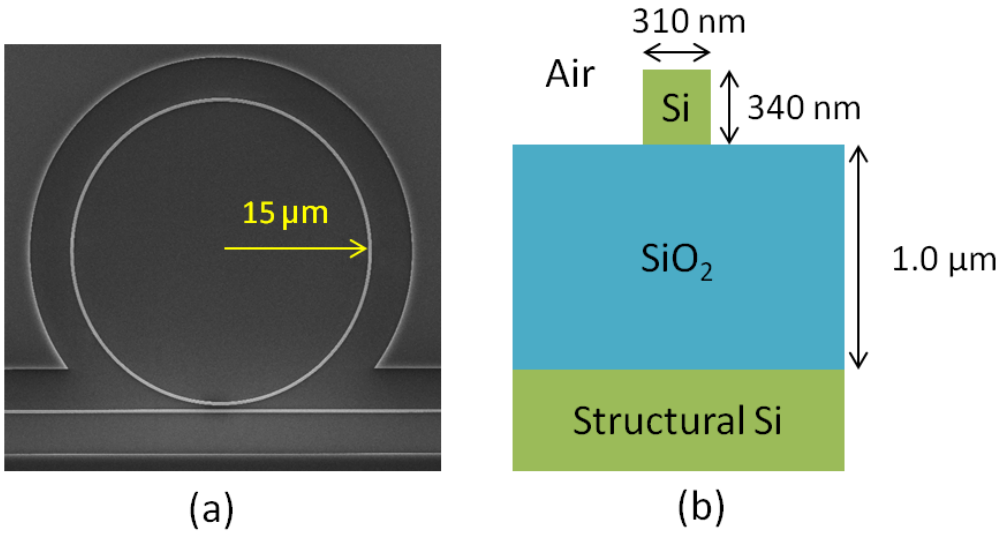

Figure 5.1: (a) SEM image of one of the 15 µm radius microrings used in the femtosecond laser tuning experiment. (b) Cross-sectional schematic of the silicon waveguides fabricated for the experiment.

The characterization of the microring devices was carried out using a continuous-wave tunable laser (Santec TSL-210V) swept over wavelengths in the 1535-1565 nm range. The laser light was adjusted to TM polarization using a polarization cube and polarization controller and then butt coupled to both waveguide end facets using lensed fibers aligned by 3D stages controlled by piezo-electric motors (Newport NanoPZ series). The output of the chip was then fed to a power meter. A diagram of the setup is in Figure 5.2. The limit of detection in the resonance wavelength for this setup using the 15 µm radius microrings was about 0.02 nm since a temperature controlled stage was not used. The temperature of the lab would vary slightly throughout the day and this would typically cause spectral variations of about 0.01 to 0.02 nm in the measured spectrum. Therefore it was not posssible to detect changes in the resonance wavelength smaller than this. For most the experiments in this thesis, the changes to the microring resonance wavelength were significantly larger than this.

A sample wavelength sweep of one of the microrings before the tuning experiment is shown in Figure 5.3. The periodic flucuations of about 5 dB in the through port response of the chip are due to the waveguide end facet reflections and are modelled

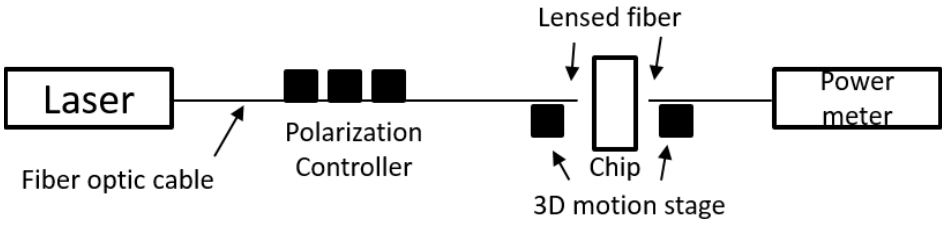

Figure 5.2: Diagram of the measurement setup.

in detail in Chapter 2.

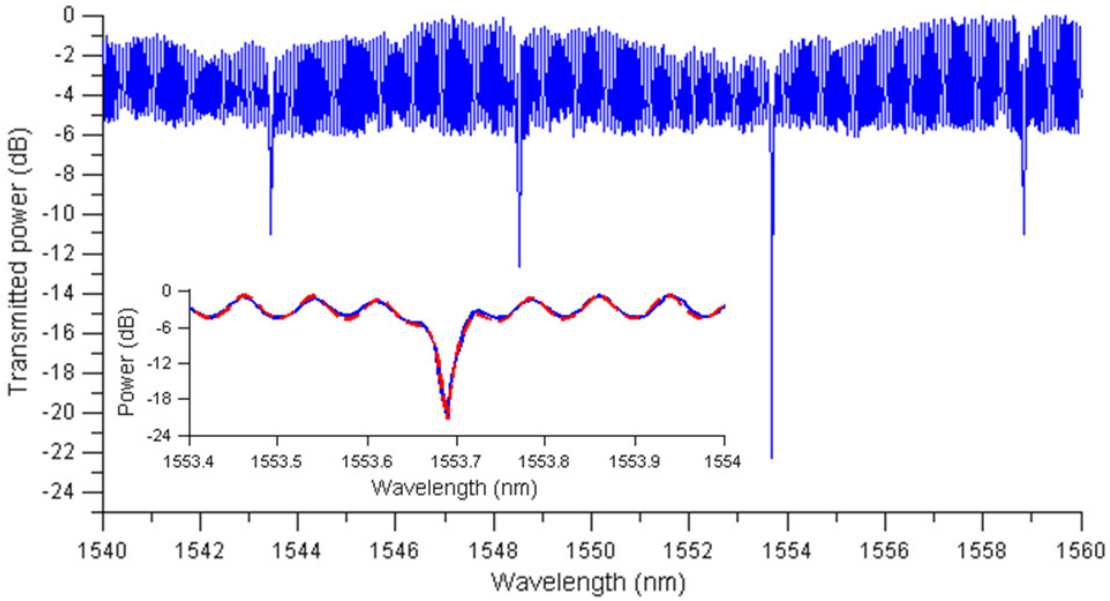

Figure 5.3: Measured initial spectrum of one of the microrings used in the tuning experiment. Inset: One of the measured microring resonances (blue, solid) and the curve fit (red, dashed).

To extract the device parameters, curve fitting of the measured data was performed using the total chip response represented by equation 2.7. As discussed, this equation takes into account the modified microring resonator spectrum due to the reflections from the chip's end facets. The curve fitting was accomplished using a MATLAB program that minimizes the residual between the measured data and the curve fit. A sample curve fit near one of the microring resonances is shown in the inset of Figure 5.3.

From this curve fitting, the average initial values for the transmission coefficient, τ, and the roundtrip field attenuation factor, a_{rt}, were determined to be 0.972 and

0.986 respectively. This gave the microrings an average loaded quality factor of about 25,000 and intrinsic quality factor of 75,000 with a roundtrip loss of 0.12 dB. The microrings also had a free-spectral-range (FSR) of about 5 nm.

5.2.2 Laser beam characteristics

For this experiment, 400 nm femtosecond pulses were used and the aparatus described in Chapter 3, Figure 3.1 was used to direct them to the chip. The pulses were imaged onto the chip after passing through a 500 μm pinhole aperture to create a top-hat beam profile with a radius of about 8.8 μm. This made the beam spot much smaller than microring diameter so that the same microring could be shot multiple times, while the use of the top-hat profile ensured that the entire laser spot would be affected by a constant laser fluence.

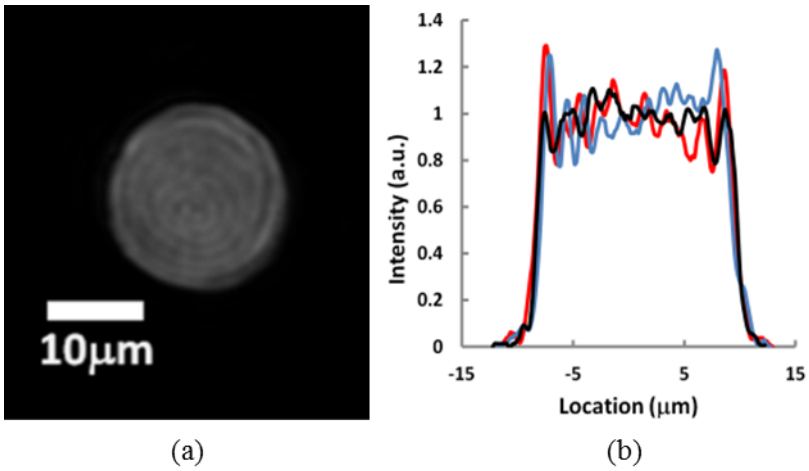

Figure 5.4: (a) CCD image of the femtosecond laser "top-hat" beam profile when the device was at the best image plane. (b) The horizontal line-out across the center of the beam when the device was at the best image plane (black line), and 2 μm in front (blue) or after (red) it.

The top-hat beam profile is very sensitive to being in its best image plane. Figure 5.4 (a) shows a CCD image of the beam at its best focus. Figure 5.4 (b) shows a lineout through the center of the beam at the best focus, and 2 μm in front and 2 μm behind the best focus. At the best image plane the top-hat beam has a nearly flat profile, but just 2 μm off focus fluctuations in the intensity of more than 20% begin to appear, especially near the edges of the beam spot. As will be seen this affects the uniformity of the amorphization region

5.2.3 Tuning results: Resonance Shift

Six of the microrings were subjected to femtosecond laser irradiation during the experiment while one was left unmodified as a control. After the initial characterization of the devices, each microring was irradiated with a single laser pulse at varying fluences. The microrings were then measured and characterized again, and irradiated with a second laser pulse on an unmodified section of the microring waveguide. Figure 5.5 (a) displays the results for the resonance shift of each microring as a function of laser fluence. The horizontal error bars are due to the uncertainty in the energy calibration and the exact size of our laser spot. The vertical error bars are mainly due to our approximately $\pm$ 2 μm accuracy of aiming the center of the laser spot onto the waveguide, resulting in some uncertainty in the length of the microring waveguide segment affected by the shot.

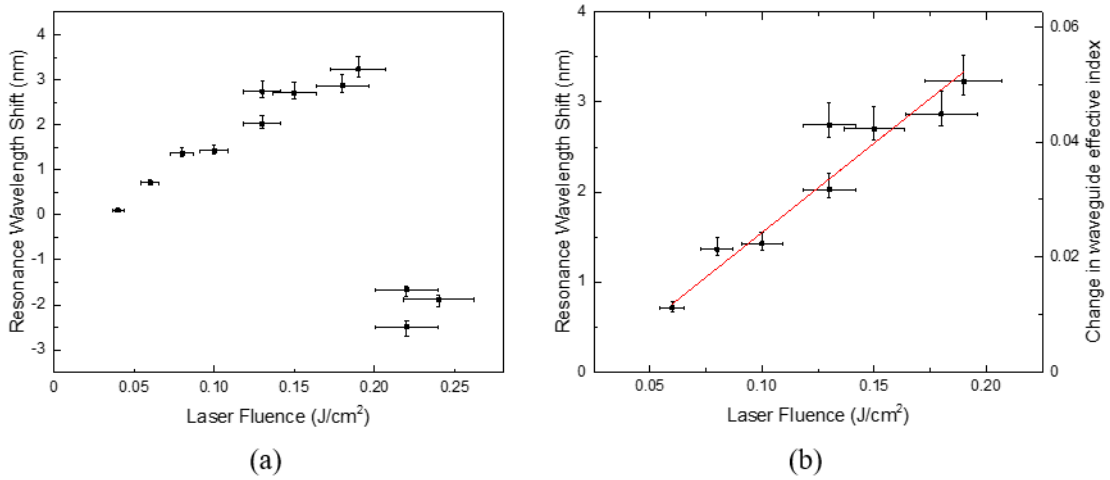

Figure 5.5: (a) Resonance wavelength shift of the microring resonators as a function of laser fluence. (b) Linear fit of the positive resonance shifts and change in the waveguide effective index as a function of the laser fluence. The data point at 0.04 J/cm^2 is removed for reasons discussed in the text.

Figure 5.5 (b) shows the change in the effective index of the section of waveguide amorphized by the laser pulse. The effective index change was computed from the resonance wavelength shift by

$$\Delta n_{\text{eff}} = \frac{\Delta\lambda}{\lambda_o} \cdot \frac{2\pi \mathrm{R}}{l} \cdot n_g \tag{5.1}$$

where λ_o is the original resonance wavelength of the microring, $\Delta\lambda$ is the resonance wavelength shift, R is the microring radius, l is the length of the modified section of microring waveguide, and n_g is the group index of the waveguide. This equation is a modification of equation 4.1 which assumes that all of the microring waveguide is being modified whereas this equation allows for a section of the microring to be illuminated. For the dimensions of SOI waveguides used in this experiment, the effective index of the TM mode was determined to be 2.3 using a Finite Difference mode solver.

Figure 5.5 (a) shows that by changing the fluence of the laser pulse it is possible to control the direction and extent of the resonance wavelength shift. The positive shifts in the resonance wavelength at fluences below 0.2 J/cm^2 are due to amorphization of a small amount of the crystalline silicon at the waveguide surface. This layer of amorphous silicon has a higher index of refraction than the original crystalline silicon, leading to an increase in the effective index of the waveguide. The negative shifts in the resonance wavelength at fluences above 0.2 J/cm^2 are due to ablation of a small amount of material off the top of the waveguide. This causes a decrease in the waveguide height which results in a decrease of the effective index of the waveguide. The $\sim$0.20 J/cm^2 threshold for laser ablation of silicon at the 400 nm wavelength is consistent with the proof of concept results in the previous chapter [36]. In the ablation regime, the minimum negative shift in the resonance wavelength was -1.7 nm, corresponding to a change in the waveguide effective index of -0.013. It was observed in our previous experiments that ablation only a few hundredths of a J/cm^2 above the ablation threshold could be damaging to the waveguide resulting in significantly increased loss so laser shots at higher fluences were not attempted.

In our proof of concept work, we determined the amorphization threshold to be 0.06 J/cm^2 whereas here we observed amorphization at an average fluence of 0.04 J/cm^2. This discrepancy is presumably due to small fluctuations in the beam profile which caused the local fluence to be well above 0.04 J/cm^2 leading to amorphization in some small regions near the edge of the beam spot. As seen in Figure 5.4 (b), the fluence fluctuations were even more pronounced if the device was not placed in the proper image plane. This effect was also observed visually through a change in the colour for only small regions within the spot size, as seen through an optical

microscope.

In the amorphization regime (laser fluence below 0.20 J/cm^2 and above 0.06 J/cm^2) there appears to be a linear correlation between the resonance wavelength shift and the laser fluence. The data point at 0.04 J/cm^2 was not included in Figure 5.5 (b) because only a small portion of the laser spot caused amorphization and the length of waveguide changed is therefore unknown (for use in equation 5.1). Assuming a linear relationship in Figure 5.5 (b) we obtain a tuning rate of 20 ± 2 nm/J·cm^{-2} (or $\Delta n_{\text{eff}} = 0.032 \pm 0.04$ per J/cm^2 for the length of waveguide affected by the pulse) above the amorphization threshold of 0.06 J/cm^2.

There are three possible explanations for the linear correlation between the wavelength shift and laser fluence in the amorphization regime. The first hypothesis is that as the fluence increases, the depth of the amorphized silicon layer also increases. It is reasonable to assume that a higher laser fluence will cause a larger volume of crystalline silicon near the surface of the waveguide to melt, resulting in a thicker layer of amorphous silicon (the waveguide width being fixed). This hypothesis is supported by J. Bonse [61], who optically characterized the depth of amorphous silicon from an 800 nm, femtosecond Gaussian laser pulse. Assuming that the refractive index of the amorphous silicon does not depend on the laser fluence, it was concluded that the depth is likely dependent on the laser fluence used. The second possibility is that the volume of the amorphous silicon created stays constant with changing laser fluences, but the refractive index of the amorphous silicon is modified instead. This hypothesis is supported by the work of Izawa et. al [65, 66] where it was shown using TEM that the depth of amorphous silicon produced using 400, 800, and 1550 nm laser pulses did not vary with the number of laser pulses or laser fluence below the ablation threshold (ref [65]. reports the depth of amorphous silicon to be 17 nm when irradiating crystalline silicon with a single 400 nm femtosecond laser pulse). However, in a later publication, Izawa et. al [64] also showed that for 266 nm laser pulses the depth of amorphous silicon does vary over a Gaussian spot size. Although it is noted in many publications that the index of amorphous silicon is highly dependent on the manner in which it is produced [78, 79], to our knowledge and also noted in ref [61], there has been no study of the change in refractive index of amorphous silicon produced by femtosecond laser shots of various fluences. Thus further studies are needed

to confirm the second hypothesis. The third option is a combination of increased amorphization depth along with increased index of refraction at higher laser fluences, which is the most probable explanation given the evidence in the literature.

Stress induced in the waveguides by the femtosecond laser pulses was also explored as a possible mechanism for change in the waveguide effective index observed in the experiment. However, for reasonable values of stress induced in the silicon waveguide's, the effective index change observed in multiphysics simulations was observed to be over an order of magnitude lower.

For this experiment, when the entire spot size was above the amorphization threshold, we achieved a minimum positive resonance wavelength shift of 0.71 nm using a fluence of 0.06 J/cm^2. This corresponds to a minimum change of 1.1×10^{-2} in the waveguide effective index. However, the data point at 0.04 J/cm^2 shows the tuning resolution of the technique using this set-up can be smaller. Due to the shorter affected length of waveguide, a shift in the resonance of 0.10 nm was observed for this shot, which is roughly 1.5× the bandwidth of these microrings. This shift cannot be converted to a change in the effective index because the length of waveguide affected is uncertain, but it illustrates that the shift is dependent on the length of waveguide affected. The resolution of the technique will ultimately be dependent on the ratio of length of waveguide affected by the laser pulse to the circumference of the microring, which is evident from equation 5.1. Therefore, the technique's resolution can be made very fine by using a very small spot size or only part of the spot size. The tuning rate obtained in Figure 5.5 (b) can be modified in the same manner as the tuning resolution. The spot size of the laser pulse, along with the accuracy of the alignment stage, is the limiting factor for fine tuning with this technique.

5.2.4 Tuning results: Loss

Measurements of the roundtrip loss in the microring resonators also allowed us to investigate the effect of the laser pulse irradiation on the waveguide loss. The initial roundtrip loss of the microring resonators averaged over four resonance dips between 1540 and 1560 nm was found to be 0.25±0.05 dB. The large variation in the roundtrip loss recorded over several resonance dips of the same microring is most likely due to coherent backscattering [80–82], an effect which has been reported for microrings very

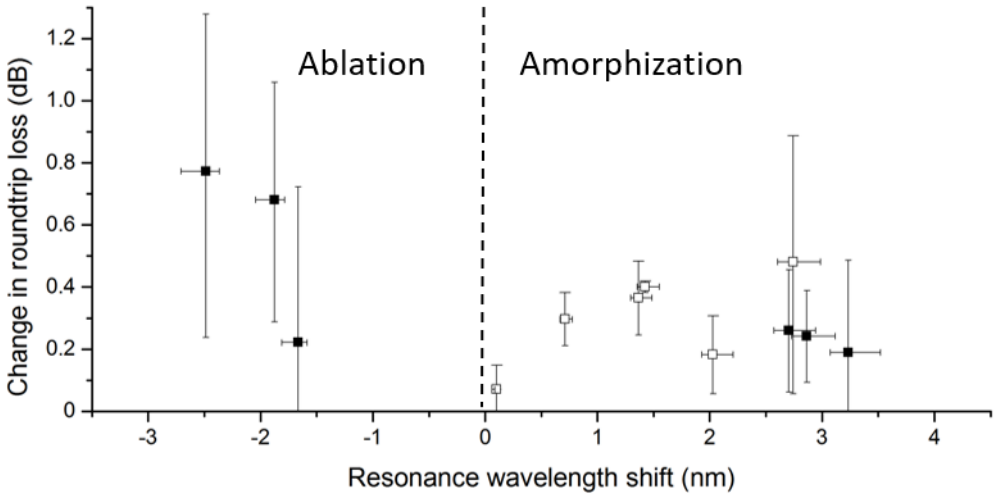

Figure 5.6: Change in the roundtrip loss of the microrings following irradiation from single pulses plotted as a function of the resonance wavelength shift. Negative shifts represent ablation and positive shifts represent amorphization of the waveguide. The open and closed data points represent the first and second shots on the microrings respectively.

similar to ours [83]. Coherent backscattering is caused by the sidewall roughness of the microring waveguides. In a normal waveguide the backscattering is random and incoherent and therefore does not alter the spectral characteristics of the waveguide except for providing a low amount of background white noise. In a microring, the backscattering is amplified and can become coherent because the light in the microring will make multiple passes over the same section of waveguide that is causing the backscattering. Since the backscattering is still a random process, the amount of backscattering will vary from resonance to resonance and creates the variations in the spectral response of the microring that is measured as fluctuations in the roundtrip loss of the microring.

In Figure 5.6 the change in the average roundtrip loss is plotted versus the resonance wavelength shift induced by each shot. The error bars represent the standard deviation of the initial roundtrip loss measured for four resonance dips between 1540 and 1560 nm that is added in quadrature with the same value for the final roundtrip loss. In the amorphization regime (positive resonance shifts), it is observed that the roundtrip loss increased with every laser shot, which is expected since amorphous silicon has larger absorption than crystalline silicon [79]. However, there appears to be no definite correlation between the loss and the laser fluence and the error bars are

fairly large and vary significantly in magnitude. The large error bars cross below zero for some data points, but no single measurement indicated a decrease in loss. The lack of a definite trend combined with the large fluctuations in the loss data suggest a dominant contribution from amplification of the coherent backscattering effect that was already present in the silicon waveguides before the laser shots. When a laser pulse amorphizes some of the silicon, it may roughen the top surface of the waveguide and/or produce volumetric index inhomogeneities due to mixtures of amorphous and crystalline Si. This roughness could increase the backscattering and cause large fluctuations in the measured roundtrip loss at different resonances as observed. The effect could also be amplified for the TM polarization since it is more sensitive to roughness on the top surface of the waveguide than on the sidewalls. This hypothesis is supported by the much larger increase in loss and the larger fluctuations in its measurement for shots above the ablation threshold (negative shifts in the resonance wavelength in Figure 5.6) together with evidence from AFM scans of unpatterned silicon surfaces after ablation that showed an increased surface roughness [36].

Overall in the amorphization regime, the induced loss in the waveguide is below 0.5 dB per shot. This amount of loss is likely not tolerable in tuning of high quality factor microring devices because the l aser pulse will significantly alter the filter's spectral response. However, it may be acceptable for other applications like tuning of low quality factor microring devices or Mach Zehnder interferometers. In these devices, the spectral response is less dependent on the loss in the device and it should not alter the device response too much by increasing the loss less than 0.5 dB.

5.3 Devices with a cladding

In most practical applications of silicon photonic integrated circuits, the silicon waveguides will be covered by a cladding layer. This is to protect the waveguides from exposure to the environment or because other layers of either electronics or photonics will be built on top. Therefore, for our technique to be useful for tuning practical silicon photonic devices it must be also work through a cladding layer.

5.3.1 Microring resonator characterization

Microring resonators 15 µm in radius were fabricated in the exact same manner as the microrings in the previous section. However before cleaving the chip for characterization, 1.8 µm of SiO_2 was deposited over top of the device by plasma enhanced chemical vapour deposition (PECVD). A cross sectional diagram of the waveguide is shown in Figure 5.7 (a) and an SEM of the waveguide end facet is in Figure 5.7 (b).

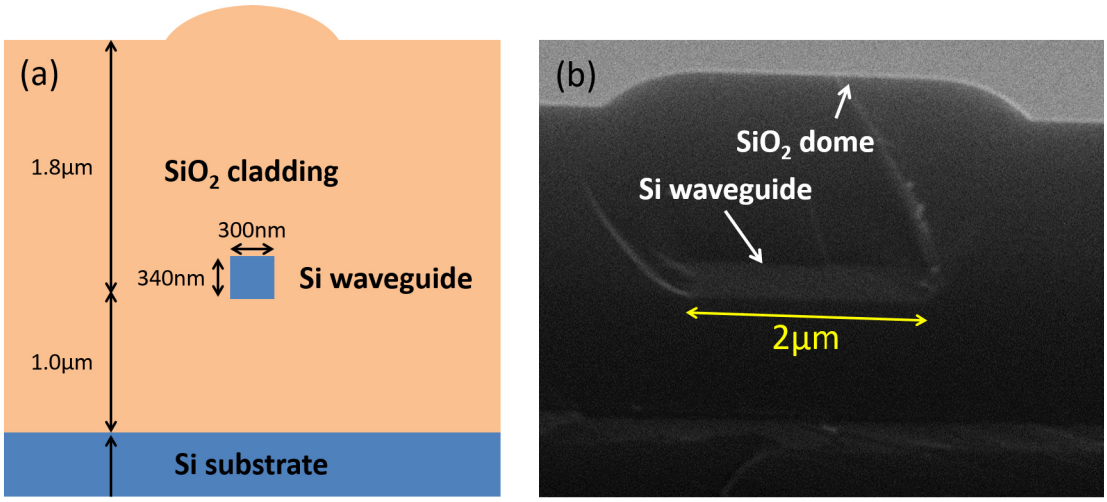

Figure 5.7: (a) Cross section of the silicon waveuide after the addition of a 1.8 µm SiO_2 cladding layer. (b) SEM of the waveguide end facet. The silicon waveguide is the faint rectangle in the middle of the picture which is surrouned by a SiO_2 cladding layer.

After the deposition of 1.8 µm of SiO_2, the Si waveguide was completely surrounded by SiO_2. Such a thick cladding layer was deposited to ensure that any changes to the waveguide effective index induced by the femtosecond laser pulse would be caused at the silicon surface and not the surface of the SiO_2 layer since the light field is much reduced at the latter surface. PECVD is a conformal deposition process which caused a small SiO_2 dome to form above the silicon waveguide and it is clearly visible in the SEM picture of the waveguide end facet in Figure 5.7 (b). The height of the dome is the same as that of the silicon device layer. This dome modified the effective fluence of the laser pulse received by the silicon core, as will be discussed later.

To extract the device parameters, curve fitting of the measured data was performed using the total chip response model represented by equation 2.7. From this curve fitting, the average initial values for the transmission coefficient, τ, and the roundtrip

field attenuation factor, a_{rt}, were determined to be 0.938 and 0.974 respectively. This gave the microrings an average loaded quality factor of about 17,000 with a roundtrip loss of 0.22 dB. The microrings also had a free-spectral-range (FSR) of about 5.5 nm. The addition of the cladding caused the coupling into the microring and roundtrip loss to increase versus the devices in section 5.2.1 with no cladding. The coupling has increased because the cladding reduces the waveguide index contrast and thus the evanescent field penetrates farther into the cladding layer which increases coupling to nearby waveguides. The increase in the waveguide loss is likely due to increased absorption in PECVD oxide layer versus the air cladding.

5.3.2 Laser beam characteristics

For this experiment, 400 nm femtosecond pulses were used and the aparatus described in Chapter 3, Figure 3.1 was used to direct them to the chip. The pulses were imaged onto the chip after passing through a pinhole aperture to create a top-hat beam profile with a radius of about 5.5 μm. This made the beam spot much smaller than microring diameter so that the same microring could be shot multiple times on fresh locations, while the use of the top-hat profile ensured that the entire laser spot would be affected by a constant laser fluence. As discussed in section 5.2.2, the top-hat beam profile is very sensitive to being in the location of the best image plane and fluence fluctuations of up to ±15% were observed in the beam's best image plane.

5.3.3 Tuning results: Resonance shift

Figure 5.8 shows the resonance wavelength shift of the microring as a function of the incident laser fluence as well as the corresponding change in the waveguide effective index in the region affected by the laser pulse (calculated from equation 5.1). For comparison, the change in the effective index of the unclad microring waveguide is included as well. We observe that for all the fluence values studied for the clad microrings, the laser pulse induces a red shift in the microring resonance, which likely corresponds to an increase in the waveguide effective index due to amorphization of the Si waveguide surface. At laser fluences just above the threshold (0.03 J/cm^2) to approximately double the threshold fluence (∼0.07 J/cm^2), there appears to be a linear correlation between the resonance shift and the laser fluence, which is consistent

with previous results for unclad samples. However at laser fluences about twice the threshold, this relationship breaks down and the observed resonance shifts begin to decrease with increasing laser fluence. Laser pulses below the threshold had no effect on the resonance of the microring and laser pulses above 0.15 J/cm^2 induced too much loss in the waveguide for the resonance to be tracked.

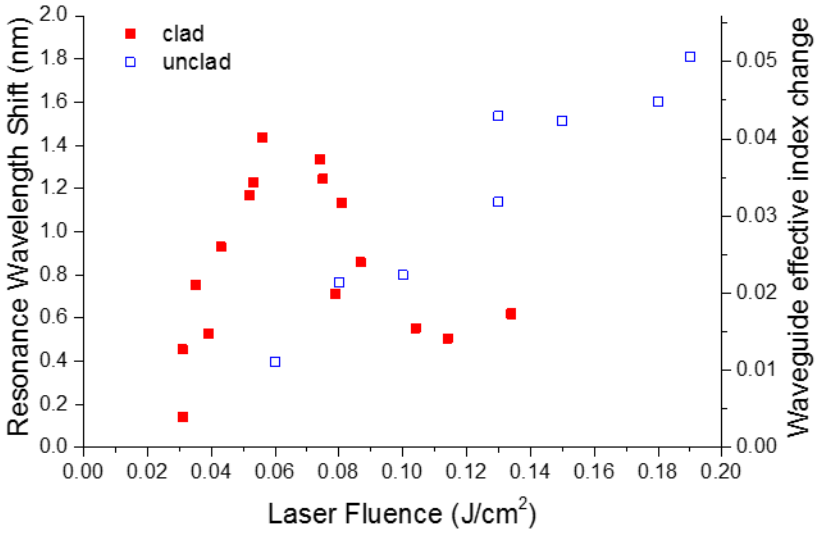

Figure 5.8: Experimental resonance shift data of clad microrings (red squares). The right axis is the corresponding change in the waveguide effective index for the clad microring waveguides. The experimental data for the effective index change for the unclad miroring waveguides from the previous section is included for comparison (open blue squares).

Comparing the clad and unclad experimental data, the threshold fluence for the clad experiment was determined to be about 0.03 J/cm^2 which is about half the threshold fluence of the unclad microring waveguides. The slope of the data in the linear region for the clad microring data is also about twice that of unclad microring data. This may be explained by the bubble that formed above the microring waveguide due to the conformal PECVD deposition. Finite difference time domain (FDTD) simulations were conducted to investigate the effect that this dome would have on the fluence of the laser pulse at the surface of the waveguide. Figure 5.9 shows the results of a simulation of a 400 nm plane wave incident on the dome. The dome shape is assumed to be flat over top of the silicon waveguide and the edges are approximated by a circular curvature.

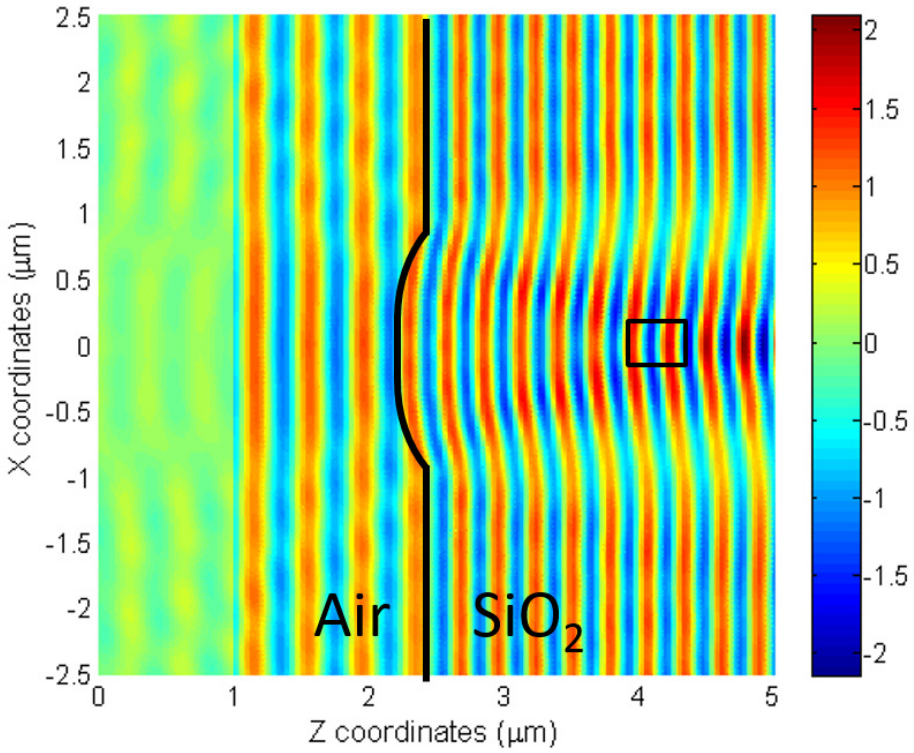

Figure 5.9: FDTD simulation of a 400 nm plane wave incident on the surface of the waveguide structure in Figure 5.7 (a). The black overlay outlines the shape of the SiO_2 dome and the location of the Si waveguide.

The FDTD simulations showed that there was an enhancement of 1.6-2.3 in the intensity of the laser pulse at the surface of the silicon waveguide depending on the radius of curvarture for the SiO_2 dome edges chosen. The radius of curvature was varied over a range based on measurements from Figure 5.7 (b). Direct measurements of the size of the curved region gave the high values for the increase in intensity while estimation of the size of the curved region from the total size of the dome gave the low values. This varied the radius of curvature of the lens from 0.8 μm to 1.1 μm. All of the measurements were taken from the cross-sectional SEM of the end facet of a 2 μm waveguide section and extrapolated to a 300 nm wide waveguide section because no direct measurements of a 300 nm wide waveguide cross-section could be made.

The simulated enhancement agreed well with the experimentally observed enhancement of approximately 2. This result leads to the conclusion that the lower observed threshold fluence was likely due to a lensing effect from the SiO_2 bubble and

not from the addition of the SiO_2 cladding directly. The conclusion is also supported by observations from the experiment on the unclad devices where it was observed that for below threshold pulses, no color change was seen to occur on the buried silicon layer underneath the SiO_2 buffer layer. The results from the unclad microring experiment can now be scaled by a factor of 2 to give both experiments approximately the same threshold values. The clad and unclad microring data can now be more directly compared in Figure 5.10.

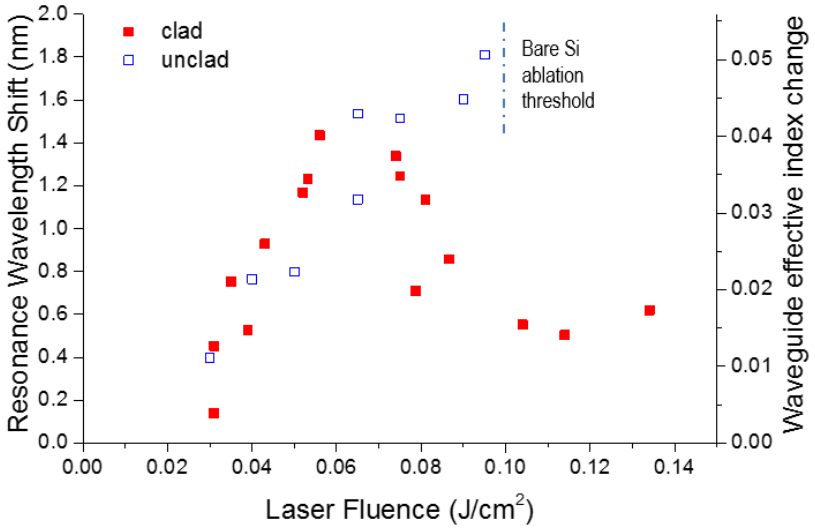

Figure 5.10: Experimental resonance shift data of clad microrings (red squares). The right axis is the corresponding change in the waveguide effective index for the clad microring waveguides. The incident fluence values of the effective index change data for the unclad miroring waveguides from the previous section is scaled down by a factor of 2 for a direct comparison (open blue squares).

The slope of the linear region for the clad microring data can now be seen to correlate very well with the slope for the unclad microring data. This correlation likely means that the mechanism for the change in the waveguide effective index is the same as for the unclad waveguides. This mechanism has been discussed in detail in section 5.2.3.

At about 0.07 J/cm^2, the linear trend reverses and the wavelength shift begins to decrease with increasing fluence and then evenually levels out. Our previous experiment on unclad microrings yielded a laser ablation threshold of 0.20 J/cm^2, which

when adjusted for lensing effect should be about 0.10 J/cm^2 for clad samples. However, Figure 5.10 shows it is possible to exceed this threshold on the clad samples without causing ablation of the Si waveguide because of the higher required energy to break the SiO_2 layer. This reverse trend in the effective index change is likely caused by stress and resolidification conditions in the Si waveguide [84]. Increasing the laser pulse energy should heat the waveguide surface to higher temperatures which should also increase the pressure in the silicon. The expansion of this heated silicon is opposed by the SiO_2 layer which may amplify any induced stress inside the a-Si layer created, and possibly change the amount of a-Si formed due to different resolidification conditions. The stress may play a larger role in this case because the SiO_2 cladding layer will prevent any expansion of the waveguide due to the formation of the a-Si layer.

5.3.4 Tuning results: Loss

After each laser shot, the roundtrip loss of each microring was determined by fitting the measured response with equation 2.7. The loss induced by each laser shot was plotted in Figure 5.11 (a). The data follows a similar pattern to the resonance wavelength shift observed in Figure 5.10. Between 0.03 and 0.07 J/cm^2, there is an increasing trend in the amount of loss versus laser fluence. The loss then decreases and becomes relatively constant with fluence before increasing significantly at 0.14 J/cm^2.

It is noted that for this particular experiment there was not the same problem of backscattering causing a large variance in the roundtrip loss values obtained over many resonances in the same microring as there was for the unclad case. The backscattering may have been reduced because of the lower starting quality factor of the microrings (17,000 vs. 25,000) [83] and/or because the SiO_2 cladding prevented the melt layer from resolidifying with a small increase in surface roughness at the top of the waveguide.

In the linear shift region circled in Figure 5.11 (a), there seems to be a relationship between increasing loss with increasing fluence. The data in the circled region in Figure 5.11 (a) is replotted in Figure 5.11 (b) to highlight this. As the laser fluence was increased, the trend was for the induced loss to also increase. This also follows

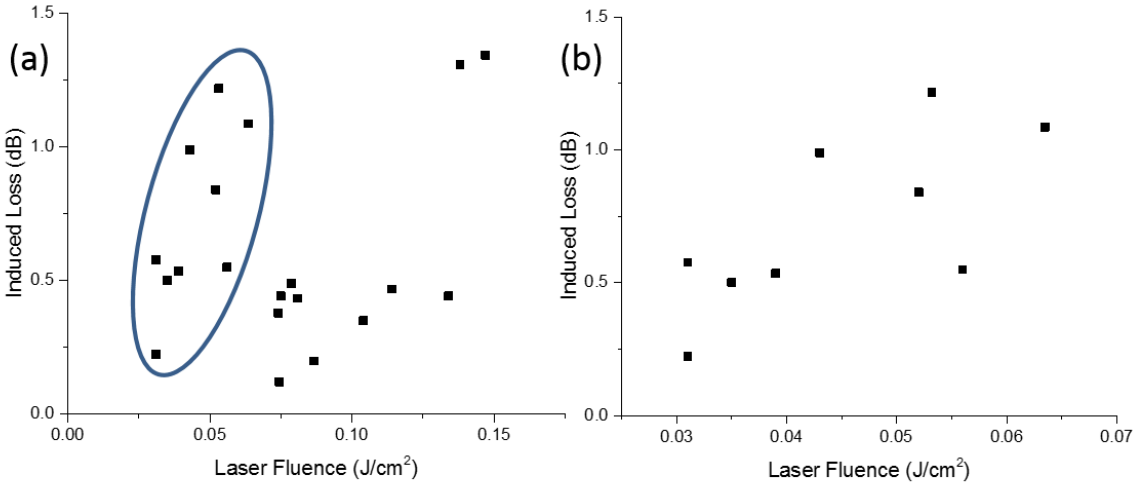

Figure 5.11: (a) The increase in loss measured for the microrings after each laser shot as a function of fluence. The blue oval indicates the data used in (b) for increase in loss measured for the microrings after each laser shot for the linear shift region between the threshold and about 0.07 J/cm^2.

the data in Figure 5.10 where the resonance wavelength shift increased over the same range of laser fluences. This trend would be expected because as the amount of a-Si in the waveguide increases the amount of absorption in the a-Si would also increase. This trend was not observed in Figure 5.6 for the unclad data because of the backscattering effect in the microring, but without that effect the trend can be observed here.

At laser fluences above the linear shift region, the loss decreased and then eventually increased to a point where the laser pulses induced so much loss in the microrings that the resonances disappeared from the spectral response of the device. Since this region would not be used for tuning these results are not important.

5.4 Summary

In this chapter, it was shown that single femtosecond laser pulses of varying fluences can be used to trim silicon waveguides both with and without a SiO_2 cladding layer. For the unclad devices, the effective index change increased linearly with increasing fluence in the positive wavelength shift regime between fluences of 0.06 and 0.20 J/cm^2 and the effective index change was negative for fluences above 0.20 J/cm^2. For the clad devices, there was a linear increase in the effective index change between

fluences of 0.03 and 0.07 J/cm^2 after which the trend reversed and the effective index change became nearly constant with increasing fluence. For all laser shots on both clad and unclad devices, the roundtrip loss of the microring increased. In the region of linear index shift for the clad devices, the roundtrip loss magnitude also increased as the laser fluence increased. There was no observable trend in the roundtrip loss for the unclad devices due to the coherent backscattering effect in silicon microring resonators.

The work on the unclad devices in this chapter was published in Optics Express in 2013 [37] and presented at CLEO:PR in 2013 [85]. The work on the clad devices was presented at CLEO in 2014 [38].

Chapter 6

Fine tuning with a Gaussian beam

6.1 Motivation

In the previous chapter, it was shown that microring devices both with and without a cladding layer could be trimmed by single femtosecond laser pulses. However, the technique as demonstrated with a top-hat beam profile could not affect a small enough section of waveguide to be useful for fine tuning applications. Equation 5.1 illustrates that in order to effect very small changes in the resonance wavelength of the microrings that one would have to make the beamspot also very small. A top-hat beam profile can only be made so small due to diffraction, but a Gaussian shaped beam spot can affect a much smaller area due to the rolloff from the center of the beam. Therefore for any reasonably small Gaussian shaped beam spot at low energy, only very small areas in the center of the beam spot would have a fluence above the amorphization threshold effectively making the beam spot very small. In this chapter, very fine tuning of silicon microring resonators is demonstrated. The effect that the laser wavelength has on the resonance wavelength shift is also explored by switching to the fundamental harmonic of the femtosecond laser, 800 nm, from the second harmonic, 400 nm. The threshold fluence for change at both wavelengths can also be accurately determined by measuring the resonance wavelength shifts.

6.2 Laser beam characteristics

The femtosecond laser tuning apparatus in Figure 3.1 was used to perform the tuning experiment. Quasi-Gaussian beam profiles were created by selecting the center part

of the initially Gaussian beam profile of the laser with a pinhole aperture and focusing it to the substrate surface. For 400 nm pulses this created a quasi-Gaussian beam profile with an e^{-2} radius of 6.2 μm while for 800 nm pulses the radius was 13.1 μm. Images of the beam profiles are in Figure 6.1.

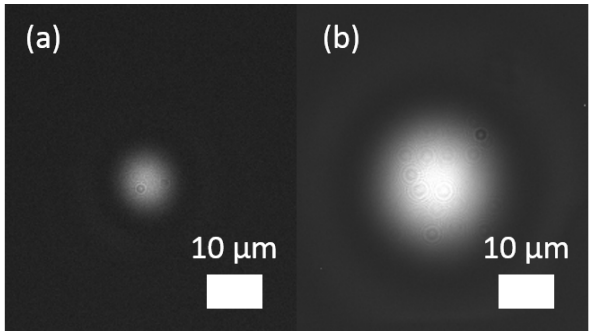

Figure 6.1: (a) 6.2 μm radius 400 nm beam spot. (b) 13.1 μm radius 800 nm beam spot.

6.3 Microring resonators

The silicon microring resonators used for this tuning experiment were very similar to the microring resonators used in the previous chapter. The microrings were made with a radius of 15 μm and waveguide cross-sections of 300x340 nm^2 with no cladding layer over top (air clad). The microrings were designed to be over coupled with a coupling gap of 370 nm which yielded a τ of 0.962 while a_{rt} was 0.977 initially.

6.4 Expected 400 nm tuning curve

The expected trend for the microrings' resonance shift after irradiation by Gaussian shaped femtosecond laser pulses can be derived analytically based on the previous results from the tophat beam shape experiment.

Figure 6.2 (a) shows the linear dependence of the waveguide effective index on the laser pulse fluence in the amorphization regime as experimentally observed in Figure 5.5 for the tophat beam experiment. The minimum change in effective index (Δn_{min}) at the threshold fluence (F_{min}) is labelled on the plot. The slope of the line is labelled as x. This trend can now be described mathematically by the following relationship where the change in the waveguide effective index is a function of the applied laser fluence.

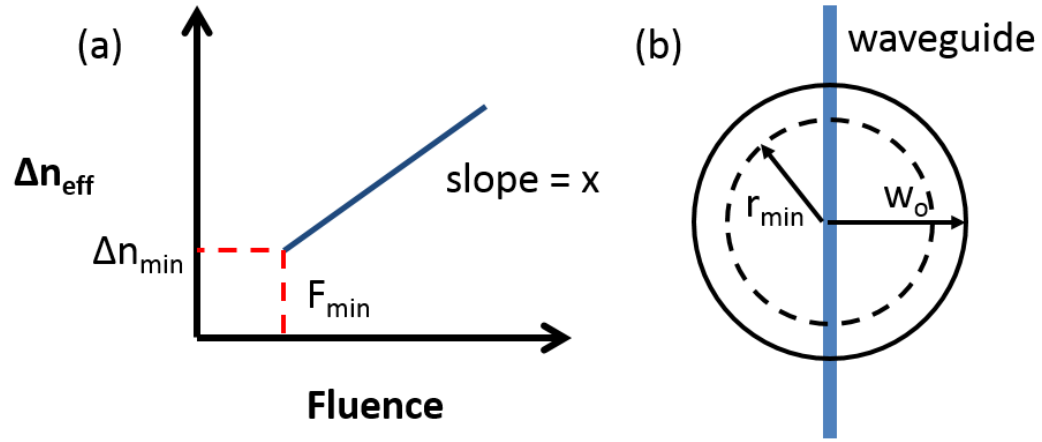

Figure 6.2: (a) The change in the waveguide effective index as a function of the applied laser pulse fluence from the tophat beam shape tuning experiment. The blue line is the observed linear trend. (b) Illustration of the length of waveguide affected by the Gaussian beam spot. The blue section is the waveguide, w_o is the beam radius (e^{-2}), and r_{min} is the radius of the beam spot above the minimum fluence for amorphization.

$$\Delta n_{\text{eff}}(\text{F}) = x(\text{F} - \text{F}_{\text{min}}) + \Delta n_{\text{min}} \tag{6.1}$$

The goal of this analysis is to find what the change in the resonance wavelength of the microring would be when the laser fluence is not constant over the spot size as is the case of a Gassian beam shape. The fluence profile of a Gaussian beam is dependent on the radial distance from the center of the beamspot and is shown below.

$$\text{F}(\text{r}) = \text{F}_o e^{-2r^2/\text{w}_o^2} \tag{6.2}$$

where F_o is the peak fluence of the beam spot and w_o is the beam spot radius (e^{-2}).

Equation 5.1 can be rearranged so that the resonance wavelength shift is a function of both the applied laser fluence and the length of waveguide affected. The length of waveguide affected can then be made to be infinitesimal so the change in resonance wavelength is also infinitesimal.

$$\frac{d\Delta\lambda}{\lambda_o} = \frac{\Delta n_{\text{eff}}(\text{F}(\text{r}))}{n_g} \cdot \frac{dl}{2\pi\text{R}} \tag{6.3}$$

This equation must now be integrated over the length of waveguide affected to determine the total resonance wavelength shift of the microring. The limits of the

integration can be determined from the illustration in Figure 6.2 (b). The Gaussian beam spot is symmetrical and will affect a circular area of the substrate. For simplicity in this analysis, the waveguide section affected by the laser pulse is assumed to be straight even though it is curved in the microring. This assumption is valid since the width of the beam spot is significantly smaller than the microring radius. The length of waveguide affected will be from -$\mathrm{r_{min}}$ to $+r_{\mathrm{min}}$ in the illustration if the center of the beamspot is assumed to be the origin. The integral can now be carried out with equation 6.1 substituted into equation 6.3 and the resulting resonance shift is found below.

$$\frac{\Delta\lambda}{\lambda_o} = \frac{1}{\pi \mathrm{R n_g}}[\frac{x\mathrm{F}_o \mathrm{w}_o}{2}\sqrt{\frac{\pi}{2}} erf(\frac{\sqrt{2}\mathrm{r_{min}}}{\mathrm{w}_o}) + \mathrm{r_{min}}(\Delta \mathrm{n_{min}} - x\mathrm{F_{min}})] \tag{6.4}$$

where erf is the error function.

The only unknown in the above equation is $\mathrm{r_{min}}$ which can be determined from $\mathrm{F_{min}}$ using equation 6.2 below.

$$\mathrm{F(r_{min})} = \mathrm{F_{min}} = \mathrm{F}_o e^{-2r_{\mathrm{min}}^2/\mathrm{w}_o^2} \tag{6.5}$$

This equation can be rearranged so that it is possible to determine $\mathrm{r_{min}}$.

$$\mathrm{r_{min}} = \frac{\mathrm{w}_o}{\sqrt{2}}(\ln \frac{\mathrm{F}_o}{\mathrm{F_{min}}})^{1/2} \tag{6.6}$$

All of this can now be substituted into equation 6.4 to yield the final equation for the resonance shift of the microring expected from the tophat tuning curve if the beam profile is now Gaussian.

$$\frac{\Delta\lambda}{\lambda_o} = \frac{\mathrm{w}_o}{\pi \mathrm{R n_g}}[\frac{x\mathrm{F}_o}{2}\sqrt{\frac{\pi}{2}} erf((\ln \frac{\mathrm{F}_o}{\mathrm{F_{min}}})^{1/2}) + \frac{1}{\sqrt{2}}(\ln \frac{\mathrm{F}_o}{\mathrm{F_{min}}})^{1/2}(\Delta \mathrm{n_{min}} - x\mathrm{F_{min}})] \tag{6.7}$$

6.5 Experimental 400 nm tuning curve

The microring resonators were first shot with the Gaussian beam spot centered over the left side of the microring's waveguide and then recharacterized before being shot again on the right side. The results of the 400 nm Gaussian tuning experiment are shown in Figure 6.3.

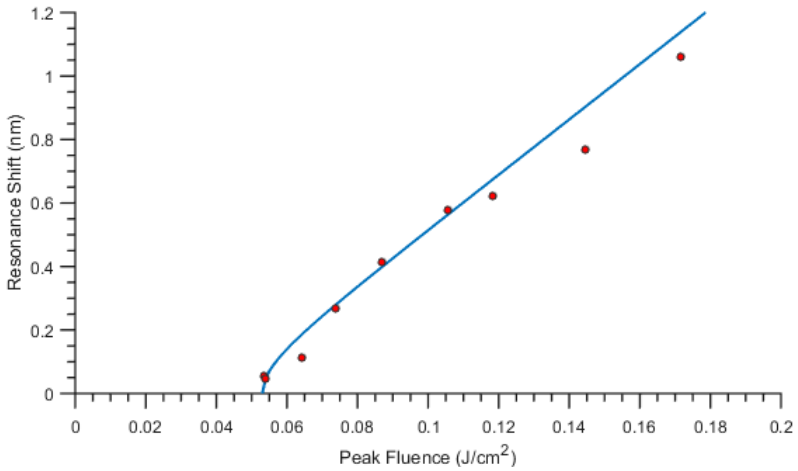

Figure 6.3: Resonance wavelength shift of the 15 µm microring resonators, red circles, as the peak fluence of the 400 nm, 6.2 µm radius Gaussian beam spot is varied. The blue line is the expected resonance wavelength shift based on the 400 nm top-hat beam experiment.

The peak fluence of the laser pulses were varied from 0.053 to 0.18 J/cm^2 and the resonance wavelength shift of the microrings increased as the peak laser fluence was also increased. The increasing trend can be compared to the tuning curve for a tophat beam by using equation 6.7 to generate the expected trend in Figure 6.3. The parameters used to generate the trend were taken from results in the previous chapter except for the threshold fluence which was determined to be slightly lower in this experiment. The beam radius, w_o, was measured to be 6.2 µm, the minimum effective index change to the waveguide, Δn_{min}, was 5.6 x 10^{-2}, the slope of the linear shift, x, was 0.16 per J/cm^2, the original waveguide effective index, n_o, was computed to be 2.3, and the threshold fluence, F_{min}, used was 0.053 J/cm^2.

The blue curve generated in Figure 6.3 for the expected resonance wavelength shifts of the microrings as a function of the peak fluence of the laser pulses follows the trend of the data points obtained experimentally very well. This result helps to prove that the the technique is repeatable and reliable from experiment to experiment even though one was completed with a tophat beam profile and the other with a Gaussian beam profile. This is important because the technique would have to be very reproducible for it to be practical in commercial applications.

6.6 Tuning resolution with 400 nm wavelength

The main goal of this experiment was to determine if the tuning technique would be capable of very fine tuning of silicon photonic circuits. The data points near 0.053 J/cm^2 of Figure 6.3 were the smallest shifts achieved in the experiment. The smallest measured resonance wavelength shift was 0.045 nm, on the order of the full width half maximum (FWHM) of the microring resonance. A sample resonance shift from this spectrum is shown in Figure 6.4.

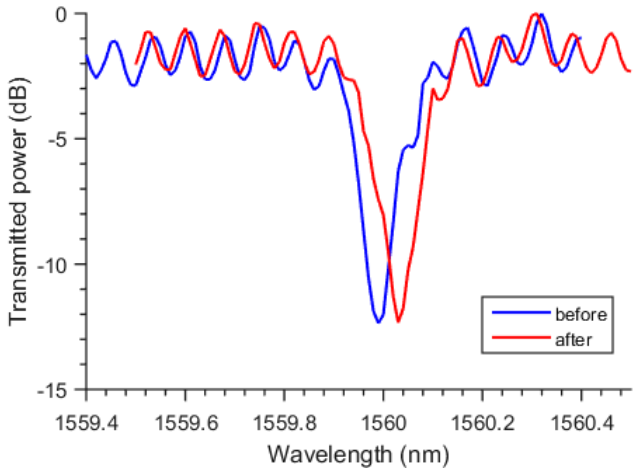

Figure 6.4: Sample resonance shift of the smallest recorded resonance shift for the Gaussian beam shape tuning experiment.

These very small resonance wavelength shifts show that with the appropriate beam shaping, very fine tuning of silicon photonic integrated circuits can be achieved with this femtosecond laser tuning mechanism. Even finer tuning may be possible with a smaller beamspot, but the tuning resolution will ultimately be limited by how precisely a diffraction limited beamspot can be aimed over the top of the waveguide.

6.7 Tuning with 800 nm wavelength

All of the previous experiments in this thesis were conducted with the femtosecond laser at the 400 nm wavelength since light absorption at this wavelength is higher than at 800 nm. However, the literature indicates that it is still possible to produce an amorphous silicon layer at the 800 nm wavelength [62,65]. The optics in the setup in Figure 3.1 were changed from 400 nm to 800 nm so that the 800 nm wavelength

could be tested for tuning silicon microring resonators. The goal of the experiment was to determine if the 800 nm wavelength could also be used to tune silicon photonic circuits and if there were any advantages at the 800 nm wavelength over the 400 nm wavelength. A Gaussian beam shape was used for the experiment since it had already been determined that the Gaussian beam shape allowed for finer tuning at the 400 nm wavelength versus a tophat beam shape.

The results of the 800 nm experiment are shown in Figure 6.5. Aside from the change in femtosecond laser wavelength, the spot size of the 800 nm pulse is also twice as big as the 400 nm wavelength spot size (13.1 μm versus 6.2 μm) since the same pinhole aperture was used to create the quasi-Gaussian beam shape. The 400 nm Gaussian beam shape tuning results are also shown in Figure 6.5 as a comparison.

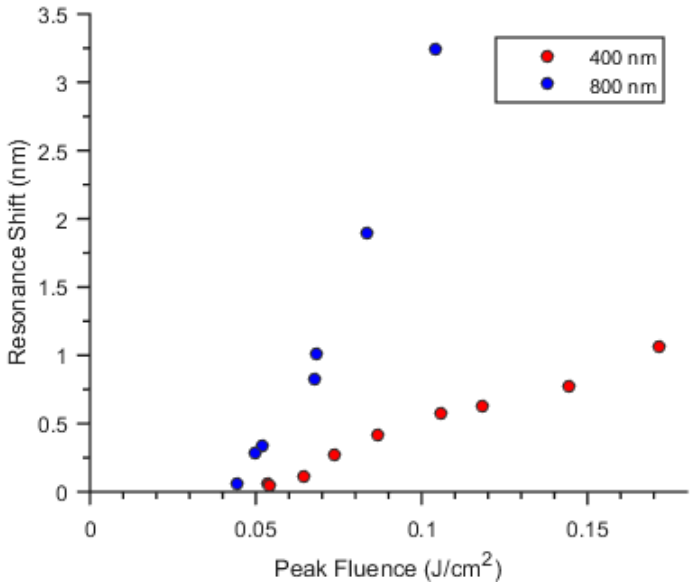

Figure 6.5: Resonance wavelength shifts of the 15 μm radius microrings subjected to irradiation by the 13.1 μm Gaussian beam shape, 800 nm wavelength femtosecond laser pulses, blue circles. The 400 nm wavelength results are included on the same plot for comparison.

Laser pulses with a peak fluence of between 0.044 J/cm^2 and 0.12 J/cm^2 produced measurable resonance shifts in the microring resonators with the resonance wavelength shift of the microrings increasing with increasing laser fluences. The data point at 0.12 J/cm^2 is not included in the plot because it is likely that it shifted the microring resonance greater than one FSR which causes ambiguity in determining the change in

resonance wavelength. A laser shot at a peak fluence 0.165 J/cm^2 induced too much loss in a previously shot microring that the microring resonance could no longer be tracked, while laser shots at peak fluences of 0.304 J/cm^2 and 0.378 J/cm^2 induced too much loss in previously unshot microring resonators for the resonances to be tracked.

Although the relationship between resonance shift and peak fluence is not linear as indicated by equation 6.7, we can approximate the relationship to be linear to compare the relative slopes of 400 nm and 800 nm data. The data point at a fluence of 0.104 J/cm^2 is not included in the linear fit of the data to keep the assumption that the effective beam spot is much smaller than the microring radius in equation 6.7 valid. The linear fit of the 800 nm data yielded a resonance wavelength shift as a function of peak fluence of 45.1 nm/Jcm^{-2} while a fit of the 400 nm data had a slope of 8.4 nm/Jcm^{-2}. Thus the slope of the 800 nm data is about 5.4x that of the 400 nm data in Figure 6.5. Part of this increase in slope is due to the larger spot size used in the 800 nm experiment. Since the same aperture was used to create the Gaussian beam spot at both 400 nm and 800 nm, the spot size of the beam will be twice as large as for the 800 nm beam according to equation 3.2. The resonance wavelength shift is proportional to the size of the beam spot used as shown mathematically by equation 6.7 and therefore, to make a direct comparison of the data, this must be taken into account. Accounting for the different beam spot sizes the relative difference in the slope of the microring resonance shift versus applied laser fluence is about 2.5x greater for the 800 nm data than the 400 nm data.

The above discussion indicates that for the same increase in energy in the laser pulse, there is a larger change in the effective index of the silicon waveguide subjected to an 800 nm wavelength pulse versus a 400 nm wavelength pulse. Part of the reason for this is likely that the thickness of the silicon layer affected by the laser pulses should be greater for the 800 nm pulses than for the 400 nm pulses. The TEM study by Izawa et al. showed that the amorphous silicon layer produced by 800 nm wavelength irradiation was 42 nm thick versus a 17 nm layer produced by 400 nm wavelength irradiation. The thicker layer of material will penetrate closer to the center of the waveguide where the mode will be more sensitive to changes in the refractive index. Part of the reason may also be due to silicon's higher index of refraction at 800 nm

of 3.68 versus at the index of refraction at 400 nm of 5.58 [74]. This difference in the index of refraction translates to different reflection coefficients at both wavelengths and ultimately different fractions of the energy in each pulse that will be absorbed by the silicon. Using Fresnel's reflection formulas, the reflectance at 800 nm is 33% and the reflectance at 400 nm is 48%. The lower reflection at 800 nm means that 1.3x more energy is absorbed at a given fluence for 800 nm irradiation than for 400 nm irradiation. This means that there is more energy available to melt the crystalline silicon and it could account for some of the increase in the slope of the 800 nm data versus the 400 nm data.

Overall using 800 nm wavelength femtosecond pulses may be less ideal for tuning applications than using 400 nm wavelength femtosecond laser pulses based on this analysis. The larger slope of the 800 nm data will make it more susceptible to energy changes from shot to shot than the 400 nm wavelength pulses. However, this may not be important if the energy of the laser pulse is very stable from shot to shot.

6.8 Tuning resolution with 800 nm wavelength

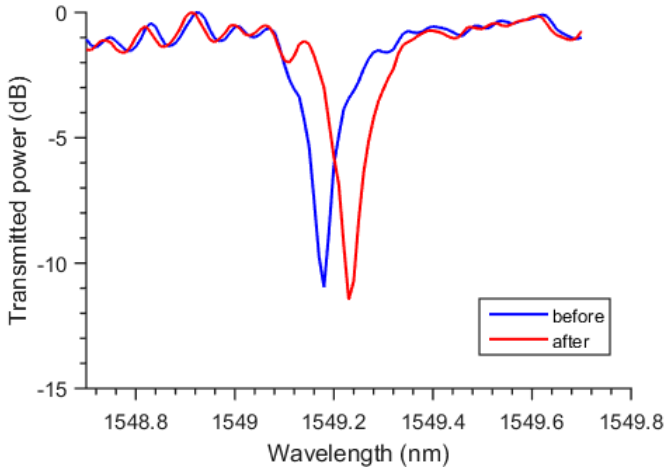

Figure 6.6: Sample resonance shift of the smallest recorded resoance shift for the 800 nm wavelength Gaussian beam shape tuning experiment.

As previously stated, one of the goals of the experiment in this chapter was to see if the technique would be capable of fine tuning of silicon microring resonators and silicon photonic circuits in general. For 800 nm irradiation to be useful, fine tuning

must also be demonstrated at this wavelength. The smallest resonance wavelength shift at this wavelength corresponds to the data point at a peak fluence 0.044 J/cm^2 in Figure 6.5. The resonance shift recorded at that peak fluence was 0.053 nm, on the order of the microring resonance's FWHM. A sample resonance shift from this spectrum is shown in Figure 6.6. Note that the Fabry-Perot induced ripples in the spectrum are surpressed here due to an angled waveguide end facet as a result of a poor cleave at the last step of fabrication. This data point shows that fine tuning of the microring's resonance is also possible with 800 nm wavelength femtosecond laser pulses.

6.9 Waveguide loss of 400 and 800 nm wavelength irradiation

The induced waveguide losses corresponding to the resonance wavelength shifts were also determined using curve fitting as in the previous experiments with a tophat beam. The results for both the 400 and 800 nm data points are in Figure 6.7

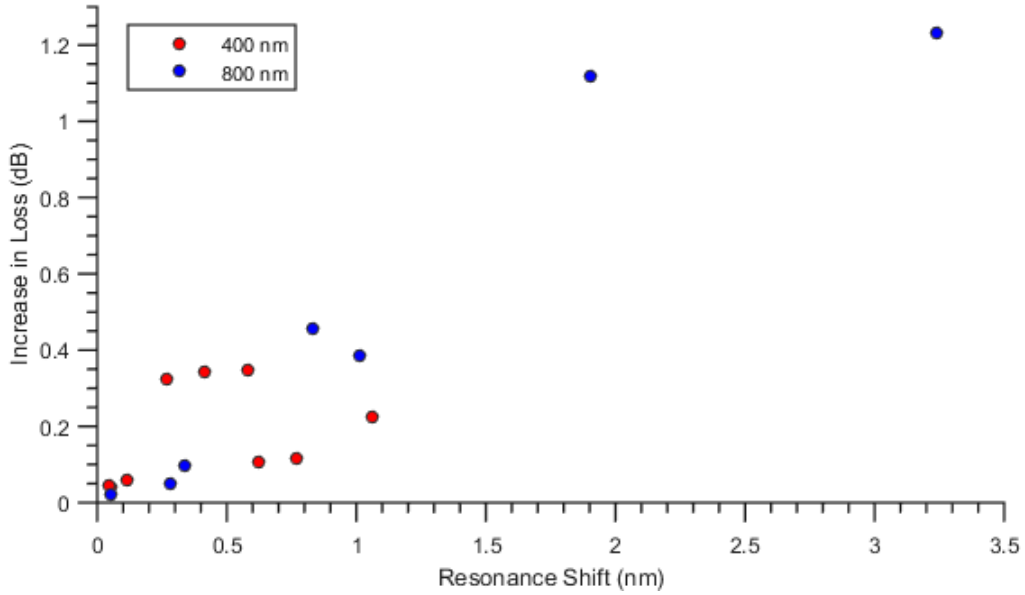

Figure 6.7: Increase in the roundtrip loss of the microring as a functional of the induced resonance shift for both the 400 nm wavelength femtosecond laser pulses and the 800 nm femtosecond laser pulses.

For the 800 nm wavelength data the amount of loss induced in the microring

resonators increases with increasing resonance wavelength shifts. For the 400 nm data, however, the increase in the microring roundtrip loss increases and then decreases. Part of the reason for this trend can again be attributed to backscattering causing a discrepancy in the measured roundtrip loss of the microring from different resonances for the same microring. This effect can artificially increase the measured induced loss in the microring if the backscattering is amplified as discussed for the previous results in the tophat beam experiment in Chapter 5 [37]. However this same effect was not observed for the 800 nm wavelength results as the induced loss increases with the resonance wavelength shift and there is very little variability in the measured roundtrip loss from resonance to resonance in the same spectrum. The physical mechanism for the reduced backscattering at the 800 nm wavelength may be related to the larger penetration depth of 800 nm femtosecond laser pulses compared to the 400 nm femtosecond laser pulses [65]. This would likely create a thicker layer of amorphous silicon which may be more homogenous throughout the silicon waveguide creating less volumetric index inhomogeneities or surface roughness.

Unfortunately when the microring is shifted by 2 nm or more by the 800 nm pulses, the amount of induced loss approaches 1 dB or greater. This amount of loss would likely be unacceptable for some applications. Therefore, for small resonance wavelength shifts of high quality factor microring resonators, 800 nm may be more benefical to use over 400 nm due to the smaller increase in backscattering observed after the shot. For large shifts in any device, 400 nm may be more useful due to the relatively lower induced loss for comparable shifts using the 400 and 800 nm wavelengths (compare shifts of over 3 nm using the 400 nm wavelength from the tophat beam shape experiment in Chapter 5 with less than 0.5 dB increase in loss to shifts here greater than 3 nm with 800 nm Gassian pulses that increase loss by over 1 dB in the microrings).

The benefits of using 400 nm wavelength femtosecond laser pulses versus 800 nm laser pulses will likely depend on the application. In devices where a small increase in backscattering is very detrimental it may be better to use 800 nm wavelength femtosecond laser pulses to perform tuning of the device. In devices where a large shift is required it may be better to use 400 nm wavelength femtosecond laser pulses.

6.10 Determination of the threshold fluence for permanent change

Figure 6.5 plots the resonant wavelength shift as a function of the laser fluence for both the 800 nm and 400 nm femtosecond pulses. For both wavelengths, we observe that the resonant wavelength shift increases with increasing laser fluence with an almost linear relationship. Using this trend as a guide, we can determine the fluence required to create a permanent index change to the Si waveguide at each wavelength. For the 400 nm wavelength, we determined this threshold value to be 0.053 ± 0.007 J/cm^2, which is in agreement with the previously reported value of 0.06 J/cm^2 in [65] as well as previous studies by our group using flat-top beams [37, 86]. The modification mechanism was attributed in [65] to the formation of a $\sim$17 nm thick amorphous silicon layer near the surface. Since amorphous silicon has a higher refractive index than crystalline silicon, the effective index of the microring waveguide increases after the femtosecond laser irradiation, which results in the measured red shifts in the resonant wavelengths of the microring. We also note that for all laser fluences that caused a shift in the resonant wavelengths, there was a visual change in the reflectivity of the crystalline silicon substrate underneath the SiO_2 layer. An optical microscope image of the microring after irradiation at 0.144 J/cm^2 peak fluence is shown in Figure 6.8 (a), from which the spot modified by the laser can be seen on the right side of the ring waveguide. The corresponding resonance spectrum shift is shown in Figure 6.8 (b). This visual evidence corroborates with the hypothesis that there is a change in the reflectivity of the silicon surface due to amorphization.

For the 800 nm wavelength, the fluence required to cause a permanent index change to the crystalline silicon waveguide was determined to be 0.044 ± 0.005 J/cm^2. This value is about a factor of 5 smaller than previously reported values for the modification threshold of crystalline silicon, which are in the range of 0.18-0.27 J/cm^2 [60–62,65,66]. Previously reported threshold values by Bonse et al. (0.26-0.27 J/cm^2) [60–62] and Izawa et al. (0.18-0.21 J/cm^2) [66] were determined by using a Gaussian beam measurement technique where a visual change in the reflectivity at the silicon surface was required to determine the modified spot area. The threshold fluence is determined by taking multiple shots at varying fluences and plotting the relation

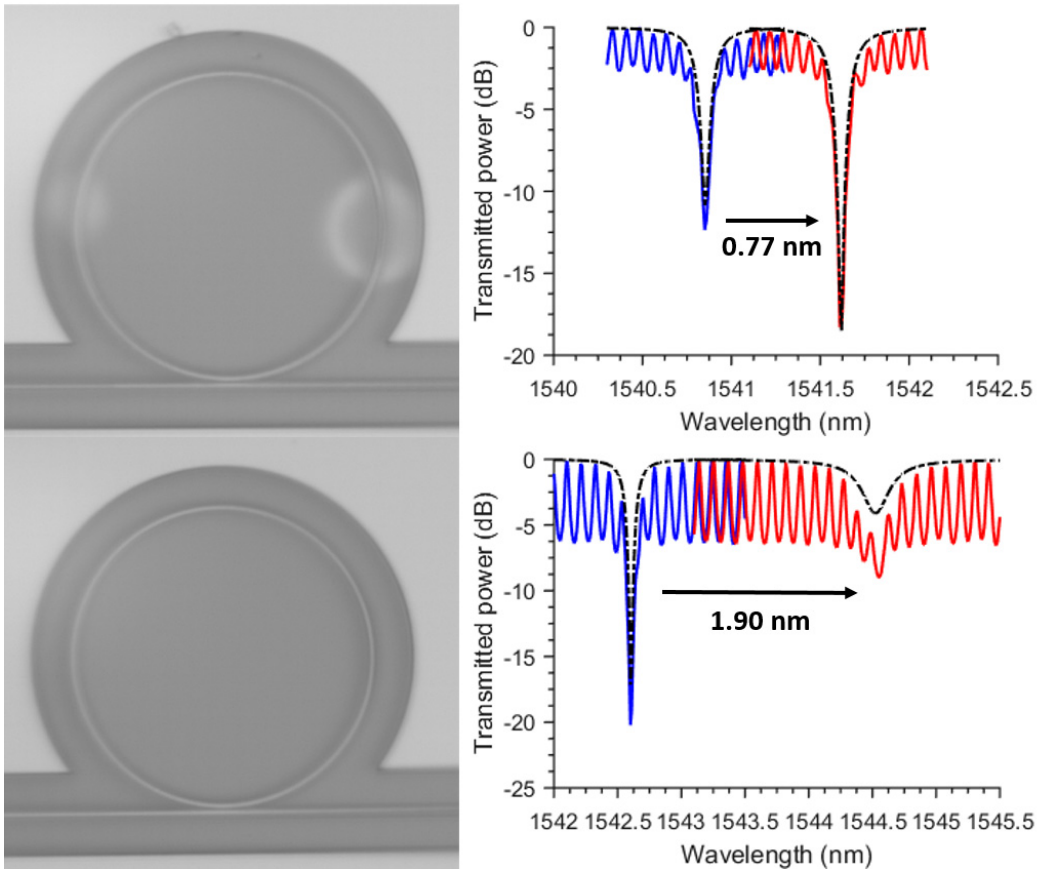

Figure 6.8: (a) Optical microscope picture of a microring resonator that has been subjected to a 400 nm wavelength femtosecond laser pulse on the left and right side. (b) Sample resonance shift after the irradiation of the microring in (a) on the right side corresponding to a peak fluence of 0.144 J/cm^2. The blue line is the microring resonance before the shot and red line is the resonance spectrum after. The black dashed lines are the extracted microring response obtained by curve fitting. (c) Optical microscope picture of a microring resonator that has been subjected to a 800 nm wavelength femtosecond laser pulse on the left and right side. (d) Sample resonance shift after the irradiation of the microring in (c) on the right side corresponding to a peak fluence of 0.083 J/cm^2. The blue line is the microring resonance before the shot and red line is the resonance spectrum after. The black dashed lines are the extracted microring response obtained by curve fitting.

below.

$$D^2 = 2w_o^2(\ln F_o - \ln F_{th}) \tag{6.8}$$

where D is the diameter of the area of colour change, w_o is the beam width, F_o is the peak fluence of the pulse used, and F_{th} is the threshold fluence. By plotting area versus the $\ln F_o$ it is possible to perform a linear fit using equation 6.8 to obtain the threshold fluence, F_{th} where the area of the spot goes to zero.

Our method relies on more accurate measurement of the resonant wavelength shift of the silicon microring and allows us to detect permanent changes that may occur in the silicon waveguide below the threshold for visual change. For example, Figure 6.8 (c) shows an optical microscrope image of the microring after irradiation on the right side by a femtosecond laser pulse at 800 nm wavelength with a peak fluence of 0.083 J/cm^2, which is far below the previously reported modification threshold. The measured resonance spectra before and after irradiation are shown in Figure 6.8 (d). We observe a large shift (1.90 nm) in the microring resonant wavelength even though there is no visible change to the silicon surface below the microring waveguide.

We have also attempted laser shots at 800 nm wavelength with fluences above the threshold for visual change on the microrings. However, due to the large induced loss in the amorphized silicon layer, the microring resonances completely disappeared from the measured spectra so that we could not determine the resonant wavelength shifts for these shots. However, since these shots did result in visible modified spots on the silicon substrate, we could use the same Gaussian beam measurement technique in [60–62,65,66] to estimate the threshold for visual change. For laser shots with peak fluences of 0.304 J/cm^2 and 0.378 J/cm^2, we measured the diameters of the modified spots to be 16.0 μm and 19.3 μm, respectively. By extrapolating these data points to zero area, we obtained an estimate of 0.19 J/cm^2 for the modification threshold of silicon. This value is consistent with the previously reported values in the literature of 0.19 to 0.27 J/cm^2 at 800 nm wavelength [60–62, 65, 66].

The above results indicate that there is a permanent change to silicon induced by the femtosecond laser pulse at fluences far below previously measured thresholds. The exact physical mechanism for the change observed below the amorphization threshold at 800 nm wavelength is unclear and requires additional studies to determine. Nevertheless, it is reasonable to expect that there may be a very minor damage to the crystallinity of the silicon caused by the femtosecond laser pulse. Izawa et al. performed cross-sectional transmission electron microscopy (TEM) of samples irradiated by 800 nm femtosecond pulses at a fluence near 0.20 J/cm^2 and reported finding a pre-amorphization regime of interaction [66]. They found that silicon irradiated on the same spot with 1-5 pulses at these fluences exhibited a colour change, but it was not accompanied by the formation of a distinct amorphous silicon layer at the sur-

face. Only after 6 pulses did they observe an amorphous silicon layer via TEM. Our experiment was performed at much lower fluences so it may be possible that the index change induced in the silicon was too small to be observed as a colour or reflectivity change on the surface. Instead, the index change may occur gradually over the bulk of the silicon waveguide core without the formation of a sharp amorphous interface at the surface that could be visually detected through an optical microscope.

The absence of a thin amorphous silicon layer at the surface implies that the damage to the silicon waveguide was likely to occur at fluences below the melting threshold. Indeed, theoretical calculations of the melting threshold of silicon at the 800 nm wavelength indicate that the onset of melting occurs at higher fluences of 0.14 J/cm^2 [87] to 0.27 J/cm^2 [55] similar to the range of experimentally reported threshold for onset of visible damage [60–62, 65, 66]. By contrast, our measured threshold for index change by 400 nm wavelength pulses was accompanied by a visible change in the reflectivity at the surface, indicating that a sharp interface between crystalline and molten silicon was formed [65]. Thus it may be concluded that the silicon surface reached the melting temperature at the threshold fluence for index change at 400 nm wavelength, whereas its temperature remained below melting at the threshold for 800 nm wavelength. Detailed theoretical calculations of femtosecond ionization and heating of silicon with femtosecond 625 nm laser pulses [87] show significant ionization to electron densities of approximately 10^{21} cm^{-3} in 100 fs and subsequent heating to temperatures of approximately 600 K in 1 ps for incident laser fluences of 0.05 J/cm^2 near our observed index change threshold value. The generation of such a high density of free electrons and the stress from the rapid heating and subsequent rapid cooling of the lattice may induce lattice changes and defects leading to the change in refractive index as observed here. Adding to this argument, an experimental study of the incubation effect in 800 nm femtosecond laser irradiation of crystalline silicon found that the modification threshold was lowered when many shots were used and that it followed the power law $\phi_{mod}(N) = \phi_{mod}(1)N^{\zeta-1}$ [60]. $\phi_{mod}(N)$ is the modification threshold fluence for N pulses and ζ is a material dependent coefficient which was found to be 0.84 for silicon [60]. This shows that some sort of damage is occurring to the silicon below the threshold for visual change on the substrate. Moreover, if we apply this power law to the single shot modification thresholds of between 0.15 - 0.27

J/cm^2, it yields a 1000 shot damage threshold of between 0.05 - 0.09 J/cm^2. This onset of some modification would be consistent with a refractive index change as we observe in the experiment at such low fluences.

6.11 Summary

In this chapter, fine tuning of silicon microring resonators was attempted using Gaussian shaped femtosecond laser pulses at 400 nm and 800 nm wavelength. Very small shifts of about the FWHM of the microring resonators were achieved using both wavelengths which showed that the technique is capable of fine tuning of silicon photonic integrated circuits. Tuning curves were also generated using both wavelengths and it was observed that the 800 nm data had a slope about 2.5x larger than that of the 400 nm data, which may make tuning at 800 nm more sensitive than at 400 nm. The loss data from both experiments indicated that for small resonance wavelength shifts the loss is comparable for both wavelengths but gets larger for the 800 nm wavelength when bigger shifts are required. However it is noted that the 800 nm wavelength did not seem to induce as much backscattering in the microring waveguides as the 400 nm wavelength which may be advantageous for some applications. The threshold fluences for observing a resonance wavelength shift in the microrings were also recorded and compared with previously obtained values in the literature. The 400 nm wavelength threshold is consistent with the literature, but the threshold for the 800 nm wavelength is about 5-6x smaller than previously obtained values in the literature and was below the threshold for a visual change to the substrate.

Chapter 7

Permanent phase correction in advanced silicon PICs

In the previous chapters, femtosecond laser modification of silicon waveguides has been shown to have the potential of tuning silicon photonic integrated devices. In this chapter, tuning of advanced silicon photonic integrated circuits is performed using the femtosecond laser tuning technique.

7.1 Resonance alignment of a second order microring filter

Single microring resonators have simple first order filter responses. However, there are many applications where a more complex filter response is required and these can be created by coupling multiple microrings together. By coupling multiple microrings together higher order filter responses can be created with higher roll off and flat-top passband than first order filters. The resonances of the coupled microrings must be aligned for proper operation of the device [20]. One potential application of the femtosecond laser tuning technique is in correcting fabrication-induced resonance misalignment in high-order silicon microring filters in order to restore their spectral responses. In this section we will use the method to tune and align the resonances of a second-order Vernier microring filter.

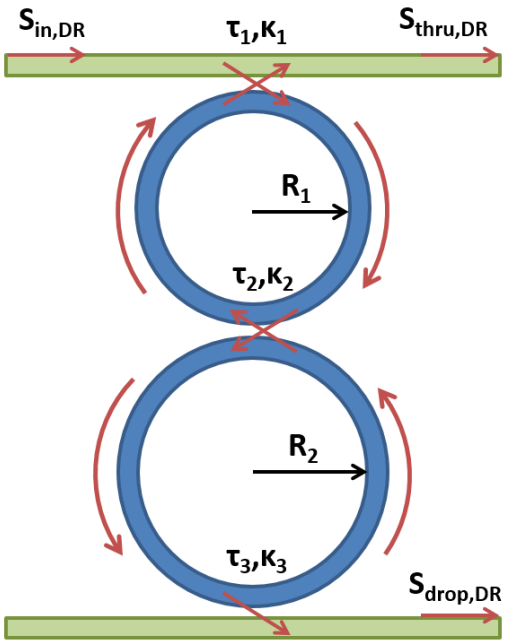

Figure 7.1: Schematic of a second order microring resonator filter. The first microring has radius R_1 and the second has radius R_2. The blue and green sections are the microring and bus waveguides respectively. Red arrows represent the propagation of the electric field through the structure with S_{in} as in the input electric field and S_{thru} and S_{drop} as the output electric fields. $\kappa_{1,2,3}$ and $\tau_{1,2,3}$ are the field coupling and transmission coefficients between the bus waveguides and/or microring waveguides.

7.1.1 Second order microring Vernier filter design

A second order microring filter is shown in Figure 7.1 where two microrings are serially coupled together. The filter looks very similar to an add-drop microring filter with two bus waveguides. The microrings have radii R_1 and R_2 and are coupled together by field transmission and coupling coefficents τ_2 and κ_2. The input bus waveguide is coupled to microring 1 by τ_1 and κ_1 and the drop-port bus waveguide is coupled to microring 2 by τ_3 and κ_3.

By tracing the field through the microrings, the equations for $S_{thru,DR}$ and $S_{drop,DR}$ can be derived analytically below.

$$\frac{S_{thru,DR}}{S_{in,DR}} = \frac{\tau_1 - \tau_2 a_{rt1} e^{-j\phi_{rt1}} - \tau_1\tau_2\tau_3 a_{rt2} e^{-j\phi_{rt2}} + \tau_3 a_{rt1} a_{rt2} e^{-j\phi_{rt1}} e^{-j\phi_{rt2}}}{1 - \tau_1\tau_2 a_{rt1} e^{-j\phi_{rt1}} - \tau_2\tau_3 a_{rt2} e^{-j\phi_{rt2}} + \tau_1\tau_3 a_{rt1} a_{rt2} e^{-j\phi_{rt1}} e^{-j\phi_{rt2}}} \tag{7.1}$$

$$\frac{S_{drop,DR}}{S_{in,DR}} = \frac{-j\kappa_1\kappa_2\kappa_3 a_{rt1}^{1/2} a_{rt2}^{1/2} e^{-j\phi_{rt1}/2} e^{-j\phi_{rt2}/2}}{1 - \tau_1\tau_2 a_{rt1} e^{-j\phi_{rt1}} - \tau_2\tau_3 a_{rt2} e^{-j\phi_{rt2}} + \tau_1\tau_3 a_{rt1} a_{rt2} e^{-j\phi_{rt1}} e^{-j\phi_{rt2}}} \tag{7.2}$$

where $a_{\mathrm{rt1,2}}$ and $\phi_{\mathrm{rt1,2}}$ are the roundtrip loss and phase factors of the microrings respectively.

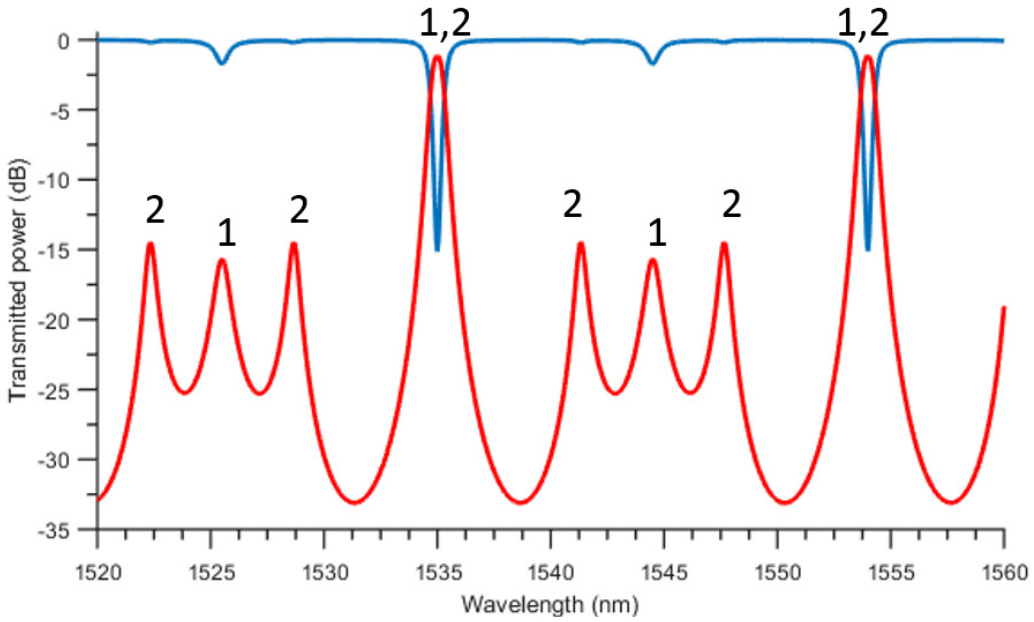

Figure 7.2: The through-port, blue line, and drop-port, red line, power spectrum of a second order silicon microring resonator with a $R_1 = 8$ μm $R_2 = 12$ μm that has values of $\kappa_1 = \kappa_3 = 0.60$ $\kappa_2 = 0.18$ and $a_{\mathrm{rt1}} = a_{\mathrm{rt2}} = 0.98$. The drop port peaks corresponding to reach ring are labelled in the plot.

At the outputs of the second order microring device, the power transmitted at the through port and drop port are represented by $|S_{\mathrm{thru,DR}}|^2$ and $|S_{\mathrm{drop,DR}}|^2$. The power spectrum for both outputs is plotted in Figure 7.2 for a second order silicon microring device designed to have a 3dB bandwidth of 100 GHz. The device consists of two microrings of radii $R_1 = 8$ μm and $R_2 = 12$ μm, with corresponding FSRs of 9.5 nm and 6.33 nm respectively. The microring radii have been carefully chosen to take advantage of the Vernier effect [43,88]. The Vernier effect causes the suppression of microring resnance that do not align so that the FSR of the filter is effectively broadened. In particular, the total FSR of the Vernier filter is given by

$$\Delta\lambda_{\mathrm{FSR,Total}} = m_1\Delta\lambda_{\mathrm{FSR,1}} = m_2\Delta\lambda_{\mathrm{FSR,2}} \tag{7.3}$$

where $m_{1,2}$ are coprime integers and $\Delta\lambda_{\mathrm{FSR,1,2}}$ are the FSRs of microring 1 and microring 2 [88]. Since a microring's FSR is inversely proportional to the microring radius (equation 2.2) this gives the design condition below.

$$\frac{m_2}{m_1} = \frac{R_2}{R_1} \tag{7.4}$$

For this design, the coprime integers 2 and 3 were chosen for m_1 and m_2 which enabled the choice of microring radii $R_1 = 8$ μm and $R_2 = 12$ μm. This gives the microring device a combined FSR of 19 nm.

In addition, the second-order microring filter can be designed to have a wider bandwidth with flatter passband and steeper roll-off than first order microring filters. Another advantage of utilizing the Vernier effect for our tuning experiment is that it is easier to determine which resonances in the spectrum belong to which microring due to the different FSRs of the two microrings. For example in Figure 7.2, the suppressed resonance at 1544.5 nm is from microring 1 while the suppressed resoances at 1541.33 nm and 1547.66 nm are due to microring 2. This allows us to determine which microring should be tuned and by how much.

7.1.2 Experimental demonstration of resonance alignment

To demonstrate the ability of the femtosecond laser tuning technique to permanently correct the resonance mismatch in high-order microring filters, we designed and fabricated a second-order microring filter consisting of two-nonidentical microring resonators with unmatched resonances. An SEM image of the device is shown in Figure 7.3 (a). The two microrings have radii $R_1 = 8$ μm and $R_2 = 12$ μm, giving individual FSR of 9.5 nm and 6.33 nm respectively. When two resonances of the microring are aligned, the FSR of the device will increase to 19 nm due to the Vernier effect with suppressed resonance peaks in between [43, 88]. The field coupling coefficients between the bus waveguides and the microrings (κ_1, κ_3) and between the two microrings (κ_2) were designed to give a flat-top filter response. For a 100 GHz-bandwidth filter the coupling values were determined to be $\kappa_1 = \kappa_3 = 0.60, \kappa_2 = 0.18$, and the corresponding coupling gaps were $g_1 = 170$ nm, $g_2 = 300$ nm, and $g_3 = 200$ nm. (The coupling gap between ring 1 and the input bus waveguide is smaller than between ring 2 and the output bus waveguide because ring 1 has a smaller radius and hence shorter interaction length with the bus waveguide).

The top trace in Figure 7.3 (b) shows the as-fabricated spectral response of the

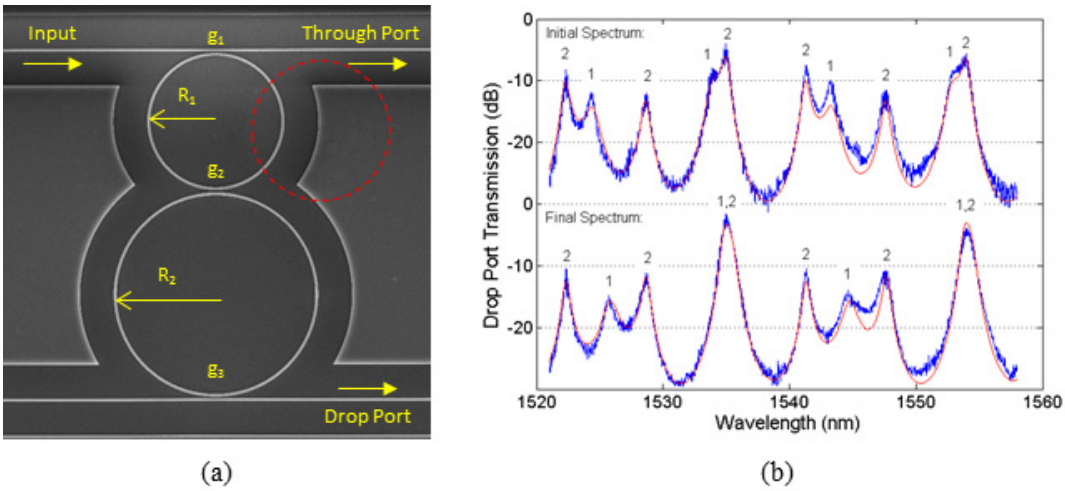

Figure 7.3: (a) SEM of the second-order microring filter. All of the device paremters are labeled in yellow and the location of the irradiation by the single femtosecond laser pulse is outlined in red. (b) Spectral response before and after tuning by a femtosecond laser pulse. The blue curves are the measured spectra and the red curves are the best fits, with the peaks corresponding to ring 1 and 2 labeled.

device with the resonance peaks of each microring labelled. All data was put through a low pass filter to remove the periodic Fabry-Perot response caused by reflections from the waveguide facets. The Fabry-Perot response could not be modelled for this device as was done for the single microring responses because the device is more broadband than single microring resonators. Over small wavelength spreads, the FSR of the Fabry-Perot for modelling can be assumed to be constant. However, this assumption is no longer valid over wide wavelength spreads because of group velocity dispersion in the wavegude effective index. This is complicated even further by small temperature variations in the room that will also affect the observed period of the Fabry-Perot response due to the length of time it takes to measure the wide spectral response of this device. Removing the Fabry-Perot response in this manner has very little effect to the spectral response of this device because the bandwidth of this device is much larger than the FSR of the Fabry-Perot response.

As seen in Figure 7.3 (b) the 1535 nm transmission peak is initially split due to ∼1.1 nm detuning between the resonances of the two microrings as determined by curve fitting using equation 7.2. To align the two resonances, we increased the resonance wavelength of microring 1 by applying a single 400 nm wavelength, femtosecond laser shot at 0.06 J/cm^2 to a section of the ring indicated in Figure 7.3

(a). The laser shot was not centered over the waveguide because a laser shot at the minimum fluence of 0.06 J/cm^2 would have induced too much shift in the microring resonance according to equation 5.1. The only way to decrease the shift induced by the laser pulse was to reduce the length of the waveguide affected, l, by moving the laser spot away from the center of the microring. It was determined that moving the center of the laser spot approximately 4 μm away from the center of the microring waveguide, which corresponded to the edge of the microring trench on the right side, would provide the desired result.

The device spectral response after the laser shot is shown by the bottom trace in Figure 7.3 (b). The two microring resonances at the 1535 nm wavelength are seen to merge to form a second-order filter response with a bandwidth of 112 GHz and an insertion loss of ∼3 dB. Careful modelling of the spectral response (shown by the red curve and obtained by least squares fitting) revealed that microring 1's resonance wavelength was now greater than microring 2's resonance wavelength by ∼0.3 nm, indicating that the resonances of microring 1 were moved by a total of 1.4 nm by the laser shot. Note that at the same fluence of 0.06 J/cm^2, the resonance shift in the 8 μm-radius ring is larger than the value recorded for the 15 μm microring filter in Figure 5.5. This is because a larger fraction of the microring roundtrip length was modified by the laser shot in the smaller ring. We also observed that the adjacent resonance peaks were much more suppressed below the main filter transmission peaks than in the original as-fabricated spectrum. The roundtrip loss for microring 1 before and after the femtosecond laser shot changed only slightly according to our modelling, increasing from 0.77 dB to 0.86 dB, while all other fitting parameters remained the same except for the resonance wavelength of microring 1. Our model showed that the increase in the loss of microring 1 accounts for only a 0.15 dB change in the insertion loss of the device.

7.2 Phase correction in a polarization diversity silicon photonics circuit

As discussed in the introduction, silicon-on-insulator (SOI) is increasingly being embraced as a material platform for photonic integrated circuits (PICs) due to its CMOS

compatibility, relatively low fabrication cost, and high index contrast which leads to small device footprints [13]. However, silicon waveguides and circuits are generally birefringent so that a silicon PIC is typically operated in a single polarization, either the TE or TM mode, to avoid the problem of polarization dependent loss and dispersion. For an input signal which has a random polarization, as is typical from a fiber optic cable, the polarization dependence of a silicon PIC can lead to signal loss and distortion. A solution is to use a polarization diversity scheme wherein the input signal is split into TE and TM components. Each component is then fed into a separate PIC designed to work for that specific polarization [89]. In many silicon PICs, which are designed to operate only in the TE mode, the TM component obtained after the polarization splitting is rotated by 90 degrees before being fed into an identical PIC as the one used for the TE component [90,91]. The device thus consists of two identical circuits, one to process the TE component of the original signal and the other to process the rotated TM component. The outputs of the two circuits are then recombined or fed directly into photodetectors.

One major challenge with the polarization diversity scheme described above is that it is currently not possible to fabricate two identical silicon PICs to have exactly the same response [17, 18]. This is due to small variations in the silicon waveguides dimensions across the wafer, caused either by process changes or slight differences in the silicon layer thickness. Deviations in the waveguides dimensions lead to variations in the waveguide effective index, which results in slightly different responses for phase-sensitive devices such as Mach-Zehnder interferometers and microring resonators. Some interleaving approaches can be used, although with limited yield [92]. For this reason, post-fabrication correction of phase mismatches in silicon PICs will find usefulness in many polarization diversity applications.

In this section we show that the femtosecond laser tuning method can be used to correct for fabrication induced phase mismatch in a polarization diversity silicon PIC with negligible induced loss [86]. The device used for the demonstration is a differential phase shift keying (DPSK) silicon demodulator. We demonstrate that using a single laser shot, it is possible to accurately impart the correct phase change necessary to fully restore the functionality of the DPSK circuit with no noticeable degradation to its polarization dependent loss and total insertion loss performance.

The result demonstrates the applicability and efficacy of the laser tuning method to practical commercial silicon photonic applications.

7.2.1 DPSK Demodulator

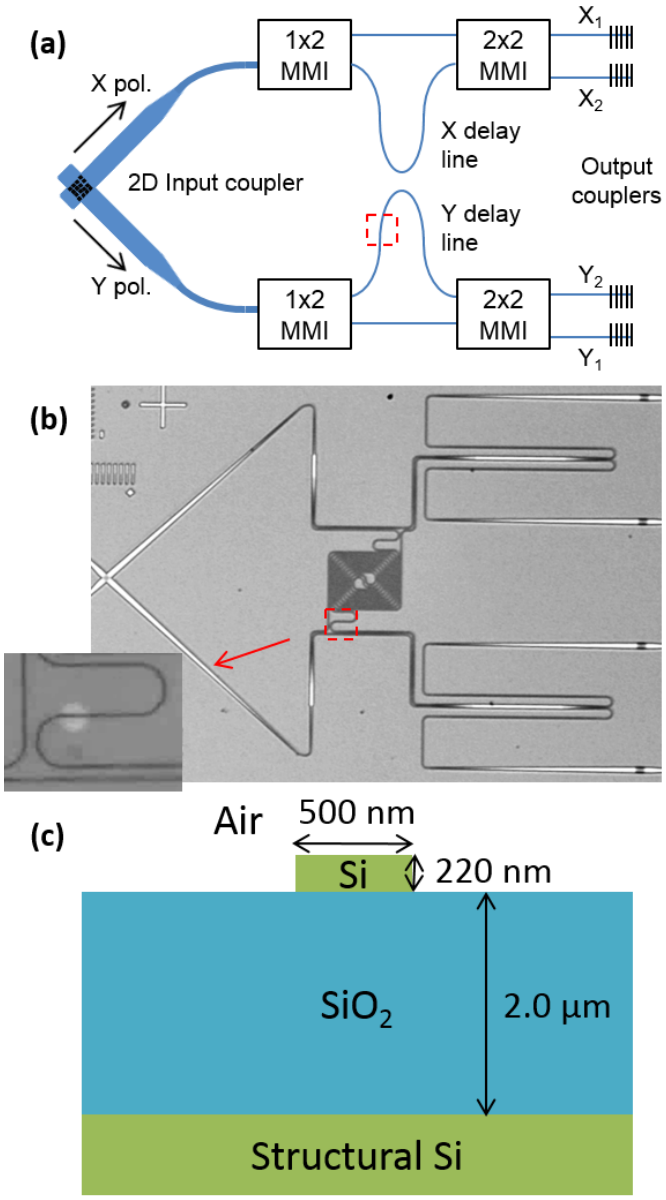

Figure 7.4: (a) Schematic of the polarization diversity DPSK demodulator. The red square indicates the tuning location. (b) Optical micrograph of the DPSK demodulator used in the experiments. The inset shows a close-up view of the delay waveguide section in the red square and the circular area modified by the laser pulse. (c) A cross-sectional diagram of the waveguide designed to operate in the TE mode.

A schematic of the silicon photonic polarization diversity DPSK demodulator is

shown in Figure 7.4 along with an optical micrograph of the fabricated device. The devices were not fabricated in our fab but at a commercial foundry and were given to us on loan from Teraxion. The DPSK circuit uses air-cladded silicon waveguides that are 220 nm thick and 500 nm wide on a 2 μm buffer oxide layer as shown in Figure 7.4 (c). The device is designed to operate in the TE polarization. A 2D surface grating is used to couple input light from a fiber into the device [93]. The 2D grating coupler simplifies the polarization diversity scheme by coupling all polarizations from an optical fiber, at near normal incidence, into the TE mode of the circuit. It accomplishes this by coupling the cross polarizations of an optical fiber (labelled as X and Y) into two separate arms of the circuit, thereby acting as a polarization splitter and eliminating any need for a separate polarization rotator [89]. Each individual arm contains an identical delay line interferometer with a free spectral range of 40 GHz and realized using 1x2 and 2x2 multimode interference (MMI) couplers. The interferometer performs DPSK demodulation of the input signal and sends the in-phase and differential phase-shifted components to the outputs of the 2x2 MMI, which are then coupled out of the chip by standard grating couplers into optical fibers or directly to photodetectors [92].

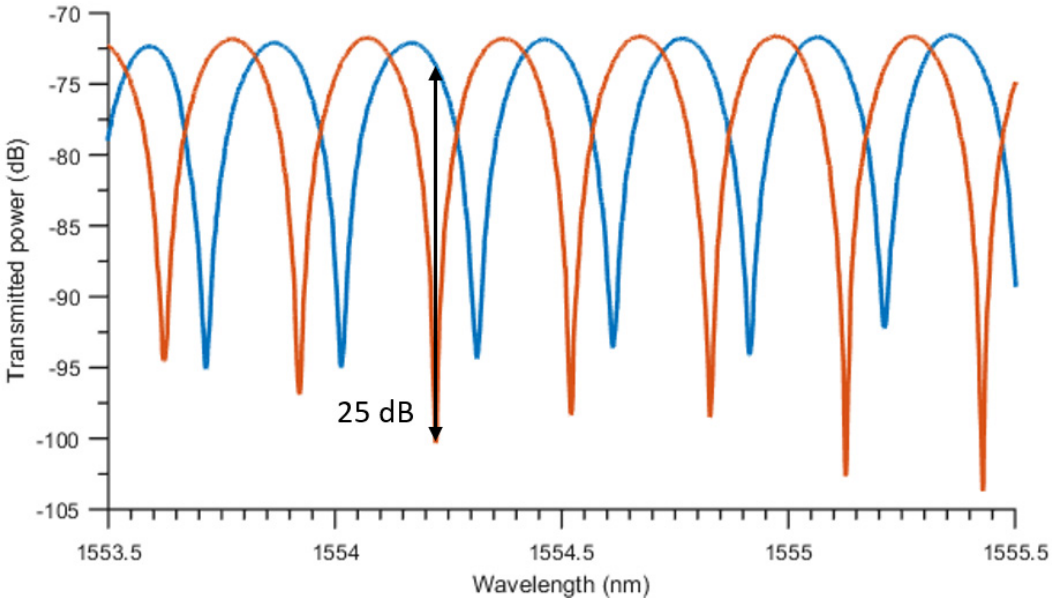

Figure 7.5: Typical spectral response from a DPSK demodulator without any post-fabrication tuning. A mixed polarization was coupled into the input grating coupler and this is the measurement at X_2 (blue line) and Y_2 (red line).

For proper operation of the device, the two interferometers for the separate polarizations must have exactly the same spectral responses. However, due to fabrication imperfections, the spectral responses measured at the outputs X_2 and Y_2 (or X_1 and Y_1) of the as-fabricated devices typically are not identical, but rather show a frequency shift with respect to each other. This is shown for one DPSK demodulator in Figure 7.5 that initially has an 11 GHz frequency shift between the outputs at X_2 and Y_2 (about 0.1 nm in wavelength). At 1554.2 nm, this mismatch causes an output power difference of as much as 25 dB between the two polarizations, rendering the circuit unusable. To recover the polarization diversity operation of the circuit, we apply the fs laser tuning method to correct for the phase mismatch in the delay arms of the two interferometers.

7.2.2 Laser beam characteristics

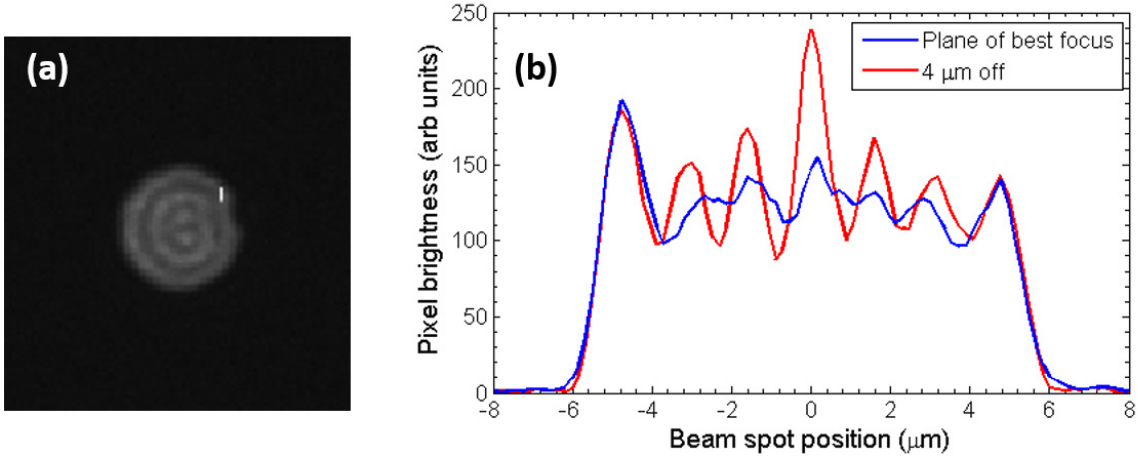

Figure 7.6: (a) Beam spot image of the 5.5 μm radius top-hat beam on the chip. (b) Line-out through the center of the beamspot image at its plane of best focus and 4 μm off.

The setup for the femtosecond laser tuning experiment is shown in Figure 3.1 and 400 nm wavelength pulses were used in this experiment. The top-hat beam profile is used to provide a uniform local fluence profile within the beam spot as shown by the beam spot image in Figure 7.6 (a) and the blue line-out scan in Figure 7.6 (b). However, if the beamspot is not in its best image plane, ripples begin to appear in the beam spot causing hot spots that can be almost double the average input fluence as shown by the red line in Figure 7.6 (b).

7.2.3 Femtosecond laser tuning curve

Because the devices were fabricated on a different SOI substrate with different waveguide dimensions, we first needed to generate a tuning curve to be used in the phase correction of the DPSK demodulator. Several DPSK circuits were used in the tuning experiment and for each circuit, a single fs laser shot at a different laser fluence was applied to the delay arm of either interferometer. The position of the laser shot is located in the area indicated by the red dashed line in Figure 7.4 (b) and the inset shows an optical picture of the affected waveguide section after the illumination. The laser shots were always applied on a previously unmodified section of the waveguide in the red dashed square in Figure 7.4 (b) and all measurements were taken using a mixed polarization optical signal incident on the 2D grating coupler. Figure 7.7 shows the wavelength shift of the transmission minima of the modified interferometer as a function of the applied laser fluence. Error bars are one standard deviation of the measured spectral shifts of transmission minima between 1554 nm and 1556 nm. From the plot it is seen that between a laser fluence of about 0.05 J/cm^2 and 0.10 J/cm^2 there is an approximately linear dependence of the shift in the wavelength of the transmission minima with the applied laser fluence. In this range, the wavelength shifts correspond to changes of approximately (0.3 - 3) x 10^{-2} in the effective index on the affected waveguide, consistent with previous results [37]. At higher laser fluences, the amount of wavelength shift begins to decrease and eventually becomes negative. We attribute positive wavelength shifts in the interference minima to an increase in the effective index of the waveguide section affected by the laser pulse. This is caused by the formation of a thin layer of amorphous silicon ($\sim$15 nm) on the surface of the crystalline silicon waveguide [65]. Similarly, negative wavelength shifts of the minima correspond to decreases in the effective index of the waveguide. This is likely due to the ablation of a thin layer of silicon from the waveguide surface which results in a decrease in the height of the affected waveguide [62].

Experiments on silicon microring resonators in the previous chapter showed that the effective index of the waveguide increases approximately linearly with the laser fluence before abruptly becoming negative at the ablation threshold of $\sim$0.20 J/cm^2 [37]. The tuning curve in Figure 7.7 shows the same approximately linear region

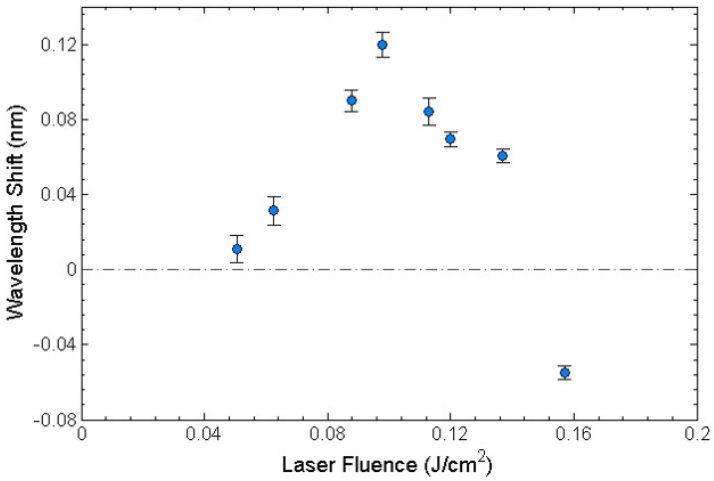

Figure 7.7: Wavelength shifts of the transmission minima of the DPSK interferometers as a function of the applied laser fluence.

for laser fluences between 0.05 J/cm^2 and 0.10 J/cm^2, but the behavior at higher fluences is different from what we previously observed. Here, above 0.10 J/cm^2 the effective index starts to decrease gradually before becoming negative at about 0.16 J/cm^2, which is lower than the ablation threshold observed in [37]. We attribute this discrepancy to hot spots in the top-hat laser beam profile when it is out of focus, as shown by the red line-out scan in Figure 7.6. In the tuning experiment, we had to focus the laser beam on the silicon substrate surface at the bottom of the 2 μm buffer oxide layer instead of the waveguide surface, causing the beam spot to be out of focus by about 3-4 μm in free space. The hot spots in the beam profile might have induced a mixture of amorphized and ablated silicon regions near the waveguide surface, causing the gradual decreasing trend in the effective index between 0.10 J/cm^2 and 0.15 J/cm^2, instead of a more abrupt change due to ablation as previously observed for silicon microrings [37]. Besides the effects of the hot spots, the discrepancies between the tuning curve obtained for this device and the one previously obtained for microring resonators [37] may also be due to the different waveguide dimensions and operating polarizations for each experiment.

For post-fabrication tuning applications, the linear region between about 0.05 J/cm^2 and 0.10 J/cm^2 provides a reliable, repeatable and calibrated range of fluences for modifying the waveguide effective index. If the required wavelength shift for a

DPSK is larger than the maximum wavelength shift of 0.12 nm achieved with a single pulse, then multiple pulses applied to unmodified sections of waveguide may be used on the delay line.

7.2.4 Demonstration of phase correction in a DPSK demodulator

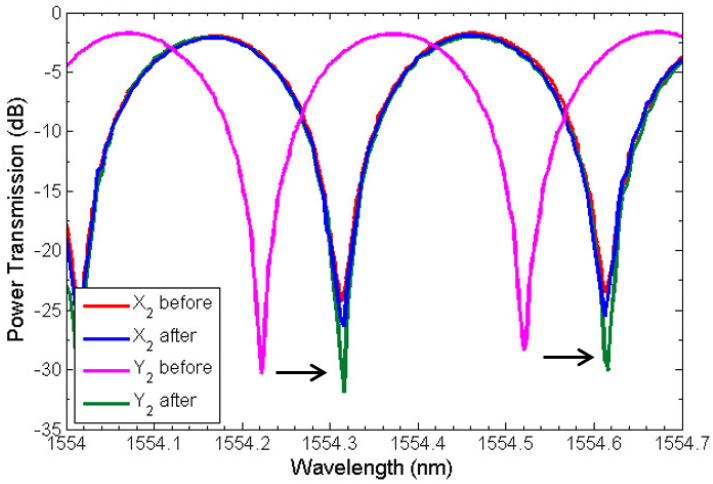

Figure 7.8: Spectral response of an initially detuned DPSK demodulator before tuning (red and pink lines) and after tuning (blue and green). A single 400nm laser pulse at 0.088 J/cm^2 was used to bring the spectral response at the Y_2 port into alignment with the X_2 port.

To demonstrate the ability of the fs laser tuning technique for phase correction in the polarization diversity DPSK circuits, a single pulse with a fluence of 0.088 J/cm^2 is applied to the delay arm of the Y-polarization interferometer to correct for the 11 GHz mismatch in the spectral responses of the two interferometers. The responses of the device before and after the laser shot are shown in Figure 7.8, where the two spectral responses are now well aligned. The measured polarization dependent frequency shift after tuning is smaller than 0.5 GHz (<4 pm). Apart from a frequency shift in the spectral response of the interferometer, the overall response of the DPSK circuit is unaltered by the laser pulse, with the extinction ratio of the interferometers remaining as high as before the shot and no noticeable change in the free-spectral-range. The polarization diversity operation of the DPSK demodulator is thus completely restored with virtually no performance degradation. The induced insertion loss of

the device is also small and is not noticeable within the fiber coupling uncertainty in the experiment. The result demonstrates the effectiveness of the fs laser tuning method in providing fast and permanent correction of phase mismatch in the device.

7.2.5 Tuning DPSK demodulators with a cladding

Preliminary experiments were also performed using femtosecond laser pulses to tune a DPSK demodulator covered with 200 nm of SiO_2 and 800 nm of SiN. For this device with a thick cladding layer, a fluence of 0.28 J/cm^2 was required to shift the spectral response of the interferometer by 0.076 nm. This laser fluence is much higher than that required to tune uncladded silicon circuits because of the absorption of the 400 nm fs laser pulse in the cladding layer. The mechanism for the change in the spectrum was likely different than for the unclad DPSK demodulators due to this absorption in the cladding layer. Nevertheless, the femtosecond laser tuning method can be used for post-fabrication phase correction even when the device is cladded (as long as the cladding layer is transparent), as has been demonstrated for cladded silicon microring resonators in a previous chapter [38].

7.3 Summary

In summary we have demonstrated applications of the femtosecond laser tuning method for post-fabrication phase correction of silicon photonic circuits. The method was used to successfully restore the polarization diversity operation of a silicon DPSK demodulator and correct the resonance mismatch of a second order microring filter. The femtosecond laser tuning method has been previously used to correct tune the resonance wavelengths of single silicon microring resonators [37]. The work reported in this chapter extends the applicability of the method to more advanced silicon PICs and shows that the method can be an effective tool in restoring the operation of polarization diversity circuits and high order microring filters.

The Vernier filter tuning was published in Optics Express in 2013 [37] and presented at CLEO:PR in 2013 [85]. The tuning of the polarization diversity circuit was published in Photonics Technology Letters in 2015 [86] and presented at FiO in 2014 [94].

Chapter 8

Investigation of negative coupling and coupling phase dispersion in a silicon quadrupole micro-racetrack resonator

One of the most advanced applications of microring resonators is the realization of a class of advanced filters called pseudo-elliptic optical filters. This type of filters require a microring configuration arranged in a 2D coupling configuration with negative coupling coefficients between some of the microrings. To date there has been no experimental work that conclusively demonstrates negative coupling in these devices, mainly due to resonance mismatch and fabrication errors [95]. This chapter reports our attempt to realize a fourth-order pseudo-elliptic filter using a silicon coupled micro-racetrack configuration with negative coupling. Our initial aim was to apply the femtosecond laser tuning method to correct for fabrication induced resonance mismatch in the micro-racetrack resonators in order to experimentally observe negative coupling effects in the proposed device. However, the fabricated device exhibited a good filter response without requiring post-fabrication tuning. Although there was some small resonance mismatch in the device, we were able to provide conclusive evidence of negative coupling and investigate the effects of coupling phase dispersion for the first time [96].

8.1 Negative coupling in photonic devices

In integrated photonic circuits, power transfer between two adjacent waveguides is typically accomplished by evanescent field coupling. For short coupling lengths the field coupling coefficient between the two waveguides, as defined in the conventional coupled mode theory [97], is positive. For such a coupler, the coupled electric and magnetic fields have a $\pi/2$ phase lag with respect to the uncoupled fields. All integrated photonic circuits, including coupled optical microring filters [45, 98], are typically designed using positive coupling elements.

An emerging application that requires negative field coupling is the realization of two-dimensionally (2D) coupled microring resonators for synthesizing the spectral responses of a class of optical filters known as pseudo-elliptic filters [99, 100]. These types of filters are characterized by transfer functions with transmission nulls in the stop band, resulting in frequency responses with very sharp stop band transitions and high frequency discrimination. It is well known that conventional microring filters based on the serial coupling configuration (also known as CROW filters) have transfer functions containing only poles and no transmission zeros. These filters have slow stop band transitions and poor frequency discrimination since the spectral response never reaches perfect extinction in the stop band. By contrast, in a 2D microring coupling topology, light follows multiple paths through the device which can interfere destructively with each other at the output to produce transmission nulls at certain frequencies. The use of 2D resonator coupling topologies can greatly expand our ability to engineer the spectral responses of optical devices [99, 100]. However, a major barrier to the practical implementation of 2D coupled microring filters is that to realize transmission nulls, the topology requires negative coupling elements between adjacent microrings, which are difficult to realize in integrated optics.

In a directional coupler with negative coupling, the coupled fields acquire a $\pi/2$ phase lead with respect to the uncoupled fields. In a 2D microring coupling topology, the fields in the resonators have a fixed phase relationship with each other, making it possible to engineer the relative phases of the coupled fields so that they acquire a $\pi/2$ phase lead with respect to the uncoupled fields, thereby resulting in an effective negative coupling. In fact, in general it is possible to engineer the relative phases of

the fields of the coupled resonators to obtain an effective complex coupling coefficient $|\kappa|e^{j\delta}$, where δ is the coupling phase. This technique has been employed to realize negative coupling in a quadrupole microring resonator by shearing the topology by 1/8 of a wavelength [100]. An experimental demonstration of the structure has also been attempted in [95] but due to fabrication errors and other experimental uncertainties, the effect of negative coupling was not clearly evidenced in the device spectral response, so that ambiguity remains as to whether negative coupling was achieved in the system.

In this chapter, we designed and fabricated a coupled micro-racetrack device which allows us to experimentally investigated the effects of frequency dispersion of the coupling phase on the spectral response of a quadrupole resonator. Clear evidence of complex and negative couplings is observed as the coupling phase changes from 0 to π. The quadrupole resonator used consists of four coupled micro-racetrack resonators in which the positions of the coupling junctions can be adjusted to achieve a wide range of coupling phases in the system. In order to experimentally observe the effect of the coupling phase, we designed the quadrupole to have the spectral response of a 4th-order pseudo-elliptic filter and investigated how the transmission null response of the device varies with frequency. A crucial advantage of the proposed racetrack coupling topology over the sheared microrings in [95] is that it enables a wide range of coupling phase values to be realized so that the effects of frequency dispersion of the coupling phase on the device response could be experimentally observed. Measurements of the fabricated quadrupole resonator on silicon-on-insulator (SOI) showed that the stop band transition of the spectral response became increasingly steepened as the coupling phase approaches π, thereby providing for the first time unambiguous evidence of the effect of negative coupling on the device response.

8.2 Device design

The quadrupole resonator used in the experiment consists of four micro-racetracks arranged in the coupling configuration shown in Figure 8.1. Racetracks 1 and 4 are also coupled to an input and an output bus waveguide, respectively, with input signal s_i applied to the input port and transmitted signals s_t and s_d measured at the through

port and drop port, respectively. The field coupling coefficient between microrings i and j is denoted by $\kappa_{i,j}$. The coupling coefficients to the input and output bus waveguides are assumed to be equal and denoted by κ_o.

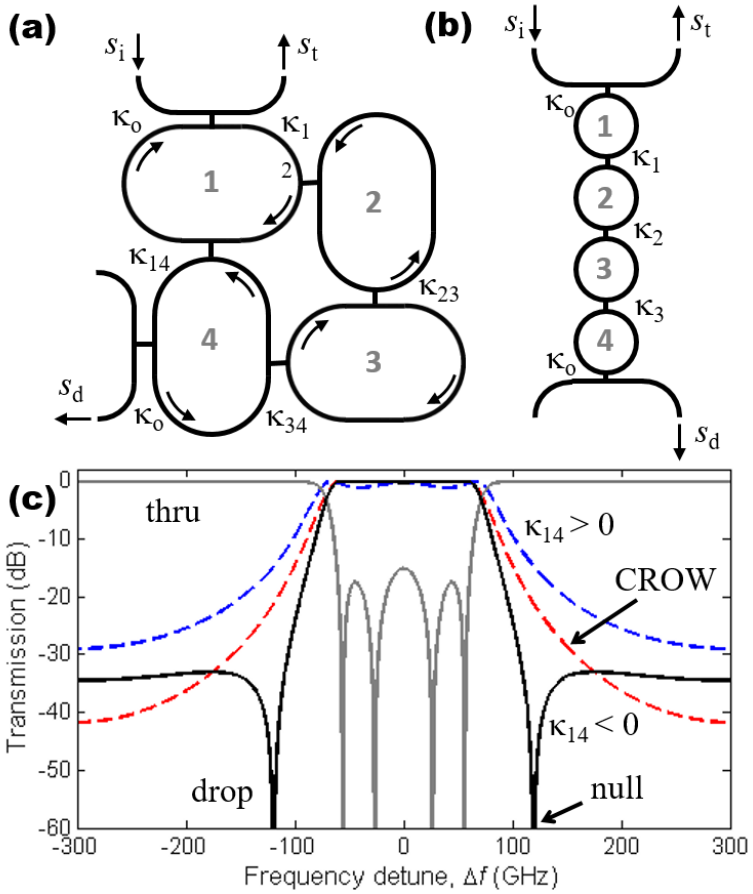

Figure 8.1: (a) Schematic of a quadrupole micro-racetrack resonator. (b) Schematic of a 4^{th} order CROW filter. (c) Target spectral responses of the quadrupole pseudo-elliptic filter (black and grey solid lines). The drop port response of the quadrupole filter with positive κ_{14} value (blue dashed line) and a 4th-order CROW filter (red dashed line) are also plotted for comparison.

The transfer function at the drop port of the quadrupole resonator has the general form [101],

$$H(z) = \frac{K(z - z_1)(z - z_1^*)}{(z - p_1)(z - p_1^*)(z - p_2)(z - p_2^*)} \tag{8.1}$$

where K is a constant, $z = e^{-j\phi}$ is the roundtrip delay variable, ϕ is the roundtrip phase of the racetracks, and p_i and z_i are the poles and zeros, respectively. The above transfer function can be used to realize the spectral response of a pseudo-

elliptic filter with equiripples in both the pass band and stop band [4]. Using the microring filter design method in [101], we designed the quadrupole to have a pseudo-elliptic response with 0.1 dB ripple in the pass band, a 3 dB bandwidth of 150 GHz and a free spectral range (FSR) of 600 GHz. The resulting device transfer function has four poles located at $\{p_1, p_1^*\} = 1.440 \pm j0.494$ and $\{p_2, p_2^*\} = 0.875 \pm j0.741$, and two transmission zeros that are placed at $\pm$120 GHz on both sides of the pass band to obtain a stop band rejection of over -30 dB. The coupling values obtained for the racetracks in the quadrupole are $\kappa_o = 0.82$, $\kappa_{12} = \kappa_{34} = 0.477$, $\kappa_{23} = 0.454$, and κ_{14} = -0.10. The negative coupling value of κ_{14} results from the placement of the two transmission zeros on the unit circle in the z-plane (or equivalently, the $j\omega$-axis in the complex frequency s-plane) in order to achieve sharp transmission nulls.

Figure 8.1 (c) shows the spectral responses at the drop port (black line) and through port (grey line) of the designed quadrupole filter. To show the effect of the negative coupling coefficient κ_{14} on the device response, we also plotted the spectral response at the drop port of the same device but with positive value for κ_{14} (κ_{14} = 0.10, blue dashed line). It is apparent that the transmission nulls responsible for the sharp stop band transitions of the pseudo-elliptic filter disappear when the phase of κ_{14} changes from π to 0. For comparison, we also show in Figure 8.1 (c) (red dashed line) the drop port response of a 4^{th}-order CROW filter (schematic in Figure 8.1 (b)) designed to have the same bandwidth and pass band ripple as the pseudo-elliptic filter. It is evident that the CROW filter has a much slower stop band transition than the 2D quadrupole resonator.

To realize the negative coupling element κ_{14} in the quadrupole system we adjust the positions of the coupling junctions of the racetracks to vary the relative phases of the coupled fields in the resonators. In the design shown in Figure 8.2, the coupling junctions κ_{14} and κ_{23} are located at the midpoints of the straight waveguide sections of racetracks 1 and 3, but the positions of the coupling junctions κ_{12} and κ_{34} are deviated from the midpoints of the straight sections of racetracks 2 and 4 by an amount $\Delta L = (L_2\text{-}L_1)/2$. To obtain an exact relation between the offset ΔL and the phases of the coupling elements, we transform the racetrack quadrupole into an equivalent coupled waveguide array [102]. This is done by "cutting" the micro-racetracks at the positions indicated by the red lines in Figure 8.2 (a), and unfolding

them into straight waveguides while keeping track of the positions of the coupling junctions. The resulting straight waveguide array is shown in Figure 8.2 (b), where coupling between two waveguides is indicated by the line connecting them. The lines corresponding to κ_{12} and κ_{34} are skewed due to the unequal racetrack lengths caused by the coupling junction offsets.

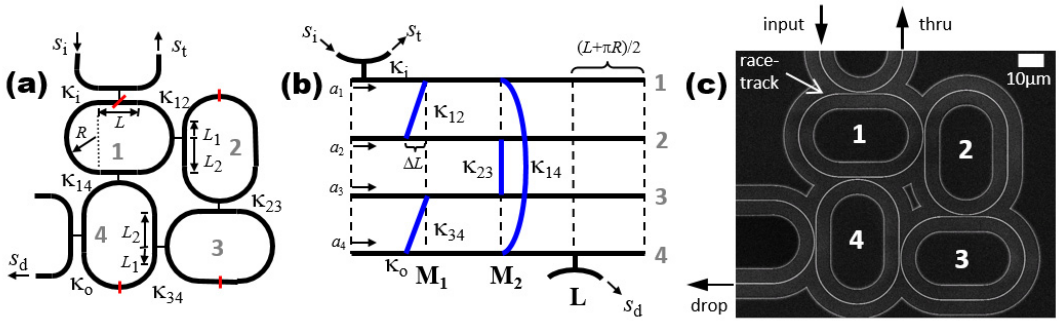

Figure 8.2: (a) Implementation of the quadrupole pseudo-elliptic filter using racetrack resonators. The red lines indicate the position where each racetrack is cut and unfolded to obtain the equivalent coupled waveguide array in (b). (c) Scanning electron microscope image of the fabricated quadrupole micro-racetrack resonator in silicon.

The spectral response of the quadrupole resonator system is obtained by applying the transmission matrix method to the coupled waveguide array. Denoting $\boldsymbol{a} = [a_1, a_2, a_3, a_4]^{\mathrm{T}}$ as the array of fields in the racetrack waveguides, we trace the transmitted fields through the coupled waveguide system to obtain the following equation for $\boldsymbol{a}$ in terms of the roundtrip delay variable z:

$$(\mathbf{I} - z\mathbf{L}\mathbf{M_2}\mathbf{M_1}\boldsymbol{a}) = \boldsymbol{s} \tag{8.2}$$

In the above equation $\mathbf{I}$ is the 4x4 identity matrix and $\mathbf{L} = [\tau_o, 1, 1, \tau_o]$, where $\tau_o = (1 - \kappa_o)^{1/2}$, is the matrix representing coupling to the input and output waveguides. The array $\boldsymbol{s} = [-j\kappa_o s_i, 0, 0, 0]^{\mathrm{T}}$ accounts for the input excitations of the resonators and $\mathbf{M_1}$ and $\mathbf{M_2}$ are the waveguide coupling matrices given by

$$\mathbf{M_1} = \begin{bmatrix} \tau_{12} & -j\kappa_{12}e^{j\delta} & 0 & 0 \\ -j\kappa_{12}e^{-j\delta} & \tau_{12} & 0 & 0 \\ 0 & 0 & \tau_{34} & -j\kappa_{34}e^{j\delta} \\ 0 & 0 & -j\kappa_{34}e^{-j\delta} & \tau_{34} \end{bmatrix} \tag{8.3}$$

$$\mathbf{M_2} = \begin{bmatrix} \tau_{14} & 0 & 0 & -j\kappa_{14} \\ 0 & \tau_{23} & -j\kappa_{23} & 0 \\ 0 & -j\kappa_{23} & \tau_{23} & 0 \\ -j\kappa_{14} & 0 & 0 & \tau_{14} \end{bmatrix} \tag{8.4}$$

where $\tau_{i,j} = (1 - \kappa_{i,j}^2)^{1/2}$. In the matrix $\mathbf{M_1}$ the phase δ associated with coupling elements κ_{12} and κ_{34} is $\delta = n_r(2\pi/\lambda)\Delta L$, where n_r is the effective index of the racetrack waveguides. Thus the effect of offsetting the coupling junctions κ_{12} and κ_{34} by ΔL is to impart a phase shift δ to these coupling elements, effectively making them complex. These coupling phases are relative to the phases of other coupling elements in the quadrupole and are not unique, since it is always possible to apply a similarity transformation to equation 8.2 to obtain new coupling matrices. For example, by applying the similarity transform $\mathbf{T} = \mathrm{diag}[e^{-j\delta}, 1, 1, e^{j\delta}]$ to equation 8.2, we obtain $(\mathbf{I} - z\mathbf{L}\mathbf{M_2'}\mathbf{M_1'}\boldsymbol{a}) = \boldsymbol{s}$, where $\mathbf{M_1'} = \mathbf{T}\mathbf{M_1}\mathbf{T^H}$ is the matrix $\mathbf{M}_1$ in equation 8.3 but with zero coupling phase ($\delta = 0$) for κ_{12} and κ_{34}, and the new matrix $\mathbf{M_2'}$ is given by

$$\mathbf{M_2'} = \mathbf{T}\mathbf{M_2}\mathbf{T^H} \begin{bmatrix} \tau_{14} & 0 & 0 & -j\kappa_{14}e^{j2\delta} \\ 0 & \tau_{23} & -j\kappa_{23} & 0 \\ 0 & -j\kappa_{23} & \tau_{23} & 0 \\ -j\kappa_{14}e^{-j2\delta} & 0 & 0 & \tau_{14} \end{bmatrix} \tag{8.5}$$

Note that the above transformation does not alter the spectral response of the quadrupole since it preserves both the poles (or eigen-frequencies) and zeros of the system. In the new coupling matrix $\mathbf{M_2'}$, the coupling element κ_{14} now acquires a phase of 2δ. For κ_{14} to be negative, we require that at the center resonance wavelength λ_o of the quadrupole,

$$\delta = n_r \frac{2\pi}{\lambda_o} \Delta L = 2m\pi + \frac{\pi}{2} \tag{8.6}$$

where m is an integer. From equation 8.6 we obtain $\Delta L = (m+1/4)(\lambda_o/n_r)$ as the offset length which will result in an effective negative value for the coupling element κ_{14} in the quadrupole.

8.3 Device fabrication and experimental results

We implemented the quadupole filter design on an SOI substrate with a 340 nm-thick Si layer and a 1 μm-thick SiO2 buffer layer. The waveguide width was 300 nm and

the device was designed to operate in the TM mode. The racetracks had a bending radius R = 12 μm and straight sections of length L = 12 μm. The input and output bus coupling value ($\kappa_o = 0.82$) was achieved using an input/output coupling gap of 200 nm and a coupling length of 1 μm. The coupling gaps between racetracks were designed to be $g_{12} = g_{34} = 240$ nm ($\kappa_{12} = \kappa_{34} = 0.477$), $g_{23} = 250$ nm ($\kappa_{23} = 0.454$), and $g_{14} = 450$nm ($\kappa_{14} = 0.10$). To realize an effective negative coupling value for κ_{14}, we set the coupling junction offset $\Delta L = 4.9$ μm, which corresponds to m = 7 at the center wavelength $\lambda_o = 1.55$ μm in (6). We intentionally chose a fairly long ΔL value so that the phase 2δ varies from 0 to 2π over the 1.5-1.6 μm wavelength range, thereby enabling us to observe the effect of coupling phase dispersion on the spectral response of the quadrupole over this wavelength range. The device was fabricated using electron beam lithography and reactive ion etching as discussed in detail in section 2.3. Figure 8.2 shows a scanning electron microscope (SEM) image of the fabricated device, which was left air-cladded. The chip was cleaved to expose the input and output waveguide facets for butt-coupling to lensed fibers.

Figure 8.3 (a-bottom panel) shows the measured spectral responses at the drop port (red line) and through port (blue line) of the quadrupole over the C-band. The measurement data has been filtered using a minimum phase technique to remove the Fabry-Perot ripples in the spectral responses caused by reflections from the chip end facets [103]. To verify that the quadrupole behaves as designed, we performed curve fitting of the measured spectral response using the coupled waveguide model given by equation 8.2. The best curve fits of the drop port and through port responses over the C-band are shown in Figs. 3(a) and (b) (green and black dashed lines), from which excellent agreement between the model and the measured spectral responses can be seen over the broad wavelength range of study. The best curve fits were obtained by setting the coupling coefficients to be 17% larger than designed values to account for the smaller coupling gaps (about 20%) of the fabricated device due to etching bias. To account for loss in the resonators we set the roundtrip amplitude attenuation coefficient of each racetrack to be 0.97, which is similar to the loss value in silicon microring devices fabricated using the same process [37]. The model also indicated that the resonance frequencies of racetracks 2, 3 and 4 were slightly detuned from the first racetrack by Δf_2 = -10 GHz, Δf_3 = 35 GHz, and Δf_4 = 15 GHz, respectively.

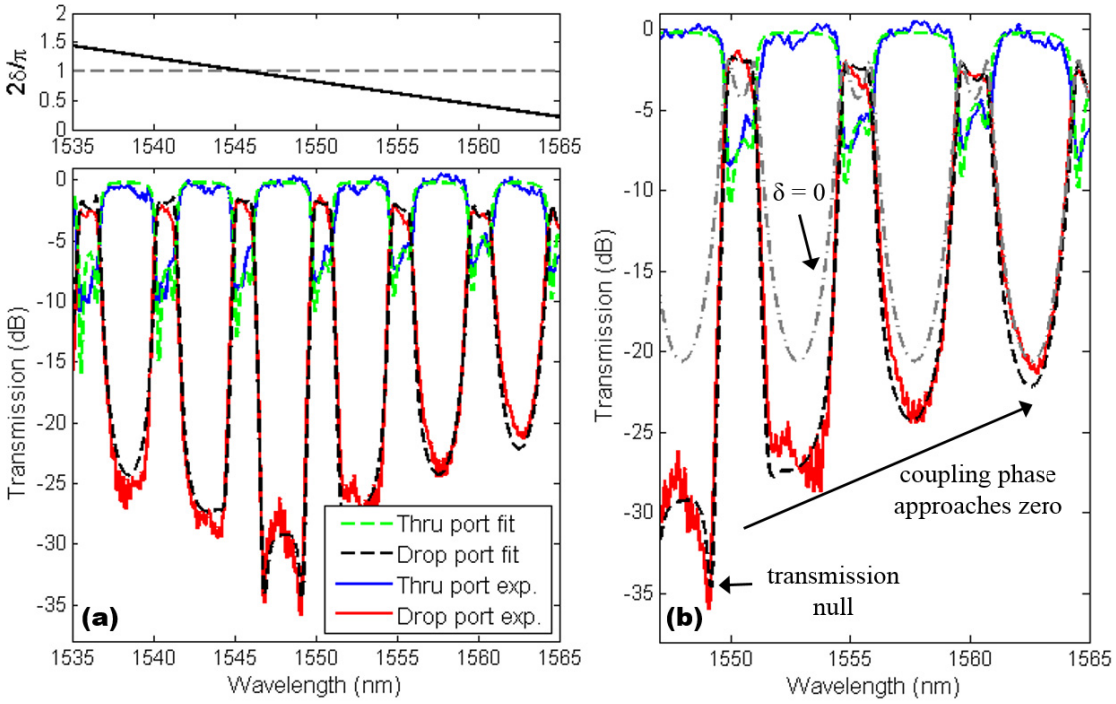

Figure 8.3: .(a) Top panel: coupling phase (2δ) of the quadrupole as a function of wavelength. Bottom panel: measured and fitted spectral responses of the quadrupole filter. Blue and red solid lines are the measured through and drop port responses; green and black dashed lines are the fitted responses. (b) Zoomed-in view of the transmission bands at 1551, 1556 and 1561 nm showing the effect of coupling phase dispersion on the spectral response. The grey dash-dotted line is the response when the coupling phase is zero i.e. κ_{14} is positive.

From the plots in Figures 8.3 (a) and (b), it is seen that near 1.55 μm, the drop port response of the quadrupole exhibits the steepest stop band transition with a deep extinction of more than -30dB. Away from the 1.55 μm wavelength the filter shape degrades gradually, exhibiting slower roll-off and shallower stop band extinction. We emphasize that such a rapid change in the spectral response over a short wavelength range is typically not observed in a CROW microring filter and is here attributed to the dispersion of the coupling phase in the quadrupole. As shown in the top panel of Figure 8.3 (a), around 1.55 μm the phase 2δ of the coupling element κ_{14} is close to π, leading to the formation of the transmission null which is responsible for the observed sharp band transition and deep extinction. Away from the 1.55 μm wavelength, the coupling phase approaches 0 or 2π causing the transmission zeros to

move away from the $j\omega$-axis in the complex frequency domain (or away from the unit circle in the z-plane) so that the transmission nulls become less sharp and eventually disappear. As a result, the filter roll-off becomes increasingly slower and the device response approaches that of a quadrupole resonator with positive coupling coefficients as shown by the grey dash-dotted line in Figure 8.3 (b).

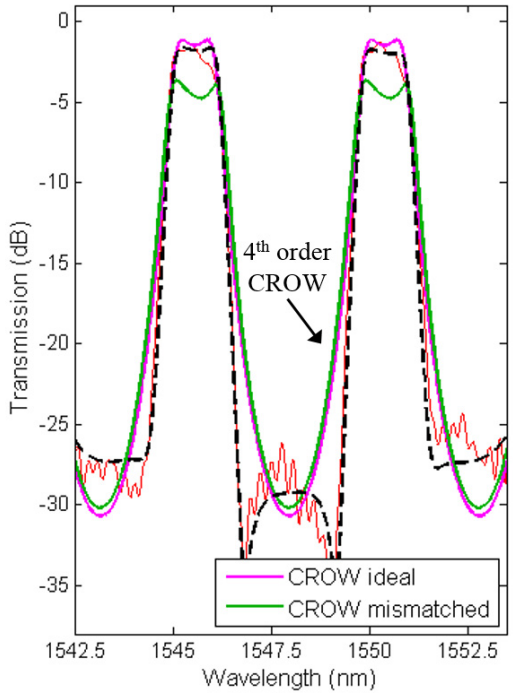

Figure 8.4: Comparison of the experimental pseudo-elliptic filter response (red line) to simulated responses of a 4th-order CROW filter for the ideal case, i.e. no resonance mismatch, (pink line) and when the device has the same resonance mismatches as the fabricated quadrupole (green line). The black-dashed line is the fitted response of the experimental quadrupole response.

In Figure 8.4 we compare the experimental performance of the 2D quadrupole resonator to the simulated response of a 4th-order CROW filter subject to the same conditions of loss and overcoupling as the fabricated quadrupole. The pink line shows the CROW response for the ideal case of no resonance mismatch while the green line is the response when the device has the same resonance mismatches as the fabricated quadrupole. The rolloff slopes for the quadrupole, ideal CROW, and mismatched CROW in that order at their respective 3 dB bandwidth points are 0.248 dB/GHz, 0.199 dB/GHz, and 0.191 dB/GHz while the slopes at the 10 dB bandwidth points

are 0.389 dB/GHz, 0.228 dB/GHz and 0.208 dB/GHz. It is seen that in both cases the CROW filter has a slower skirt roll-off than the pseudo-elliptic filter. In addition, we find that the CROW filter exhibits much more sensitivity to resonance mismatch than the 2D quadrupole device. Specifically, in the presence of the same resonance mismatches, the CROW filter suffers from severe degradation in the pass band, while the 2D quadrupole still retains its relatively flat-top transmission and sharp roll-offs. The robustness of the 2D coupling topology can be attributed to the fact that light can travel multiple pathways through the device so the transmission is less susceptible to individual resonance detunings.

8.4 Summary

In summary, the effects of coupling phase dispersion on the spectral response of a quadrupole micro-racetrack resonator were experimentally investigated for the first time. Clear evidence of negative coupling was observed through the sharp band transitions and deep extinction ratio in the resonator spectral response near the 1.55 μm wavelength. This work also provides the first demonstration of a pseudo-elliptic optical filter based on the 2D resonator coupling topology on the SOI platform. Both the proposed racetrack coupling topology and the experimental performance achieved help lay the groundwork for realizing a new class of microring devices based on 2D coupling topologies with complex coupling coefficients.

The work in this chapter was published in Optics Express in 2015 [96] and presented at CLEO in 2014 [104].

Chapter 9

Conclusion

It has been demonstrated many times that silicon photonic integrated circuits will require post-fabrication tuning due to minute deviations in waveguide width and/or height from designed dimensions due to fabrication errors [17, 18]. These deviations then induce phase errors in phase sensitive components like microring resonators and Mach Zehnder interferometers, which in most circumstances require correction in order for the device to operate properly. As discussed in detail in the introduction, there had been no permanent tuning mechanism demonstrated in silicon photonics that would be both fast and robust enough to implement for mass fabrication and also compatible with a CMOS manufacturing process. The goal of this thesis was to demonstrate a permanent tuning mechanism that would satisfy these requirements. The solution was to develop a tuning technique based on the irradiation of single femtosecond laser pulses to induce a permanent change in a silicon waveguide's index of refraction. To accomplish this goal, several experiments were designed and conducted to evaluate the feasibility and capability of single femtosecond laser pulses to tune silicon photonic integrated circuits. The key findings and contributions of the thesis are summarized below.

9.1 Key contributions in this thesis

- **Demonstration of the femtosecond laser tuning mechanism** - The first experiment performed in this thesis was to investigate the feasibility of using a femtosecond laser to induce permanent changes in a silicon waveguide's effective index of refraction. To accomplish this, a femtosecond laser tuning apparatus

was designed and constructed to irradiate an ultracompact silicon microring resonator with single femtosecond laser pulses. The experiment demonstrated that single femtosecond laser pulses could be used to change the effective index of refraction of a silicon waveguide. It was shown that the first shot on the ring caused an increase in the waveguide effective index of refraction at a fluence of 0.08 J/cm^2 and subsequent shots at increasing fluences also caused change in the waveguide. When a fluence of 0.20 J/cm^2 was exceeded, the change in the waveguide effective index was negative showing that the technique may be capable of bi-directional tuning. The experiment demonstrated that femtosecond laser modification can be used to tune silicon photonic integrated devices, but more experiments were still required to demonstrate the repeatibility and reliability of the technique.

- **Evaluation of the capability of femtosecond laser tuning** - While the first experiment demonstrated that femtosecond laser tuning mechanism may be useful in tuning silicon photonic integrated circuits, it left many questions still unanswered regarding the suitability of the method for tuning practical silicon photonic devices. Therefore more experiments were designed and conducted to test the reliability, repeatability and effectiveness of the femtosecond laser tunning mechanism. By irradiating several microring devices with single femtosecond laser pulses, we were able to show that in the amorphization regime the amount of resonance wavelength shift is dependent on the laser fluence with a linear relationship. Negative shifts were also achieved above the ablation threshold.

- **Femtosecond laser modification through a cladding layer** - For the technique to be truly useful as a post-fabrication method, it should also be able to modify silicon photonic integrated circuits with a cladding layer since most practical photonic circuits will have a cladding layer. Our femtosecond laser tuning experiments performed on microring resonators with a thick silicon dioxide cladding showed that positive increases in the waveguide effective index could be achieved and that there was the same linear relationship between the laser fluence and increase in waveguide effective index. However, as the bare sili-

con ablation threshold was approached, the waveguide effective index change saturated and eventually induced too much loss in the waveguide to still be trackable. The experiment showed that there exists a range of fluences for which the tuning curve is linear, which can be used to tune silicon photonic devices through a cladding layer.

- **Beamshaping to allow for fine tuning** - The previous experiments showed that the technique was capable of providing reliable coarse tuning using a top-hat beam shape. In order to demonstrate that the method is also capable of fine tuning, the beamshape was changed from a top-hat shape to a Gaussian shape and microrings were again used as the test device. The experiment showed that with a Gaussian beam shape,very fine tuning of the microring resonance could be achieved with shifts as small as the microring linewidth. The experimental curve was also compared to the expected result based on the previous experiments and was found to correlate very well which demonstrated again the repeatability and reliability of the femtosecond laser tuning mechanism. Overall, the experiment showed that for most practical applications of the tuning technique it would be better to use a Gaussian beam shape over the top-hat beam shape since it has a much better tuning resolution.

- **Effect of laser wavelength in tuning silicon photonic integrated devices and determination of the threshold fluences** - With the beam profile still set to a Gaussian shape, the tuning experiment was conducted again, but this time at a different wavelength. Previous experiments had been conducted at the second harmonic of the femtosecond laser, 400 nm, but in this experiment the wavelength was switched to the fundamental harmonic, 800nm. A similar tuning curve was obtained compared to the previous experiments and it was determined that this wavelength could also be used for fine tuning of silicon photonic integrated circuits. The threshold fluence for a permanent change to the silicon waveguides was also recorded and compared to previously obtained values in the literature. It was found to be about 5-6x lower than previously reported values and below the threshold for a visual change to the substrate. The result is significant because it demonstrates that the damage threshold for

silicon at 800 nm is lower than previousy thought.

- **Tuning more advanced silicon photonic integrated circuits** - The femtosecond laser tuning mechanism was also demonstrated to be capable of tuning advanced silicon photonic integrated circuits. A two ring Vernier filter was fabricated and found to initially have some resonance mismatch between the two rings. This was corrected with a single femtosecond laser pulseto yield a second-order filter response with a wide FSR. The technique was also demonstrated on a polarization diversity silicon photonic integrated circuit. The device was a DPSK demodulator which utlized two identical Mach Zehnder interferometers for polarization diversity. However, due to fabrication induced phase errors, the two interferometers did not have the same spectral responses. Using a single femotsecond laser pulse we could correct for the phase error and restore functionality to the polarization diversity DPSK demodulator. These application demonstrations showed that the femtosecond laser tuning method is robust and can be applied to advanced silicon photonic devices.

- **Demonstration of negative coupling and coupling phase dispersion in SOI platform** - A quadrupole micro-racetrack resonator filter in a 2D coupling topology was designed and fabricated in the silicon on insuator (SOI) platform. Using a sheared micro-racetrack coupling configuration, we were able to experimentally verify the effects of negative coupling and coupling phase dispersion in the quadrupole resonator. The device demonstrated a new architecture for creating 2D coupled microring filters with negative coupling.

9.2 Future research directions

Tuning with 266 nm

This thesis demonstrated that it is possible to tune silicon photonic integrated circuits using 400 nm and 800 nm wavelength femtosecond laser pulses. However, there is some evidence that indicates that it may be more beneficial to tune devices at a shorter wavelength. Izawa et al. studied the thicknesses of the amorphous silicon layer produced by single femtosecond laser pulses at varying wavelength and

found that the thicknesses of the layer were dependent on the wavelength [64, 65]. As the wavelength of the femtosecond laser was decreased so did the thickness of the amorphous silicon layer. At 800 nm, 400 nm, and 266 nm, the thicknesses of the amorphous silicon layers were 42 nm, 17 nm, and 7 nm respectively [64, 65]. This thinner layer of amorphous silicon at 266 nm may allow for finer tuning with less induced loss than femtosecond laser pulses at 400 nm or 800 nm.

Creating standalone devices with the femtosecond laser modification mechanism

It may also be possible to produce devices with a perturbed refractive index profile using the femtosecond laser tuning mechanism. By either patterning a silicon waveguide with a mask prior to femtosecond laser irradiation or by using a different beamshape, devices with periodic index perturbations such as gratings may be produced using the femtosecond laser.

Performing tuning with a nanosecond laser

Femtosecond lasers are very expensive when compared to other laser systems. The femtosecond laser tuning mechanism is based on the formation of a thin layer of amorphous silicon, but it may also be possible to produce a similar effect using a nanosecond laser. Recently, a single experiment has been published that used a nanosecond laser to provide coarse tuning of silicon photonic integrated circuits [105]. The authors reported issues with the repeatability and control of the method, but it may be something that warrants further study.

Reducing the loss caused by the technique

More experiments are required to discover the mechanism for the induced waveguide loss and how to reduce it.

Determination of the modification threshold at more laser wavelengths

The modification threshold was determined at two laser wavelengths, 400 nm and 800 nm, in this thesis. One of them agreed with previous experiments in the literature while one of them disagreed. By detemining the theshold fluence at many

more wavelengths, it may allow for better modelling of the fundamental processes involved in femtosecond laser matter interactions in silicon.

Determining the index of refraction and depth of laser amorphization region

More experiments are required to determine the depth and index of refraction in the laser modification region. This may be possible by fabricating many SOI photonic circuits with varying waveguide heights and then modelling the results in mode solver simulations. More research should also be conducted to determine the mechanism for the index of refraction change in the laser modification region.

Studying the effect of different pulse durations

All of the femtosecond laser pulses used in this thesis had a pulse duration of approximately 130 fs. It may be possible to change the final properties of the laser affected region by varying the pulse duration of the femtosecond laser and this would require further study.

Development of a table top system for commercial applications

The experiments conducted in this thesis were performed to demonstrate the potential of the femtosecond laser tuning mechanism in commercial applications. The experimental setup was based on free space optics which was difficult and time consuming to achieve good alignment. To show the full potential of the technique, a dedicated system could be designed and built with all the required functions occuring in the same system. Such a device could then be more automated to demonstrate the technique for post-fabrication tuning on a much larger scale.

Bibliography

[1] C. Gunn, "CMOS photonics for high-speed interconnects," *Micro, IEEE*, vol. 26, no. 2, pp. 58–66, 2006.

[2] J. Ahn, M. Fiorentino, R. G. Beausoleil, N. Binkert, a. Davis, D. Fattal, N. P. Jouppi, M. McLaren, C. M. Santori, R. S. Schreiber, S. M. Spillane, D. Vantrease, and Q. Xu, "Devices and architectures for photonic chip-scale integration," *Applied Physics A*, vol. 95, pp. 989–997, Feb. 2009.

[3] X. Zheng, P. Koka, H. Schwetman, J. Lexau, R. Ho, J. E. Cunningham, and K. A. V., "Silicon photonic WDM point-to-point network for multi-chip processor interconnects," in *Group IV Photonics, 2008 5th IEEE International Conference on*, pp. 380–382, 2008.

[4] A. Krishnamoorthy, H. Schwetman, P. Koka, I. Shubin, and J. Cunningham, "Computer Systems Based on Silicon Photonic Interconnects," *Proceedings of the IEEE*, vol. 97, pp. 1337–1361, July 2009.

[5] R. Ho, K. W. Mai, , and M. A. Horowitz, "The Future of Wires," vol. 89, no. 4, 2001.

[6] C. Batten, A. Joshi, J. Orcutt, and A. Khilo, "Building many-core processor-to-DRAM networks with monolithic CMOS silicon photonics," *Micro, IEEE*, vol. 29, no. 4, pp. 8–21, 2009.

[7] D. A. Miller, "Device requirements for optical interconnects to silicon chips," *Proceedings of the IEEE*, vol. 97, no. 7, pp. 1166–1185, 2009.

[8] "International technology roadmap for semiconductors: Interconnect," 2013 Edition.

[9] J. W. Goodman, F. J. Leonberger, S.-Y. Kung, and R. A. Athale, "Optical interconnections for vlsi systems," *Proceedings of the IEEE*, vol. 72, no. 7, pp. 850–866, 1984.

[10] M. Haurylau, G. Chen, H. Chen, J. Zhang, N. A. Nelson, D. H. Albonesi, E. G. Friedman, and P. M. Fauchet, "On-chip optical interconnect roadmap: challenges and critical directions," *Selected Topics in Quantum Electronics, IEEE Journal of*, vol. 12, no. 6, pp. 1699–1705, 2006.

[11] G. Chen, H. Chen, M. Haurylau, N. a. Nelson, D. H. Albonesi, P. M. Fauchet, and E. G. Friedman, "Predictions of CMOS compatible on-chip optical interconnect," *Integration, the VLSI Journal*, vol. 40, pp. 434–446, July 2007.

[12] K. C. Cadien, M. R. Reshotko, B. A. Block, A. M. Bowen, D. L. Kencke, and P. Davids, "Challenges for on-chip optical interconnects," in *Integrated Optoelectronic Devices 2005*, pp. 133–143, International Society for Optics and Photonics, 2005.

[13] B. Jalali and S. Fathpour, "Silicon Photonics," *Journal of Lightwave Technology*, vol. 24, pp. 4600–4615, Dec. 2006.

[14] R. Soref, "The past, present, and future of silicon photonics," *Selected Topics in Quantum Electronics, IEEE Journal of*, vol. 12, no. 6, pp. 1678–1687, 2006.

[15] W. Bogaerts, P. De Heyn, T. Van Vaerenbergh, K. De Vos, S. Kumar Selvaraja, T. Claes, P. Dumon, P. Bienstman, D. Van Thourhout, and R. Baets, "Silicon microring resonators," *Laser & Photonics Reviews*, vol. 6, pp. 47–73, Jan. 2012.

[16] D.-X. Xu, J. H. Schmid, G. T. Reed, G. Z. Mashanovich, D. J. Thomson, M. Nedeljkovic, X. Chen, D. Van Thourhout, S. Keyvaninia, and S. K. Selvaraja, "Silicon photonic integration platform-have we found the sweet spot?," *IEEE Journal of Selected Topics in Quantum Electronics*, vol. 20, no. 4, pp. 189–205, 2014.

[17] W. A. Zortman, D. C. Trotter, and M. R. Watts, "Silicon photonics manufacturing.," *Optics express*, vol. 18, pp. 23598–607, Nov. 2010.

[18] A. V. Krishnamoorthy, T. Pinguet, A. Mekis, H. Thacker, I. Shubin, K. Raj, and J. E. Cunningham, "Exploiting CMOS Manufacturing to Reduce Tuning Requirements for Resonant Optical Devices," *IEEE Photonics Journal*, vol. 3, pp. 567–579, June 2011.

[19] P. Dong, W. Qian, H. Liang, R. Shafiiha, N.-N. Feng, D. Feng, X. Zheng, A. V. Krishnamoorthy, and M. Asghari, "Low power and compact reconfigurable multiplexing devices based on silicon microring resonators.," *Optics express*, vol. 18, pp. 9852–8, May 2010.

[20] M. Dahlem and C. Holzwarth, "Reconfigurable multi-channel second-order silicon microring-resonator filterbanks for on-chip WDM systems," *Optics Express*, vol. 19, no. 1, pp. 306–316, 2011.

[21] X. Zheng, I. Shubin, G. Li, T. Pinguet, A. Mekis, J. Yao, H. Thacker, Y. Luo, J. Costa, K. Raj, J. E. Cunningham, and A. V. Krishnamoorthy, "A tunable 1x4 silicon CMOS photonic wavelength multiplexer/demultiplexer for dense optical interconnects.," *Optics express*, vol. 18, pp. 5151–60, Mar. 2010.

[22] A. P. Masilamani and V. Van, "Design and realization of a two-stage microring ladder filter in silicon-on-insulator.," *Optics express*, vol. 20, pp. 24708–13, Oct. 2012.

[23] Q. Xu, S. Manipatruni, B. Schmidt, J. Shakya, and M. Lipson, "12.5 Gbit/s carrier-injection-based silicon ring silicon modulators," *Optics Express*, vol. 15, no. 2, pp. 430–436, 2007.

[24] E. Timurdogan, C. M. Sorace-Agaskar, J. Sun, E. S. Hosseini, A. Biberman, and M. R. Watts, "An ultralow power athermal silicon modulator," *Nature communications*, vol. 5, 2014.

[25] L. Zhou, K. Okamoto, and S. J. B. Yoo, "Athermalizing and Trimming of Slotted Silicon Microring Resonators With UV-Sensitive PMMA Upper-Cladding," *IEEE Photonics Technology Letters*, vol. 21, no. 17, pp. 1175–1177, 2009.

[26] A. Canciamilla, F. Morichetti, S. Grillanda, P. Velha, M. Sorel, V. Singh, A. Agarwal, L. C. Kimerling, and A. Melloni, "Photo-induced trimming of chalcogenide-assisted silicon waveguides," *Optics Express*, vol. 20, no. 14, pp. 15807–15817, 2012.

[27] S. Prorok, A. Y. Petrov, M. Eich, J. Luo, and A. K.-Y. Jen, "Trimming of high-Q-factor silicon ring resonators by electron beam bleaching.," *Optics letters*, vol. 37, pp. 3114–6, Aug. 2012.

[28] A. H. Atabaki, A. A. Eftekhar, M. Askari, and A. Adibi, "Accurate post-fabrication trimming of ultra-compact resonators on silicon," *Optics express*, vol. 21, no. 12, pp. 14139–14145, 2013.

[29] J. Schrauwen, D. Van Thourhout, and R. Baets, "Trimming of silicon ring resonator by electron beam induced compaction and strain.," *Optics express*, vol. 16, pp. 3738–43, Mar. 2008.

[30] Y. Shen, I. B. Divliansky, D. N. Basov, and S. Mookherjea, "Electric-field-driven nano-oxidation trimming of silicon microrings and interferometers.," *Optics letters*, vol. 36, pp. 2668–70, July 2011.

[31] C. Chen, J. Zheng, T. Gu, and J. McMillan, "Selective tuning of high-Q silicon photonic crystal nanocavities via laser-assisted local oxidation," *Optics Express*, vol. 19, no. 13, pp. 3671–3673, 2011.

[32] S. Chu, W. Pan, S. Sato, T. Kaneko, B. Little, and Y. Kokubun, "Wavelength trimming of a microring resonator filter by means of a UV sensitive polymer overlay," *IEEE Photonics Technology Letters*, vol. 11, pp. 688–690, June 1999.

[33] S. Suzuki, Y. Hatakeyama, Y. Kokubun, and S. T. Chu, "Precise control of wavelength channel spacing of microring resonator add-drop filter array," *Journal of lightwave technology*, vol. 20, no. 4, p. 745, 2002.

[34] U. Levy, K. Campbell, A. Groisman, S. Mookherjea, and Y. Fainman, "On-chip microfluidic tuning of an optical microring resonator," *Applied Physics Letters*, vol. 88, no. 11, p. 111107, 2006.

[35] D. K. Sparacin, C.-y. Hong, L. C. Kimerling, J. Michel, J. P. Lock, and K. K. Gleason, "Trimming of microring resonators by photo-oxidation of a plasma-polymerized organosilane cladding material," *Optics Letters*, vol. 30, no. 17, pp. 2251–2253, 2005.

[36] D. Bachman, Z. Chen, A. M. Prabhu, R. Fedosejevs, Y. Y. Tsui, and V. Van, "Femtosecond laser tuning of silicon microring resonators," *Optics letters*, vol. 36, no. 23, pp. 4695–4697, 2011.

[37] D. Bachman, Z. Chen, R. Fedosejevs, Y. Y. Tsui, and V. Van, "Permanent fine tuning of silicon microring devices by femtosecond laser surface amorphization and ablation," *Optics express*, vol. 21, no. 9, pp. 11048–11056, 2013.

[38] D. Bachman, Z. Chen, Y. Y. Tsui, R. Fedosejevs, and V. Van, "Femtosecond laser tuning of si microring resonators by surface amorphization through a thick sio 2 cladding," in *CLEO: Science and Innovations*, pp. SF1J–8, Optical Society of America, 2014.

[39] K. De Vos, I. Bartolozzi, E. Schacht, P. Bienstman, and R. Baets, "Silicon-on-insulator microring resonator for sensitive and label-free biosensing," *Optics express*, vol. 15, no. 12, pp. 7610–7615, 2007.

[40] S. C. Buswell, V. a. Wright, J. M. Buriak, V. Van, and S. Evoy, "Specific detection of proteins using photonic crystal waveguides.," *Optics express*, vol. 16, pp. 15949–57, Sept. 2008.

[41] S. Yamatogi, Y. Amemiya, T. Ikeda, A. Kuroda, and S. Yokoyama, "Si Ring Optical Resonators for Integrated On-Chip Biosensing," *Japanese Journal of Applied Physics*, vol. 48, p. 04C188, Apr. 2009.

[42] M. Iqbal, M. A. Gleeson, B. Spaugh, F. Tybor, W. G. Gunn, M. Hochberg, T. Baehr-Jones, R. C. Bailey, and L. C. Gunn, "Label-free biosensor arrays based on silicon ring resonators and high-speed optical scanning instrumentation," *Selected Topics in Quantum Electronics, IEEE Journal of*, vol. 16, no. 3, pp. 654–661, 2010.

[43] K. Oda, N. Takato, and H. Toba, "A wide-fsr waveguide double-ring resonator for optical fdm transmission systems," *Lightwave Technology, Journal of*, vol. 9, no. 6, pp. 728–736, 1991.

[44] B. E. Little, S. T. Chu, H. A. Haus, J. Foresi, and J.-P. Laine, "Microring resonator channel dropping filters," *Lightwave Technology, Journal of*, vol. 15, no. 6, pp. 998–1005, 1997.

[45] B. Little, S. Chu, P. Absil, J. Hryniewicz, F. Johnson, F. Seiferth, D. Gill, V. Van, O. King, and M. Trakalo, "Very high-order microring resonator filters for wdm applications," *Photonics Technology Letters, IEEE*, vol. 16, no. 10, pp. 2263–2265, 2004.

[46] O. Schwelb, "Transmission, group delay, and dispersion in single-ring optical resonators and add/drop filters-a tutorial overview," *Journal of Lightwave Technology*, vol. 22, no. 5, p. 1380, 2004.

[47] Y. Vlasov, W. M. J. Green, and F. Xia, "High-throughput silicon nanophotonic wavelength-insensitive switch for on-chip optical networks," *Nature Photonics*, vol. 2, pp. 242–246, Mar. 2008.

[48] A. Yariv, "Universal relations for coupling of optical power between microresonators and dielectric waveguides," *Electronics Letters*, vol. 36, no. 4, pp. 321–322, 2000.

[49] J. C. Miller, "A brief history of laser ablation," in *AIP Conference Proceedings*, pp. 619–622, AIP, 1994.

[50] X. Liu, D. Du, and G. Mourou, "Laser ablation and micromachining with ultrashort laser pulses," *Quantum Electronics, IEEE Journal of*, vol. 33, no. 10, pp. 1706–1716, 1997.

[51] B. Rethfeld, K. Sokolowski-Tinten, D. Von Der Linde, and S. Anisimov, "Timescales in the response of materials to femtosecond laser excitation," *Applied Physics A*, vol. 79, no. 4-6, pp. 767–769, 2004.

[52] M. Downer, R. L. Fork, and C. V. Shank, "Femtosecond imaging of melting and evaporation at a photoexcited silicon surface," *JOSA B*, vol. 2, no. 4, pp. 595–599, 1985.

[53] K. Sokolowski-Tinten, J. Bialkowski, and D. Von der Linde, "Ultrafast laser-induced order-disorder transitions in semiconductors," *Physical Review B*, vol. 51, no. 20, p. 14186, 1995.

[54] P. Stampfli and K. Bennemann, "Time dependence of the laser-induced femtosecond lattice instability of si and gaas: Role of longitudinal optical distortions," *Physical Review B*, vol. 49, no. 11, p. 7299, 1994.

[55] D. Korfiatis, K. T. Thoma, and J. Vardaxoglou, "Conditions for femtosecond laser melting of silicon," *Journal of Physics D: Applied Physics*, vol. 40, no. 21, p. 6803, 2007.

[56] C. Shank, R. Yen, and C. Hirlimann, "Time-resolved reflectivity measurements of femtosecond-optical-pulse-induced phase transitions in silicon," *Physical Review Letters*, vol. 50, no. 6, p. 454, 1983.

[57] S. Sundaram and E. Mazur, "Inducing and probing non-thermal transitions in semiconductors using femtosecond laser pulses," *Nature materials*, vol. 1, no. 4, pp. 217–224, 2002.

[58] K. Sokolowski-Tinten, J. Bialkowski, A. Cavalleri, D. Von der Linde, A. Oparin, J. Meyer-ter Vehn, and S. Anisimov, "Transient states of matter during short pulse laser ablation," *Physical Review Letters*, vol. 81, no. 1, pp. 224–227, 1998.

[59] D. Von der Linde and K. Sokolowski-Tinten, "The physical mechanisms of short-pulse laser ablation," *Applied Surface Science*, vol. 154, pp. 1–10, 2000.

[60] J. Bonse, S. Baudach, J. Krüger, W. Kautek, and M. Lenzner, "Femtosecond laser ablation of silicon–modification thresholds and morphology," *Applied Physics A*, vol. 74, no. 1, pp. 19–25, 2002.

[61] J. Bonse, "All-optical characterization of single femtosecond laser-pulse-induced amorphization in silicon," *Applied Physics A*, vol. 84, pp. 63–66, Apr. 2006.

[62] J. Bonse, K.-W. Brzezinka, and A. Meixner, "Modifying single-crystalline silicon by femtosecond laser pulses: an analysis by micro raman spectroscopy, scanning laser microscopy and atomic force microscopy," *Applied surface science*, vol. 221, no. 1, pp. 215–230, 2004.

[63] A. Kiani, K. Venkatakrishnan, and B. Tan, "Micro/nano scale amorphization of silicon by femtosecond laser irradiation," *Optics express*, vol. 17, no. 19, pp. 16518–16526, 2009.

[64] Y. Izawa, S. Tokita, M. Fujita, M. Nakai, T. Norimatsu, and Y. Izawa, "Ultrathin amorphization of single-crystal silicon by ultraviolet femtosecond laser pulse irradiation," *Journal of Applied Physics*, vol. 105, no. 6, p. 064909, 2009.

[65] Y. Izawa, Y. Izawa, Y. Setsuhara, M. Hashida, M. Fujita, R. Sasaki, H. Nagai, and M. Yoshida, "Ultrathin amorphous Si layer formation by femtosecond laser pulse irradiation," *Applied Physics Letters*, vol. 90, no. 4, p. 044107, 2007.

[66] Y. Izawa, Y. Setuhara, M. Hashida, M. Fujita, and Y. Izawa, "Ablation and Amorphization of Crystalline Si by Femtosecond and Picosecond Laser Irradiation," *Japanese Journal of Applied Physics*, vol. 45, pp. 5791–5794, July 2006.

[67] T. Höche, D. Ruthe, and T. Petsch, "Low-fluence femtosecond-laser interaction with a mo/si multilayer stack," *Applied Physics A*, vol. 79, no. 4-6, pp. 961–963, 2004.

[68] A. Borowiec, M. Mackenzie, G. Weatherly, and H. Haugen, "Transmission and scanning electron microscopy studies of single femtosecond-laser-pulse ablation of silicon," *Applied Physics A*, vol. 76, no. 2, pp. 201–207, 2003.

[69] M. S. Rogers, C. P. Grigoropoulos, A. M. Minor, and S. S. Mao, "Absence of amorphous phase in high power femtosecond laser-ablated silicon," *Applied Physics Letters*, vol. 94, no. 1, p. 011111, 2009.

[70] J. Jia, M. Li, and C. V. Thompson, "Amorphization of silicon by femtosecond laser pulses," *Applied physics letters*, vol. 84, no. 16, pp. 3205–3207, 2004.

[71] E. Coyne, J. Magee, P. Mannion, G. Oconnor, and T. Glynn, "Stem (scanning transmission electron microscopy) analysis of femtosecond laser pulse induced damage to bulk silicon," *Applied Physics A*, vol. 81, no. 2, pp. 371–378, 2005.

[72] T. Crawford, J. Yamanaka, G. Botton, and H. Haugen, "High-resolution observations of an amorphous layer and subsurface damage formed by femtosecond laser irradiation of silicon," *Journal of Applied Physics*, vol. 103, no. 5, p. 053104, 2008.

[73] M. Amer, M. El-Ashry, and L. Dosser, "Femtosecond versus nanosecond laser machining: comparison of induced stresses and structural changes in silicon wafers," *Applied Surface Science*, vol. 242, pp. 162–167, Mar. 2005.

[74] M. A. Green and M. J. Keevers, "Optical properties of intrinsic silicon at 300 k," *Progress in Photovoltaics: Research and Applications*, vol. 3, no. 3, pp. 189–192, 1995.

[75] E. D. Palik, *Handbook of optical constants of solids*, vol. 3. Academic press, 1998.

[76] E. Hecht, *Optics 4th edition*. San Francisco, USA: Addison Wesley Longman Inc, 1998.

[77] D. Bachman, Z. Chen, A. M. Prabhu, R. Fedosejevs, Y. Tsui, and V. Van, "Post-fabrication tuning of silicon microring resonators by femtosecond laser modification," in *Integrated Photonics Research, Silicon and Nanophotonics*, p. IME2, Optical Society of America, 2011.

[78] W.-J. Liu, S. Chen, H.-Y. Cheng, J.-D. Lin, and S.-L. Fu, "Fabrication of amorphous silicon films for arrayed waveguide grating application," *Surface and Coatings Technology*, vol. 201, pp. 6581–6584, Apr. 2007.

[79] M. J. a. de Dood, a. Polman, T. Zijlstra, and E. W. J. M. van der Drift, "Amorphous silicon waveguides for microphotonics," *Journal of Applied Physics*, vol. 92, no. 2, p. 649, 2002.

[80] B. E. Little, J. P. Laine, and S. T. Chu, "Surface-roughness-induced contradirectional coupling in ring and disk resonators.," *Optics letters*, vol. 22, pp. 4–6, Jan. 1997.

[81] F. Morichetti, A. Canciamilla, and A. Melloni, "Statistics of backscattering in optical waveguides.," *Optics letters*, vol. 35, pp. 1777–9, June 2010.

[82] F. Morichetti, A. Canciamilla, M. Martinelli, A. Samarelli, R. M. De La Rue, M. Sorel, and A. Melloni, "Coherent backscattering in optical microring resonators," *Applied Physics Letters*, vol. 96, no. 8, p. 081112, 2010.

[83] G. C. Ballesteros, J. Matres, J. Martí, and C. J. Oton, "Characterizing and modeling backscattering in silicon microring resonators.," *Optics express*, vol. 19, pp. 24980–5, Dec. 2011.

[84] M. Huang, "Stress effects on the performance of optical waveguides," *International Journal of Solids and Structures*, vol. 40, no. 7, pp. 1615–1632, 2003.

[85] D. Bachman, Z. Chen, R. Fedosejevs, Y. Tsui, and V. Van, "Permanent tuning of high-q silicon microring resonators by fs laser surface modification," in *Conference on Lasers and Electro-Optics/Pacific Rim*, p. TuPM_8, Optical Society of America, 2013.

[86] D. Bachman, Z. Chen, J. N. Westwood-Bachman, W. K. Hiebert, Y. Painchaud, M. Poulin, R. Fedosejevs, Y. Y. Tsui, and V. Van, "Permanent phase correction in a polarization diversity si pic by femtosecond laser pulses," *Photonics Technology Letters, IEEE*, vol. 27, no. 17, pp. 1880–1883, 2015.

[87] N. Medvedev and B. Rethfeld, "A comprehensive model for the ultrashort visible light irradiation of semiconductors," *Journal of Applied Physics*, vol. 108, no. 10, p. 103112, 2010.

[88] R. Boeck, N. A. Jaeger, N. Rouger, and L. Chrostowski, "Series-coupled silicon racetrack resonators and the vernier effect: theory and measurement," *Optics express*, vol. 18, no. 24, pp. 25151–25157, 2010.

[89] H. Fukuda, K. Yamada, T. Tsuchizawa, T. Watanabe, H. Shinojima, and S.-i. Itabashi, "Silicon photonic circuit with polarization diversity," *Optics express*, vol. 16, no. 7, pp. 4872–4880, 2008.

[90] L. Chen, C. R. Doerr, and Y.-K. Chen, "Compact polarization rotator on silicon for polarization-diversified circuits," *Optics letters*, vol. 36, no. 4, pp. 469–471, 2011.

[91] D. Dai and J. E. Bowers, "Novel concept for ultracompact polarization splitter-rotator based on silicon nanowires," *Optics express*, vol. 19, no. 11, pp. 10940–10949, 2011.

[92] Y. Painchaud, M. Poulin, J.-F. Gagné, and C. Paquet, "Ultra-compact si-photonic dqpsk demodulator," in *Optical Fiber Communication Conference*, pp. OM3J–3, Optical Society of America, 2012.

[93] D. Taillaert, H. Chong, P. I. Borel, L. H. Frandsen, R. M. De La Rue, and R. Baets, "A compact two-dimensional grating coupler used as a polarization splitter," *Photonics Technology Letters, IEEE*, vol. 15, no. 9, pp. 1249–1251, 2003.

[94] D. Bachman, Z. Chen, J. N. Westwood, W. K. Hiebert, Y. Painchaud, M. Poulin, R. Fedosejevs, Y. Y. Tsui, and V. Van, "Permanent, post-fabrication trimming of polarization diversity silicon circuits by single fs laser pulses," in *Frontiers in Optics*, pp. FM3A–5, Optical Society of America, 2014.

[95] M. A. Popovic, "Experimental demonstration of loop-coupled microring resonators for optimally sharp optical filters," in *Conference on Lasers and Electro-Optics*, p. CTuNN, Optical Society of America, 2008.

[96] D. Bachman, A. Tsay, and V. Van, "Negative coupling and coupling phase dispersion in a silicon quadrupole micro-racetrack resonator," *Optics express*, vol. 23, no. 15, pp. 20089–20095, 2015.

[97] A. Yariv, "Coupled-mode theory for guided-wave optics," *Quantum Electronics, IEEE Journal of*, vol. 9, no. 9, pp. 919–933, 1973.

[98] F. Xia, M. Rooks, L. Sekaric, and Y. Vlasov, "Ultra-compact high order ring resonator filters using submicron silicon photonic wires for on-chip optical interconnects," *Optics express*, vol. 15, no. 19, pp. 11934–11941, 2007.

[99] V. Van, "Synthesis of elliptic optical filters using mutually coupled microring resonators," *Journal of Lightwave Technology*, vol. 25, no. 2, pp. 584–590, 2007.

[100] M. A. Popovic, "Sharply-defined optical filters and dispersionless delay lines based on loop-coupled resonators and negative coupling," in *Conference on Lasers and Electro-Optics*, p. CThP6, Optical Society of America, 2007.

[101] A. Tsay and V. Van, "A method for exact synthesis of 2xn coupled microring resonator networks," *IEEE Photonics Technology Letters*, vol. 23, no. 23, pp. 1778–1780, 2011.

[102] A. Tsay and V. Van, "Analysis of coupled microring resonators in sheared lattices," *Photonics Technology Letters, IEEE*, vol. 24, no. 18, pp. 1625–1627, 2012.

[103] R. Halir, I. Molina-Fernández, J. Wangüemert-Pérez, A. Ortega-Moñux, J. de Oliva-Rubio, and P. Cheben, "Characterization of integrated photonic devices with minimum phase technique," *Optics express*, vol. 17, no. 10, pp. 8349–8361, 2009.

[104] D. Bachman, A. Tsay, and V. Van, "Realization of a 4th-order pseudo-elliptic microring filter with negative coupling on soi," in *CLEO: Science and Innovations*, pp. SM3G–7, Optical Society of America, 2014.

[105] M. Jizodo, S. Kamei, K. Kikuchi, and T. Saida, "Si photonics wavelength-adjustable crosstalk suppression filter by using coarse laser trimming," in *Group IV Photonics (GFP), 2015 IEEE 12th International Conference on*, pp. 207–208, IEEE, 2015.